UNIVERSITÀ DI PARMA

UNIVERSITA' DEGLI STUDI DI PARMA

DOTTORATO DI RICERCA IN SCIENZA E TECNOLOGIA DEI MATERIALI

CICLO XXXIV

GRAPHENE-SUPPORTED NOVEL CHEMISTRIES IN LITHIUM-ION BATTERIES

Coordinatore:

Chiar.mo Prof. Dalcanale Enrico

Tutore:

Chiar.mo Prof. Riccò Mauro

Co-tutore:

Chiar.mo Prof. Pontiroli Daniele

Dottorando: Sidoli Michele

Anni Accademici 2018/2019 – 2020/2021

Pour ce qui est de l'avenir,

il ne s'agit pas de le prévoir,

mais de le rendre possible.

Antoine de Saint-Exupéry, 1948

As for the future,

it is not a question of foreseeing it,

but of making it possible.

ABSTRACT

Among energy storage devices, lithium-ion batteries represent the state-of-the-art technology, being widely employed in portable electronics, stationary storage and even electric mobility. Despite being our best solution, there are numerous problems bound to their employment, such as the still not clear recycling path of exhausted batteries, the scarcity or toxicity of key materials (e.g., nickel, cobalt, manganese etc) that are not sufficient to support an electric fueled mobility and the intrinsic limits of the performance of the commercially available lithium-ion batteries. In fact, commercial cathodes are characterized by relatively low capacities and an unfavorable energy density, because of the presence of heavy metals. Also commercial anodes have limited capacities, if compared with newly proposed materials. Apparently, extensive research can only cut down little of both prices and slightly increase the performance in the foreseeable future, due to the already optimized technology, while only large-scale production can moderately inhibit the costs.

A viable solution is offered by innovative chemistries of lithium-ion batteries, which employ novel active materials characterized by elevated energy densities and low impact. These technologies are not already widely commercialized because they are still affected by limitations, that so far make these solutions suitable only for niche applications. The current interest is in making these devices robust and versatile, and the ideal path is to create composites with materials that will overcome the limitations of the bare active material. In this work, macroscopic amount of chemically produced graphene was employed as a scaffold for such new chemistries with a twofold role: on the one hand, graphene is able to support the electroactive materials at the nanoscale; on the other hand, it provides a conductive network that promotes the charges extraction from the electrode. In addition, chemically derived graphene is a porous material with a high specific surface area, and can successfully buffer the volumetric swelling of the electroactive materials which happen upon lithium uptake and retain the eventual cracking of the particles due to continuous swelling and shrinkage. For these reasons, graphene is an ideal candidate for these roles, due to its electrical, mechanical and specific surface area characteristics. In this thesis, graphene was combined with three different innovative electroactive materials, namely titanium dioxide, sulfur and silicon.

For the case of titanium dioxide, a chemically derived graphene, obtained by the thermal exfoliation of graphite oxide, was used to enhance the performance of the still under study TiO_2-based lithium-ion batteries. The composite materials were successfully produced, either via decoration of the

graphene during the solvothermal synthesis of TiO_2 nanoparticles, or via physical mixing by means of high energy ball milling. The electrochemical performance of the electrodes have been markedly improved by the addition of just a 1% in weight of graphene. In addition, the structural evolution of the electrode upon lithiation and de-lithiation was investigated via operando synchrotron light diffraction, which highlighted the different steps of the Li intercalation process in these materials. These results encouraged the employment of TiO_2-graphene composites as anodes in lithium-ion batteries.

Subsequently, graphene has been combined with sulfur to produce S-graphene composites, following four different routes: I) physical mixing of the reagents via ball milling, II) liquid-assisted ball milling (or wet ball milling), III) thermal infiltration of sulfur in the graphene matrix and IV) chemical decoration of graphene with sulfur. Specifically, the last synthesis was performed by precipitation of sulfur in a solution containing graphene oxide, which was subsequently chemically reduced. A systematic study of the synthetic route along with the research of the best sulfur-to-carbon ratio was carried out, and the chemically produced sample with 70 % sulfur loading was proven as the best candidate for lithium-sulfur batteries, obtaining a mean reversible capacity of about 500 mAh/g after 100 cycles.

Finally, graphene was employed as a conductive agent for silicon-based batteries. In particular, silicon nanoparticles produced by the disproportionation of silicon monoxide achieved remarkable results. The Si nanoparticles obtained by this synthesis measured about 4 nm in size. The challenging etching of the silicon oxides was performed in an ad hoc plastic apparatus, employing ammonium hydrogen difluoride as an etching agent. Unfortunately, the etching step was not successful, but the silicon mixture was electrochemically characterized nonetheless. The electrodes fabricated with disproportionated silicon monoxide were measured having an impressive starting capacity exceeding 7000 mAh/g, with a reversible capacity of 1150 mAh/g retained after more than 70 cycles.

Summary

List of figures

List of abbreviations

CB	Carbon black
CP	Chronopotentiometry
DMC	Dimethyl carbonate
DME	1,3-dimethoxyethane
DOL	1,3-dioxolane
EC	Ethylene carbonate
Eg	Energy gap
EtOH	Ethanol
GCD	galvanostatic charge/discharge
GO	Graphene oxide
HOMO	Highest occupied molecular orbital
HT	Hydrothermal
LAA	L-ascorbic acid
LAA-rGO	L-ascorbic acid reduced graphene oxide
LIB	Lithium-ion battery
Li/S	Lithium sulfur
LiTFSI	Lithium bis (trifluoromethane) sulphonamide
LMO	Lithium metal oxide
LTO	Lithium titanate
LUMO	Lowest unoccupied molecular orbital
NMP	N-methyl-2-pyrrolidone
NP	Nanoparticles
OCV	Open circuit voltage
PAA	Polycrylic acid
PVDF	Poly (vinylidene difluoride)
PXRD	Powder X-ray diffraction
rGO	Reduced graphene oxide
RT	Room temperature
SEI	Solid electrolyte interphase
SEM	Scanning electron microscopy
SHE	Standard hydrogen electrode
SXRPD	Synchrotron X-ray powder diffraction
TEGO	Thermally exfoliate graphene oxide
TEM	Transmission electron microscopy
THF	Tetrahydrofuran
TTIP	Titanium tetraisopropoxide
XRD	X-ray diffraction

Battery glossary

Active Material	The element or compound that releases or stores electrical energy during electrochemical operations.
Ampere	Ampere is the unit of measure of electrical current. Current is defined as the amount of charge flowing per unit of time.
Ampere-hour	Unit of charge, namely the current of 1 ampere flowing over an hour (Ah).
Anode	Electrode with the lower potential in an electrolytic cell.
Capacity	Quantity of energy a battery can release in a single discharge, measured in Ah.
Capacity fade	Gradual decrease of the quantity of charge a battery can deliver, caused by irreversible chemical and structural changes of the components.
Cathode	Electrode with the higher potential in an electrolytic cell.
Charge Rate	Or C-rate. It quantifies the current delivered from or supplied to the cell as a fraction of the theoretical battery capacity.
Current collector	Copper (for anodes) and aluminum (for cathodes) onto which electrodes are cast.
Cycle Stability	Number of cycles a battery can undergo before its capacity drops below a certain percentage of its original capacity.
Efficiency	Ratio between the current supplied to the battery and subsequently extracted within a consecutive charge and discharge semicycle.
Electrolyte	Medium that allows the ion exchange between separated electrodes.
Galvanostatic charge/discharge	GCD. In this technique, the battery is charged and discharged between a voltage window at a constant current.
Nominal Cell Voltage	The average voltage at which a cell operates during charge/discharge operations.
Open-Circuit Voltage	OCV. The voltage of a battery when it is not in use.
Power density	Volumetric or gravimetric power of a battery. It is expressed in W/L or W/Kg
Secondary Battery	Cell operating via reversible reactions. Also called rechargeable battery.
Separator	Plastic film used to separate the electrodes spatially and electrically, preventing the short circuit of the system.
Specific capacity	Is the measure of the charge stored for weight unit by a battery, usually expressed in mAh/g.
Specific energy density	Is the amount of energy in a given mass (gravimetric energy density) or volume (volumetric energy density). It is expressed in Wh/Kg or Wh/L.

1 INTRODUCTION

1.1 BACKGROUND

Today's society is facing an ever-growing energy demand. This is related with a steady growth of the world's gross domestic product (GDP), which was experiencing an ascending trend until the 2020 pandemic. This sudden production hiatus has caused a decrease of 4% of both the World's overall GDP and the energy demand. These contractions have been rebounded by 2021 economic stimulus, which has led to a 6% GDP growth paired with a + 4.6% energy demand [1]. The production of electricity is mainly generated by burning fossil fuels, which have the advantage of being efficient, convenient, and well established, but their exploitation poses a serious threat to our development on the planet as we have known it so far. The use of fossil fuels has seen a stasis in recent years, mostly caused by the environment politics employed by first world countries, recently encouraged by the subscription of the Paris Climate Agreement by U.S. under Biden's administration. Unfortunately, China and developing countries like India are still far from western goals about carbon neutrality and CO_2 emissions, even though some "green" politics are starting to emerge. These conditions favor the harnessing of renewable sources. In fact, despite the rise in the consumption of fossil fuels, their share in the energy market has decreased. In Figure 1-1 [2] the generations shares are highlighted. Today, the 25% of the global power output is generated by renewable sources, but the hunger for energy is inevitably reflected in a CO_2 emission growth. To face this unruled trend, the International Panel on Climate Change (IPCC) is releasing annual reports, assessing environmental science issues. Of these reports, the most ground-shaking document is "Global Warming of 1.5°C" [3], in which it is shown

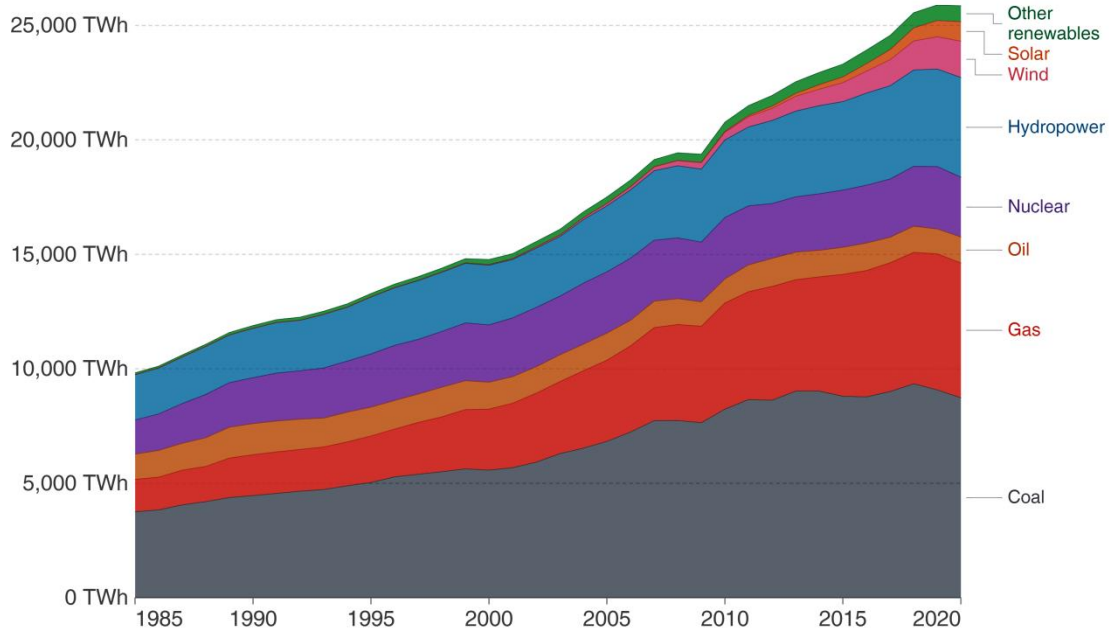

Figure 1-1 Sources share in energy production. The graph depicts the global energy production by the main different sources, in absolute values.

how the mean temperatures have risen of about ~1°C since pre-industrial levels, and are forecast to reach 1.5°C in a span ranging from 2030 to 2052. In the aforementioned document, the 1.5°C mean temperature increase is considered as a point of no return, because after that, adaptation would be harder, and the intensity and frequency of extreme events would be harsher and the impact on resources, food, ecosystems, biodiversity, carbon and more severe. In recent days we have already seen important meteorological events, such as heavy precipitations, floods and droughts, and this drift is bound to become chronic. The most viable route to slow down this trend is to switch the energy production, shifting from a carbon-based energy market to renewable sources whenever possible. Still, the major issue with renewable sources is their intrinsic variability and intermittent nature [4]. Even though renewable sources may satisfy and exceed the energy demand peak, they are limited by their non dispatchable nature, as shown in Figure 1-2. For instance, solar has a day/night cycle, while wind has no possible forecast. The only

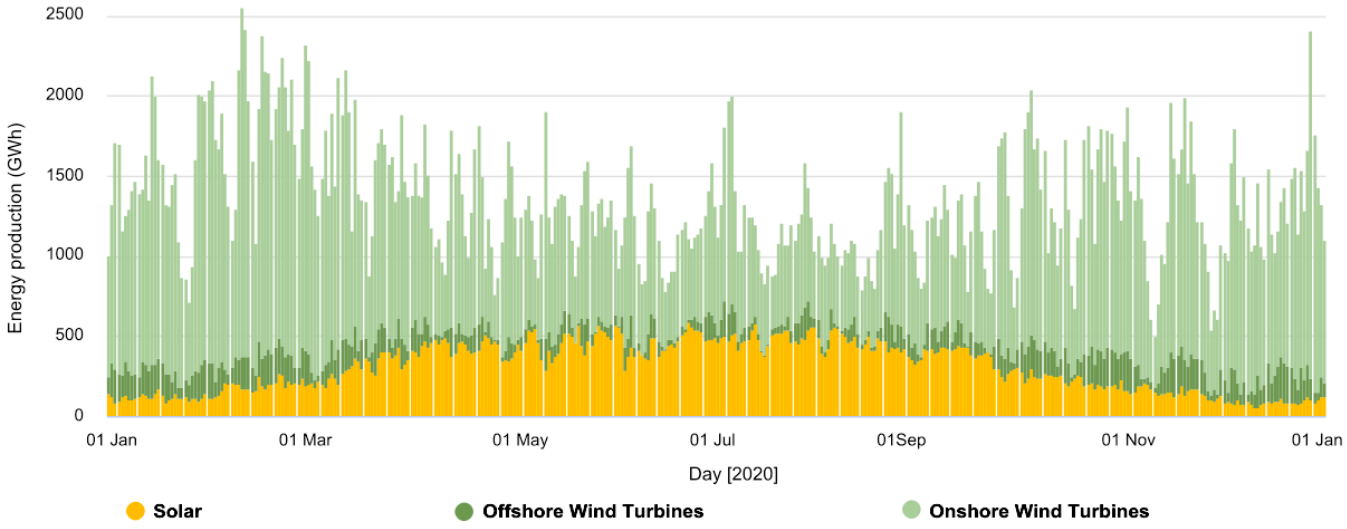

Figure 1-2 Daily energetic production in European Union by renewable sources (solar and eolic).

dispatchable renewable sources are geothermal, hydroelectric and biomass. To succeed in the aim of this "*green revolution*", the passage to renewable sources must be buffered with the support of storage systems. Traditionally, most of the energy surplus is stored by pumping water back up to dam lake reservoirs in order to refuel hydroelectric plants. When this solution is not available (e.g., small plants, domestic storage, et cetera), many other systems can compensate for it, e.g. electrical, mechanical, chemical and electrochemical storage systems, each of them offering its peculiar pros and cons [5–7]. Electrochemical storage in batteries is under most circumstances, the most viable and versatile solution, and, among these, Li-ion batteries (LIBs) are the best developed and still the most promising ones, with few doubts on their role in modern economies. Their strength comprehends being lightweight, modular, pollution-free while operating (the disposal takes place at end-life) and having high efficiency and long cycle life (over 1000 cycles). All these characteristics grant their employment both in stationary and mobile solutions, making them viable in uses ranging from household buffers, electric mobility to portable electronics. Batteries can be easily built in a range of shapes and dimensions and are low in maintenance. LIBs are also considered being cheap, and their price has

dropped by 88% in the last decade, and it is forecast to deflect further on, but some limitations emerge. LIBs current price is below 100$/kWh [8], but the trend is coming to a stop due to the intrinsic costs of the raw materials, which are predicted to increase in the next decade, due to their intensive exploitation [9]. In order to give a stimulus to the price per kWh deflection, it is necessary to explore and study new battery chemistries, since investigation of the current systems has limited room for improvement before stumbling on unavoidable practical limits. A shift is needed because an enormous boost in the battery market will be imposed by the development of electric mobility. Based on the actual trend, electric vehicles (EVs) should surpass internal combustion engines sales by 2035 and our roads will be trafficked by more EVs than internal combustion engine vehicles by 2040 [10]. The advantages of electric mobility consist in lowering the pollution in highly populated areas, allowing the concentration of power production in specialized plants and farms. This will allow the carbon footprint reduction of road transportation, which constitutes the 73% of transport-related CO_2 emissions [11]. Thus, the development of new solutions in electrochemical storage can help the reduction of greenhouse gas emissions and decrease in the carbon footprint of human activities, but this will be only viable if the economic aspects will be convenient as well. Creating and implementing greener chemistries in commercial batteries may pave the way for low impact energy solutions without penalizing economy and production efficiency, while creating new jobs and opportunities.

The aim of this thesis is the exploration of novel and challenging battery chemistries, and the *fil rouge* of the research is the harnessing of carbon nanostructures as scaffolds and supports for these still to be explored chemistries, respectively titanium dioxide batteries, silicon batteries and sulfur LIBs. All of these chemistries present their own advantages and drawbacks that will be introduced in each chapter, but carbon can be used in each system to resolve or mitigate problems that prevent the employment of the technology. In order to explore the functioning and the issues of each of these systems, the next chapter will explain the general components and operations of a LIBs, and a more detailed explanation will be provided for each specific chemistry.

1.2 LIBs. Components and operations

1.2.1 Working principle of a LIB

The history of LIBs is short but has been running a fast race. The idea behind the technology lays on the pioneering work developed by Goodenough, Whittingham and Yoshino in the 1970s. These scientists, who were awarded the 2019 Nobel prize for chemistry [12], studied the concepts and the materials on which today's technology is based. After their first commercialization in 1991 LIBs keep driving a lot of interest since electrochemical storage was identified - along with renewable sourced energy – as a key strategy for a clean transition from the fossil fuels exploitation [13]. Electrochemical storage systems are so far from the most interesting storage technologies and operate by converting electrical energy in chemical energy and viceversa. Two common indexes to quantify the performance of storage technologies are energy density, usually expressed in Wh/kg and power density, expressed in W/kg. The first quantifies the amount of energy a device can store per unit of mass, while the second describes how quickly a device can discharge its energy per unit of mass. In a Ragone plot (Figure 1-3) these indexes are plotted, and different electrochemical storage technologies are positioned following their energy and power density characteristic. The oblique lines that cross the diagram are timelines that indicate the time needed to fully charge or discharge the device, hence related to the power density. It can be noticed that (super)capacitors respond to high power necessities, while batteries are ideal for high energy density applications. In particular, LIBs have amongst the better energy densities, if we exclude more complex systems such as metal-air and fuel cells, with typical energy densities ranging between 70 to 265 Wh/kg (or 250 to 670 Wh/L). This is made possible by the brilliant yet simple design of a commercial LIB, which has not changed much in the last decades, despite the huge effort dedicated in investigating the electrochemical behavior of lithium and materials capable of storing and hosting lithium ions [14]. In Figure 1-4 the structure and

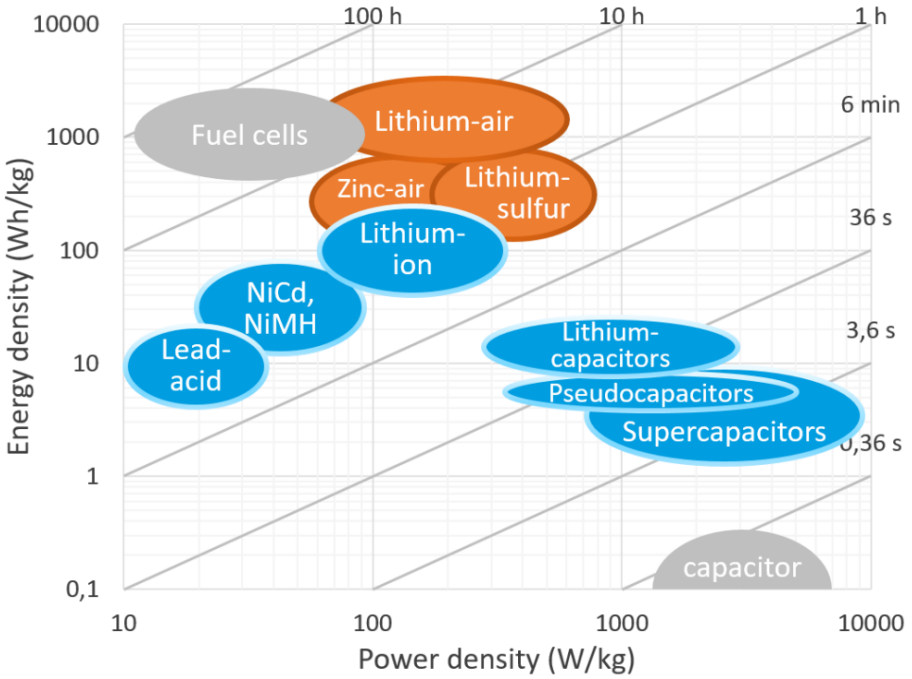

Figure 1-3 Ragone plot of the most popular electrochemical storage technologies

the mechanism of a commercial LIB is depicted. A classical LIB is composed by two electrodes, namely anode and cathode, separated by a separator and wet by an electrolyte. In detail, most cathode materials consist of layered or spinel-like lithium metal oxides ($Li_{1-x}MOs$), which can host and allow the intercalation/deintercalation of lithium ions. The typical specific capacities of cathodes range from 150 to 270 mAh/g, which is the amount of current a material can store and deliver normalized on its weight. On the anode side, graphite plays a leading role since the first commercialization of LIBs, even though many alternatives are emerging in recent years, which are preferable both in terms in sustainability and performance. Graphite consists of a layered sp^2 carbon which can host the ions between its planar structure, with a specific capacity of 372 mAh/g. This insertion takes place at a low voltage vs Li/Li^+, allowing good performance even in the absence of metallic lithium, which was considered the ideal anode since its specific capacity of 3860 mAh/g and lowest electrochemical potential (- 3.040 V vs Standard Hydrogen Electrode

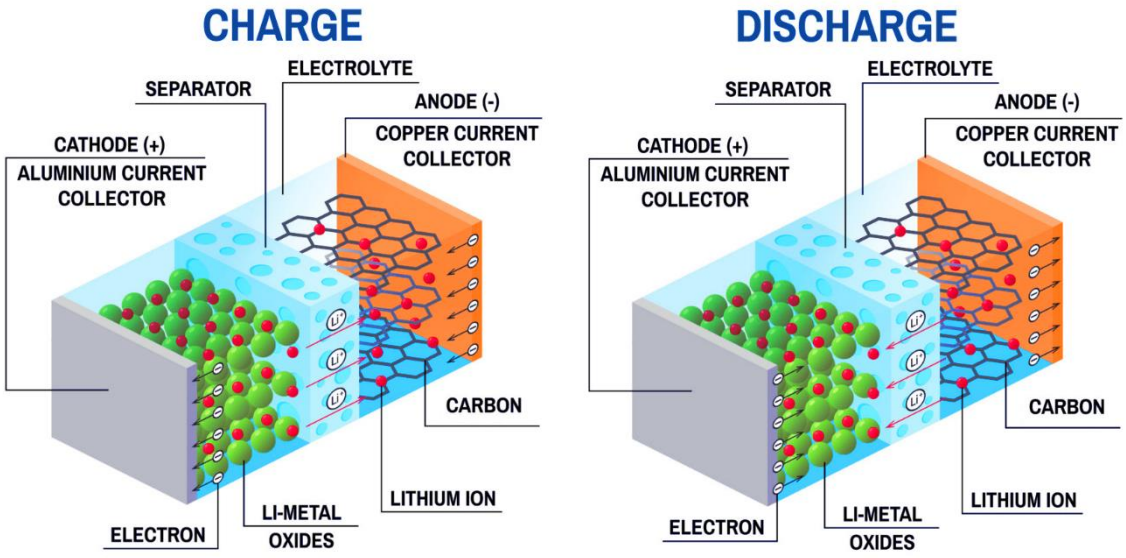

Figure 1-4 Components and operation of a standard commercial LIB. The typical architecture consists in a graphite anode, a lithium metal oxide cathode, and an electronically insulating separator, soaked in electrolyte. On the left, the charging mechanism; on the right, the discharge path.

- SHE or 0 V vs Li/Li^+) but was discarded because dangerous and not stable to humidity and oxygen. The separator is a multilayered plastic (Celgard® is the most widespread) which prevents the short-circuit between anode and cathode and is permeable by the electrolyte. The electrolyte is a mixture of organic solvents in which a lithium salt is dissolved, with the role of allowing the ionic transport between the electrodes, whilst being electronically insulating. The working principle is the reversible migration of Li^+ ions between anode and cathode, as shown in Figure 1-4. During the charge mechanism, Li^+ ions migrate from cathode to the anode. The charge mechanism is forced by an external source which injects electrons into the device and forces the ions to intercalate in the layered carbon (high energy state), where they recombine with the electrons. When an electric load is connected, the spontaneous migration of the ions from the anode to the cathode takes place, and an electron flow onto the external circuit balances this phenomenon. The overall reaction, using graphite as an anode, is summarized in equation:

$$LiMO_2 + 6\ C \leftrightarrow Li_{1-x}MO_2 + Li_xC_6 \quad (1)$$

When this process is repeated several times, a solid-electrolyte-interphase (SEI) forms on the surface of both electrodes [15]. The SEI is a thin film forming on the surface of the electrodes consequently to few charge/discharge cycles and is a result of chemical reactions between the electrolyte and the electrode. This interlayer is a passivation film that forms by reaction between the surface of the electrode and the electrolyte upon cycling. A stable SEI is fundamental for the cell functioning and has the role to protect the electrode materials from further decomposition reactions with the electrolyte, thus assuring the overall efficiency of the cell.

1.2.2 LIBs ELECTRODES. LITHIATION MECHANISMS

There are different ways by which an electrode can accommodate lithium, and the characteristics of the electrodes determinate the overall functioning of the cell, its working potential and its capacity. These different mechanisms can be summarized in three groups, namely insertion or intercalation materials, alloying materials and phase conversion materials [16,17], as depicted in Figure 1-5 [18]. Insertion electrodes represent a fundamental mechanism of electrochemical batteries. Graphite, TiO_2 and most commercial cathodes are the most representative examples [19]. During the intercalation/de-intercalation process, lithium diffuses inside the crystal structure, causing phase changes. This translates in an increase of the stacking distance in the case of graphite, while TiO_2 undergoes a crystal phase transition upon lithium intercalation, leading to lithium titanate [20]. The peculiarities of this class of electrodes are the low volumetric expansion, the minimal voltage gap between discharge and discharge process (overvoltage) while exhibiting relatively low energy densities, typically below 400

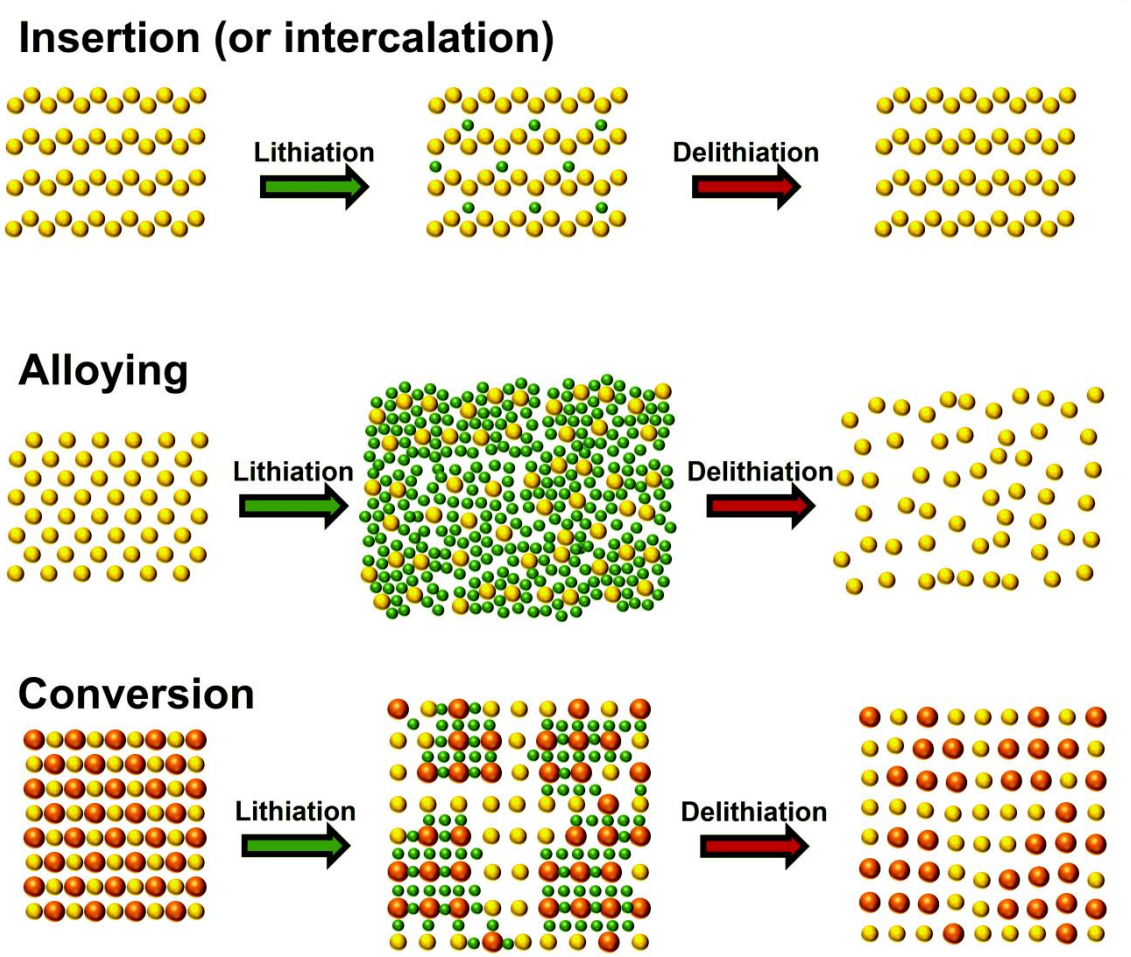

Figure 1-5 Three major lithium uptake mechanisms. From top to the bottom: intercalation of lithium between planar graphitic or titanates structures; lithium alloying in elements like silicon or tin; conversion of metal oxides or chalcogenides into their relative lithiated compounds

mAh/g, due to the limited lithium uptake this class of electrodes can undergo, hindered by its own mechanism [21]. Another issue is the low electronic conductivity of these materials; apart from graphite, TiO_2 and $Li_{1-x}MOs$ display low conductivity and need the addition of a conductive agent in order to work properly. The second lithium uptake mechanism is represented by alloying materials. This class of compounds usually undergo significant structural changes upon lithiation, mostly because of the important stoichiometry that these alloys can achieve (e.g., $Li_{4.4}Sn$ or $Li_{3.75}Si$). These materials (mostly group 13-15 species) can reach high capacities, at the price of extreme volumetric change (up to 400%, while intercalation materials do not exceed deformations above

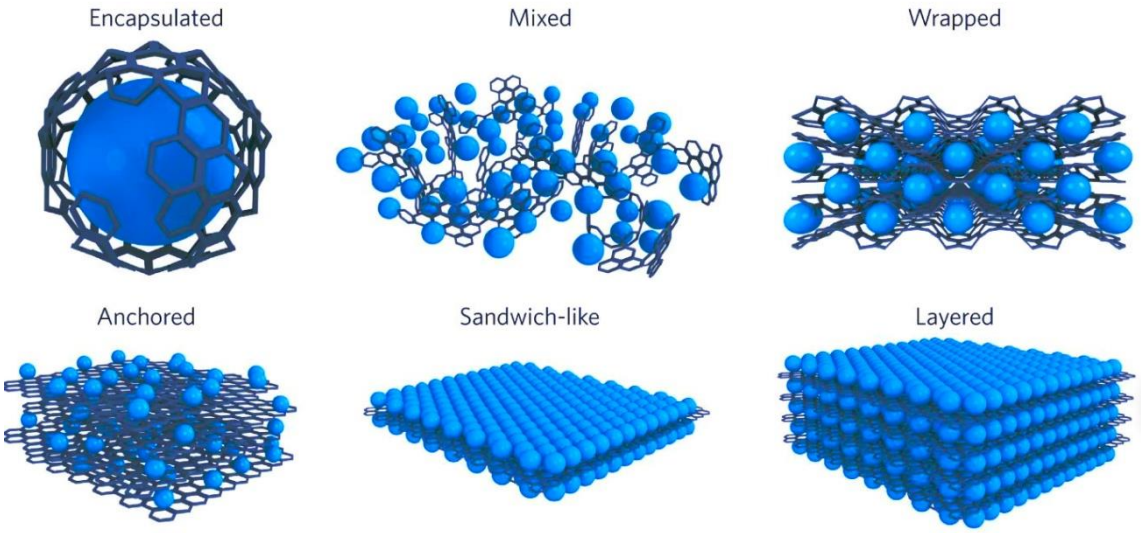

Figure 1-6 Examples of carbon-scaffolded particles

25%) and undergo detrimental effects like fracturing and pulverization. This can lead to a cycle of SEI formation, causing the consumption of large quantities of lithium ions and decomposition of electrolyte components, resulting in an irreversible loss of capacity, which is the main issue to be addressed when dealing with this set of materials. Possible solutions may include incorporating the active material in a scaffold, as schematized in Figure 1-6 [22] (e.g. porous carbon) that may accommodate the expansions, or nano-sizing the material to reduce the fracturing phenomena, or encapsulating the active material with a coating preventing direct contact with the electrolyte [17]. The third class of lithium-storing electrodes are conversion materials. During the cycling process, the active material undergoes a cycle of redox reactions. These materials offer capacities in the range of 600-1700 mAh/g, because each redox step is balanced with an important electron flow. A representative active material for this class of compounds is sulfur, which can convert from the elemental state (S_8) up to Li_8S. The downside of this class of electrode materials is that theoretical performance are hindered by their complex transformation mechanisms, leading to hard to manage systems. Some of the species

obtained during the redox conversion are soluble in the organic solvents used as electrolytes or electronic insulators (which makes a conductive scaffold necessary), thus prone to polarization effects. This may lead to important overvoltages, which is an energy-expensive feature that is not welcome in electrochemical system that already achieve close to 100% charge/discharge efficiency. Still, if these issues were to be addressed correctly, this class of materials is expected to be absolutely promising [23,24].

1.2.3 ELECTROLYTES. COMPOSITION AND ROLE

Electrolyte has the role of allowing the ionic transport between the anode and the cathode, namely the lithium ions transfer. In commercial devices liquid electrolytes are employed, but in recent years, polymeric and ceramic electrolytes are gaining interest due to their safety and the prospect of all-solid-state batteries, even though their wide commercialization has to overcome several issues, such as interface contact and ionic conductivities still not comparable to liquid ionic conductors [25]. Liquid electrolytes, in fact, offer all the properties a LIB needs, like high transfer rate, low viscosity, electronic insulation and a wide stable voltage to ensure operative flexibility to the finished device, at the price of safety and thermal stability, since organic electrolytes are inflammable. The typical LIB electrolyte solvents are mixtures of short chain or cyclic carbonates in which an appropriately soluble lithium salt is dispersed. The most used solvents are ethylene carbonate (EC) and dimethyl carbonate (DMC), but also propylene carbonate (PC) and diethyl carbonate (DEC) find use in appropriate situations [26]. Different LIBs chemistries may require different electrolyte families and combinations, as it will be discussed in chapter 2.2.2, where ether-based electrolytes will be discussed. As for the electrolyte salts, the requirements are a good solubility in the liquid media (in order to improve ionic mobility), and a sterically hindered and non-coordinating anion. The most common lithium salts are lithium hexafluorophosphate ($LiPF_6$), which replaced lithium hexafluoroarsenate for obvious safety reasons, and lithium bis(trifluorosulfonyl)imide

(LiTFSI) [27]. Some electrolyte mixtures have become standards in the industry and research field, just like LP30, the most common electrolyte for LIBs, consisting of a 50/50, v/v mixture of DMC and EC with 1 M $LiPF_6$ dissolved in. In this electrolyte lithium ions are coordinated in a tetrahedral environment of carbonate oxygen atoms, and this offers a good shielding from the sterically unwieldy anion, thus promoting the mobility and ionic conductivity of the electrolyte [28,29]. Many combinations of solvents and salts in different proportion are available, and lots of additives can be added to improve the electrolyte performance. Usually, additives can improve the SEI formation, or forming a SEI of their own, by creating a thin passivation plating on one or both the electrodes. The most commonly employed are vinylene carbonate, fluoroethylene and lithium nitrate [28,30].

1.2.4 SEI. CHARACTERISTICS AND FUNCTIONS

SEI is a fundamental part of a working LIB, although it is not already completely understood yet [31,32]. During the standard operations of a LIB, the SEI mostly forms on the reductive electrolyte-anode interface, passivating it. All the exposed surfaces of the electrodes undergo this transformation, and their complete reaction provides stability to the cycling of the cell, preventing further degradation. The most established theory about SEI was introduced over forty years ago, but still explains the mechanism properly, namely that the SEI is formed by degradation compounds, mostly in the form of inorganic salts that act as a solid electrolyte, buffering the electrode-electrolyte interface. These inorganic salts have a patterned structure, showing a mosaicity of the different phases, which include oxides, fluorides, carboxides and alkoxides, along with polymeric decomposition structures. According to this model, the organic polymeric interphase,

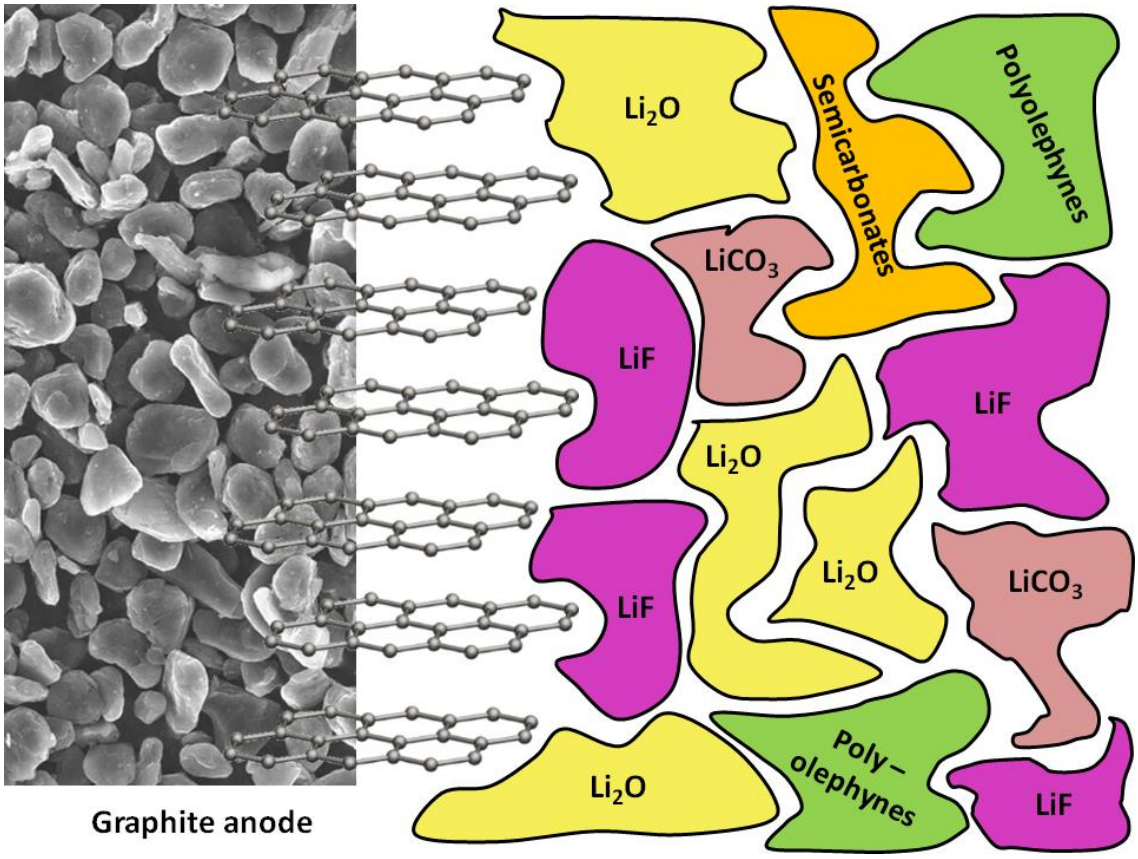

Figure 1-7 Schematic model of SEI components, both inorganic and organic are shown as separate domains. The most established theory proposes possible ionic pathways through grain boundaries. All main chemical species composing SEI are represented in the figure.

which presents a porous permeable structure, forms after the inorganic SEI, thus creating an overlayer, which stands upon the salt interphase forming from the very first cycles of the device [33]. In this structure, shown in Figure 1-7, electrons have to travel across a dielectric SEI formed by insulating materials, hence the ionic conductivity is allowed through the grain boundaries, suggesting a double-pathed mechanism, in which lithium ions diffuse through the organic SEI and then move around the salt domains to reach the electrode [34]. As previously discussed, most of the SEI forms at the anode-electrolyte interface, while the cathode forms much less interphase. This was explained in terms of working voltage and molecular orbitals relative energies. If the lowest unoccupied molecular orbital (LUMO) of the electrolyte components (e.g., lithium

hexafluorophosphate and organic carbonates) is at a higher state of the highest occupied molecular orbital (HOMO) of the electrode, the cell will be stable upon cycling. When the redox potential exceeds the voltage stability window of the organic electrolyte, decomposition reactions start to occur, leading to SEI formation. Cathode materials are characterized by high energy gaps (E_g), within which the voltage window of the electrolyte stands, thus the SEI formation at the cathode interface is often almost negligible. Low voltage anodes (e.g., Li metal, silicon, graphite), on the other hand, usually do not match their gaps with the electrolyte stability voltage, thus leading to a large SEI formation. This large SEI formation is not observed in high voltage working anodes (like TiO_2) since their characteristic potential lays within the HOMO lower limit of the organic carbonates. This interlayer buffers the difference between the E_g of the anode and the LUMO of the electrolyte, allowing proper and stable cycling and preventing continuous decompositions. Since components of SEI are formed by reaction of electrolyte components, a large amount of literature has been developed upon theoretical and experimental studies to investigate the phenomenon, leading to a more accurate understanding of this complicated mechanism [35–37].

1.2.5 OTHER LIBS COMPONENTS

Apart from components having a specific electrochemical role, a standard LIB has several different components, each with a peculiar role. Of these, current collectors, conductive agents, binders, separators and casings are fundamental but need proper tailoring, since all additions increase the weight of the device, undermining the specific energy of the final battery. Current collectors are metal foils upon which the electrodes are cast and laminated. The typical cathode collector is aluminum foil, chosen for its versatility and low cost, but it cannot be employed as a support for anodes, because at low voltage (about 0.15V vs Li/Li^+) it can alloy lithium, causing the deterioration of the collector upon cycling. The expensive copper foil is used for anode back contacts because it can

withstand Li alloying, even though it cannot be employed as cathode collector because at the potential typical cathodes work (above 3.5V vs Li/Li^+) Cu can be dissolved into the electrolyte. Conductive agents are always employed in combination with dielectric electrode active material, mostly cathodic $Li_{1-x}MOs$ and insulating anodes (e.g., TiO_2), in order to provide a conductive matrix to the active particles. Carbon black (CB) is a class of compounds obtained by incomplete combustion of heavy hydrocarbons with the right characteristics of surface area, electronic conductivity and convenient price. Binders traditionally are polymer chains that are dissolved in an organic solvent along with the rest of the electrode components, in order to cast and spread the active materials onto the current collector. When the solvent is dried, the binder chains maintain the electrode stuck together and on the metal foil. Typical binders are polyvinylidene fluoride (PVDF) and polyacrylic acid (PAA) and are dissolved with N-methyl-2-pyrrolidone (NMP). In recent years, research laboratories have been proposing hydrophilic binders, such as carboxymethyl cellulose and alginates, but these water soluble polymers are not being employed in the industry yet [38,39]. Separators are multi-layers plastic fibers of polyethylene (PE) and polypropylene (PP) that provide electronic insulation between the opposite electrodes, whilst being permeable to the carbonate-based electrolyte and allowing ionic passage. Other separators, mainly for non-lithium batteries, or water based electrolytes, can be made of glass fiber or many other materials [40]. Casings are often made of stainless steel for commercial lithium-ion batteries and coin cells, while high power to weight cells (pouch and prismatic) have a plastic casing in which these are singularly manufactured, and a hard plastic or metal container that contains the whole pack.

1.3 THE ROLE OF CARBON IN LIBS

As aforementioned, carbon has many important roles in a LIB. It can constitute the anode, in the form of graphite, which is the leading commercial anode since the commercialization of LIBs because of its good capacity and its very low voltage of lithium intercalation (about 0.25 V vs Li/Li^+), which is also the cause of important SEI formation [41,42]. Conductive carbon (e.g., carbon black, acetylene black, …) can also be used as a conductive agent to make insulating active materials available. Many efforts are being accomplished in order to employ carbon-based functional materials both as electrode materials and inactive components (e.g., scaffolds for active materials and separators components among others). An interesting class of carbon materials for battery applications has been identified in carbon nanostructures, in which graphene is the most versatile and impactful [43]. Graphene is a two-dimensional sp^2 single layer of carbon, disposed in a honeycomb hexagonal pattern. It is the fundamental component of graphite, which is a periodical stacking of graphene sheets. It is characterized by a high specific surface area (SSA) and a good electronic conductivity, making it a good candidate both as an electrode material and as a technological adjuvant in terms of high SSA, conductive scaffold. These peculiar properties suggest that graphene may solve many open issues that characterize some novel troublesome battery chemistries, allowing its use as a conductive matrix that can host active material in its wide surface area. Many different synthetic approaches have been investigated [44] since this engaging material entered the academic debate [45], and each synthetic route obtains different properties and allows a maximum scaling of the process. In this work, graphene-related materials obtained via scalable methods were employed as support materials for LIBs which exploit three different non-conventional chemistries.

1.4 AIM OF THE PROJECT

As previously discussed, batteries will have a leading role in the green transition, but some limitations have to be overcome to make the technology scalable also for high-scale static employment, such as domestic and industrial accumulators. Based on this premise, a strong need for new, reliable, high-capacity electrodes and novel battery chemistries can be sensed. The aim of this project is to solve some limitations bound to the current chemistry of commercial LIBs by exploring noncommercial and non-conventional lithium intercalating materials. The focus of the current work is to explore different electrodes that are already known in scientific literature as promising battery materials, but are still almost absent on the market, due to challenges that are yet to be overcome. In this thesis, the properties of carbon nanostructured materials are exploited to solve these so far unsolved issues. The chemistries that will be explored and discussed are:

- Lithium - titanium dioxide batteries. The aim of this work is to obtain finely dispersed TiO_2 nanoparticles (NP) to overcome the low conductivity of the material and using a good conductive agent to allow good performance of the system and allow high-rate charge/discharge cyclability. In this chapter, graphene acts both as a nucleation site to obtain nanosized particles and as conductive matrix to allow fast cycles.
- Lithium - sulfur batteries. This is the only cathodic system explored in the current work. Like in the TiO_2 case, sulfur needs a conductive matrix to overcome its dielectric nature and to improve material utilization and cycling stability. In addition, a high surface area scaffold can anchor and disperse the active material, and act as a barrier to polysulfide shuttling, by confining the redox intermediate products that have an appreciable solubility in the electrolytes commonly used in these systems.
- Lithium - silicon. This is the most mature technology among the three. In this part of the work, a synthetic effort was deployed to obtain silicon NPs small enough

to sustain and mitigate the fracturing and pulverization that normally happens in the alloying phase. Graphene was added as a conductive host, both for its important conductivity and for its porous structure, able to confine eventual debris that could form upon long and reiterate cycling.

2 NEW TECHNOLOGIES IN LITHIUM BATTERIES

In this chapter, the three systems studied in the thesis are explained and discussed, both in terms of materials, working principles and open issues. The first presented system is titanium dioxide, which was the subject that was studied more in depth during this thesis.

2.1 TITANIUM DIOXIDE BATTERIES

In this section, a brief introduction about titanium dioxide materials is presented. In the first part, the physicochemical properties of titanium oxide are discussed, along with the synthesis employed in the production of titanium-based compounds. Its application in LIBs is disserted in the second part of the chapter, with a focus on the working principles and the problems related to TiO_2-containing LIBs.

2.1.1 TITANIUM DIOXIDE – PROPERTIES AND SYNTHESIS

Titanium dioxide (or titania), as aforementioned, is a large gap semiconductor. It is a binary compound that can be found in nature mainly in three polymorphs, namely anatase, rutile and brookite. Titania has been widely investigated in all its forms and for a plethora of applications, which harness both its optical and electrochemical properties. To name a few, titania has been employed as photodegradation catalyst for pollutants, as pigment for paint (E171) and as UV filter, for photovoltaics thin films and NPs, sensors and, lately,

for electrochemical storage [46–51]. Apart its important performance in all the cited applications, TiO_2 stands as a good candidate for large scale applications due to its

Table 2-1 Structure and characteristics of titanium dioxide polymorphs

Structure	Space Group	Density (g/cm^3)	Lattice Parameters
Anatase	Tetragonal I41/amd	3.90	a=3.78 Å, c=9.51 Å
Rutile	Tetragonal P42/mnm	4.25	a=4.59 Å, c=2.96 Å
Brookite	Orthorombic Pbca	4.12	a=9.18 Å, b=5.45 Å, c=5.15 Å
TiO_2-B	Monoclinic C2/m	3.73	a=12.18 Å, b=3.74 Å, c=6.52 Å, β=107.1°
TiO_2-II	Orthorombic Pbcn	4.33	a=4.52 Å, b=5.50 Å, c=4.94 Å
TiO_2-III	Monoclinic P21/c	5.09	a=4.59 Å, b=4.85 Å, c=4.74 Å β=98.6°
TiO_2-H	Tetragonal I4/m	3.46	a=10.16 Å, c= 2.97 Å
TiO_2-R	Orthorombic Pbmn	3.87	a=4.90 Å, b=9.46 Å, c=2.96 Å

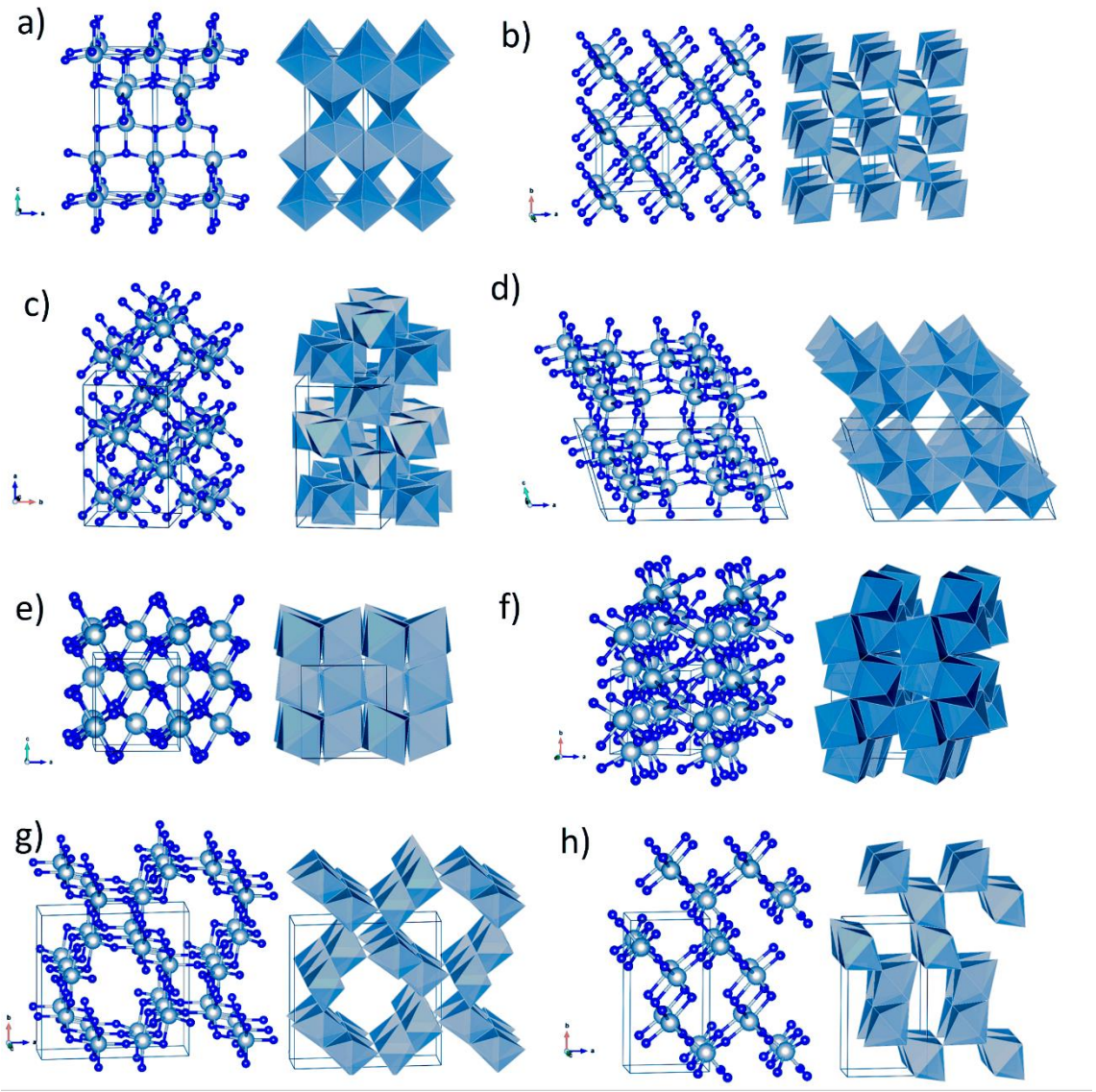

Figure 2-1 Crystal structures of a) Anatase, b) Rutile, c) Brookite, d) Bronze, e) Columbite, f) Baddeleyite, g) Hollandite and h) Ramsdellite phases

physicochemical stability, relative abundance in the earth crust and consequent low cost and theoretically absent toxicity, only related to eventual form factors (e.g. titania nanotubes) [52]. In all the aforementioned allotropes, a Ti atom is coordinated by six oxygen atoms, forming the TiO_6 octahedron; in the different polymorphs, the relative

positions of the octahedral differ, while the fundamental TiO_6 structure remains unaltered. In addition to the three most common polymorphs, other more exotic structures can be found, like TiO_2-B (bronze), which has grown interest lately because of its lithium intercalation properties. Other phases, like, TiO_2-II (columbite) and TiO_2-III (baddeleyite) can be only synthetized at high pressure conditions [53]. Other structures like TiO_2-H (hollandite) and TiO_2-R (ramsdellite), are of interest mostly in fundamental research [54]. In table 2-1, a summary of the titanium dioxide allotropes can be found. Anatase is a metastable structure that can be converted in the termodynamically favorable rutile when heated above 650°C, transitioning from a corners-sharing tetragonal structure to an edge-sharing tetragonal disposition. Brookite is also metastable like anatase, but the octahedron in this case, shares both edges and corners, resulting in a orthorhombic structure. All TiO_2 structures have slightly different atomic distances, thus resulting in different densities and electronic band structure. In fact, anatase, rutile and brookite are n-type semiconductors, and the band gap slightly changes between the allotropes. In fact, anatase has a band gap of 3.20 eV, similar to brookite (~3.2 eV) while rutile has a bandgap of 3.02 eV. The main source of titanium dioxide is mineral extraction, mostly by ilmenite ($FeTiO_3$). The mineral is treated with chlorine gas in presence of carbon at a temperature above 900°C, following (2).

$$FeTiO_3 + 7/2\ Cl_2 + 3\ C \rightarrow TiCl_4 + FeCl_3 + 3\ CO \qquad (2)$$

Titanium tetrachloride is a fundamental intermediate from which almost all the titanium industry branches out. This intermediate is strongly reactive, and titanium dioxide can be easily obtained if the precursor is exposed to air moisture, hydrolyzing as

$$TiCl_4 + 2\ H_2O \rightarrow TiO_2 + 4\ HCl \qquad (3)$$

or oxidizing if exposed to atmospheric oxygen.

$$TiCl_4 + O_2 \rightarrow TiO_2 + 2\ Cl_2 \qquad (4)$$

This is also the intermediate for the titanium metal industry, and it is obtained via the Kroll process, explained in (5),

$$2\ \mathrm{Mg} + \mathrm{TiCl_4} \rightarrow 2\mathrm{MgCl_2} + \mathrm{Ti} \qquad (5)$$

using molten magnesium as reducing agent to obtain metallic titanium. The hydrolysis of titanium tetrachloride permits to obtain also important compounds known as titanium alkoxydes, which are employed in research and industrial processes to obtain nano-scaled titanium dioxide. In fact, many approaches have been proposed to obtain nanosized TiO_2. The sol-gel method is the most used technique, and it allows to achieve nanocrystals without any contaminating byproducts. The technique consists in the hydrolysis and condensation of the precursor, to form a colloid named *sol*. The modulation of the reaction parameters can influence the properties of the product, and a flourishing literature is already available on this subject [55,56]. Another route that employs titanium alkoxides is the hydrothermal synthesis, that exploits high temperature and pressure to obtain TiO_2 nanocrystals. In this synthesis, the organotitanate is inserted in an autoclave along with water and sealed. The typical reaction involves temperatures above 100°C, leading to a saturated steam pressure inside the reactor, causing the hydrolysis of the precursor and the production of nano-TiO_2.

2.1.2 TITANIUM DIOXIDE IN LIBS

Titanium oxide materials have been studied as a possible LIB anode for a couple of decades thanks to its characteristic of being stable, safe and abundant material. Lithium titanate ($Li_4Ti_5O_{12}$, LTO obtained by the reaction between Li_2O and TiO_2) is already available as an anode in commercial LIBs. It has a theoretical capacity of 175 mAh/g, related to the intercalation reaction highlighted in (6).

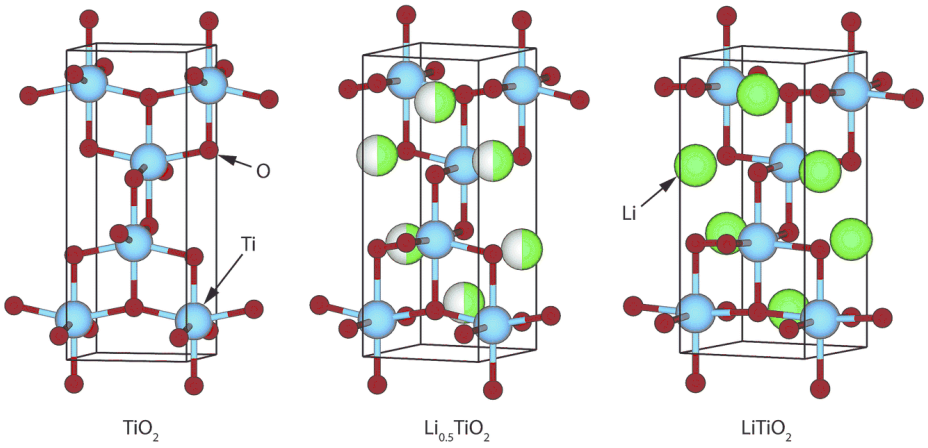

Figure 2-2 Evolution of the crystal structure of tetragonal anatase (on the left), to orthotombic lithium titanate (center) and the irreversible fully lithiated $LiTiO_2$ tetragonal phase. The half-filled green spheres represent intercalation sites that have the same probability to be either occupied or unoccupied by a lithium ion.

$$Li_4Ti_5O_{12} + 3Li^+ + 3e^- \leftrightarrow Li_7Ti_5O_{12} \qquad (6)$$

The capacity is related to the intercalation of 3 moles of Li^+ for each mole of LTO. During this process, a negligible 0.5 % volume expansion of the anode is registered, since the spinel-like structure of the material can host additional lithium cations without deforming its structure. In addition, the insertion takes place at about 1.5 V vs Li/Li^+, preventing the formation of a large SEI like in the case of carbon-based anodes. These properties ensure a good rate capability and lack of capacity loss during the operations of the device [57]. More recently, also titanium dioxide TiO_2 has been studied as well as a possible anode for LIBs. Of the examined polymorphs, anatase, brookite, rutile and TiO_2-B are being detected as good candidates for their electrochemical properties [58,59]. In fact, as shown in Figure 2-1 [60], these polymorphs have interstitial voids that can accommodate the small Li ions (structures a,b,d). Rutile can intercalate Li ions, but the process is negligible at room temperature for kinetical factors and proper intercalation only takes place at about 120°C, making it less interesting for practical applications in LIBs [61]. Anatase, on the other hand, can accommodate lithium ions at room temperature, making it one of the most interesting allotrope in LIBs for its satisfying lithium mobility and facile syntheses. In

anatase, the intercalation process is accompanied with a phase transition imposed by the electrostatic repulsion between lithium ions, while volume only expands by 4% [62]. The intercalation process can be observed at about 1.7 V vs Li/Li^+ with a theoretical capacity of 335 mAh/g, which corresponds to the fully lithiated form shown in (7)

$$TiO_2 + x\ Li^+ + x\ e^- \leftrightarrow Li_xTiO_2 \qquad (7)$$

$$\text{with } 0 \leq x \leq 1$$

During the discharge process, the Li cations intercalate inside the tetragonal anatase crystal lattice, resulting in a phase shift of the anodic material to an orthorhombic phase of lithium titanate. During this reaction, titanium reduces from Ti^{4+}, reaching Ti^{3+} when 1 mole of lithium is fully intercalated in the crystal structure. In order to maintain this process reversible, the lithiation of the anode cannot undergo complete intercalation but reaches its maximum at the stoichiometry $Li_{0.5}TiO_2$, resulting in a lithium titanate with an orthorhombic structure. Given the theoretical capacity of 335 mAh/g, the halved stoichiometry can grant 168 mAh/g [63–65]. One key factor to obtain performing TiO_2 anodes is the nanosizing of the active material. In fact, the ionic passage is only allowed through the empty channels of the anatase structure, and is characterized by a chemical diffusion coefficient of about 10^{-11} cm^2/s. For this reason, the nanosizing of the particle is accredited as a possible solution to the low lithiation kinetics. Another issue to be addressed is the low electric conductivity of anatase (10^{-12} S cm^{-1}), which is traditionally addressed with the mix of the anatase crystals with a conductive agent, traditionally carbon black [66]. To overcome these limitations, a cornucopia of solutions has been proposed. One approach is the tailoring of TiO_2 nanostructures, which allows to buffer the low ionic mobility issues and to maximize the electrical contact with the surrounding conducting agent. An array of possibilities opens, ranging from 0D TiO_2 to 1D, 2D, and 3D structures [67]. Another possible approach is the design of the conductive agent. Studies show how the introduction of metals, metal oxides, and carbon materials may improve the electrochemical performance of TiO_2. Still, most solutions offer great results

but show expensive drawbacks, employ toxic or carcinogenic materials (e.g., carbon nanotubes or V_2O_5), or need intricate synthetic steps [68]. Despite these complications, LTO batteries are already on the market, with packs with capacities ranging from 1.8 mAh up to 65 Ah. Toshiba is currently commercializing a LTO battery with the commercial name of Super Charge Ion Battery (SCiB^{TM}) due to its characteristic of recharging 90 % of its capacity in 10 minutes [69].

2.2 LIHIUM/SULFUR BATTERIES

Herein, a discussion about sulfur and its chemistry is presented, then its employment in LIBs will be discussed. In the first part, the properties and synthesis of the materials will be disserted, and subsequently the role and issues of sulfur-based LIBs will be expanded.

2.2.1 SULFUR – PROPERTIES AND SYNTHESIS

Sulfur is an interesting atom. Like titanium dioxide, sulfur can arrange in different allotropic structures, and it tends to naturally form single bonds within itself. For this reason, its most stable arrangement is in cyclic form, with formula S_8. This eight-membered crown-like ring can have different packing symmetries; the best known are the thermodynamically favorable orthorombic α phase and the monoclinic β phase, which is formed when sulfur is crystallized above 100°C and then cooled rapidly. If the sulfur is melted and then is allowed to cool slowly, another eight-membered ring allotrope is obtained, this time with a monoclinic spatial distribution, resulting in a higher density. All allotropes have low solubility in common organic solvents (in the range of mg per liter) and are excellent thermal and electrical insulators (~$5 \cdot 10^{-4}$ S/cm) [70]. Other structures that sulfur can aggregate into are polymers and linear, cyclic or branched structures with different chain lengths. The favored species depend on temperature and

pressure conditions. Another peculiarity of sulfur is its capacity of forming a high number of polysulfides with electropositive elements (Li, Na, K, Ba, …) [71,72]. Many of these compounds have been studied and characterized, and this phenomenon can be exploited in lithium sulfur batteries. The production of sulfur in its elemental state is almost completely obtained from the petrol industry. In fact, sulfur comes as a byproduct of the oil and coal industry during the purifying stage, making it available in large quantities and at a low cost. It comes from the stripping of sulfur hydride (H_2S), following the Claus process, that follows (8) and (9).

$$H_2S + 3/2\ O_2 \rightarrow SO_2 + H_2O \quad (8)$$

$$2H_2S + SO_2 \rightarrow 3S_2 + 2H_2O \quad (9)$$

Another available route is the extraction of sulfur as a byproduct of the purification of ferrous minerals. Its importance is mainly related to the production of sulfuric acid, which is relevant on its own and as precursor of phosphates, employed as fertilizers. Other interesting sulfur compounds are mercaptans (odorous molecules added to domestic gas to help locate leakages), polysulfides and sulfur oxoanions.

2.2.2 Sulfur in Li/S batteries

Sulfur has been proposed as a cathode for lithium batteries. Research on cathode materials is more challenging and slower as compared to the outstanding materials that have been proposed as high capacity and high energy anodes (e.g., Li metal, silicon, …). Commercial cathodes have capacity non exceeding 200 mAh/g, thus creating a mismatch between anodes and cathodes and a barrier in overcoming current Li ion batteries energy densities. In addition, commercial cathodes often employ toxic and costly metals, often found in third world country mines. This promoted the scientific research for new chemistries in lithium batteries, with the proposal of innovative such as lithium-sulfur

Table 2-2 Comparison between commercial cathodes and sulfur in terms of performance and price

Cathode Material	Voltage (V)	Capacity (mAh/g)		Energy Density (Wh/kg)		Price (USD/kg)	Cycle Life
		Theoretical	Practical	Theoretical	Practical		
$LiMn_2O_4$	3.7	148	110-120	420	120	15	300
$LiCoO_2$	3.6	274	110-140	510	180	30	400
$LiFePO_4$	3.6	170	150	578	130	10	1000
S	2.2	1675	-	2600	-	0.57	-

batteries. Sulfur, with its theoretical capacity of 1675 mAh/g and energy density of 2600 Wh/kg (five times higher than a $LiCoO_2$ battery), is proposed as a groundbreaking technology [73–75]. These performance are fueled by the reaction between sulfur and lithium, that involves the overall reaction expressed in (10).

$$S_8 + 16Li^+ + 16e^- \leftrightarrow 8Li_2S \qquad (10)$$

This reaction involves the breaking of S-S bonds to form Li-polysulfides. The reaction chain involves several different species, resulting from the reaction course, which are, in order Li_2S_8, Li_2S_6, Li_2S_4, Li_2S_2, and Li_2S. Every step of the conversion mechanism involves two electrons, thus granting the aforementioned capacities. The redox system is reversible, and the charge mechanism in batteries follows the reverse arrow, starting from Li_2S and reaching the elementary state again. Despite these advantages, the practical applications of the technology are hindered by several problems. Three are the most overwhelming:

1. The electronic conductivity of S_8 is almost nonexistent, orders of magnitude lower than traditional cathode material such as $LiFePO_4$ (10^{-5} S/cm) or $LiCoO_2$ (10^{-3} S/cm). Also Li_2S, the discharge products of the redox cycle is an electronic insulator [76], leading to a low utilization of the material [77].

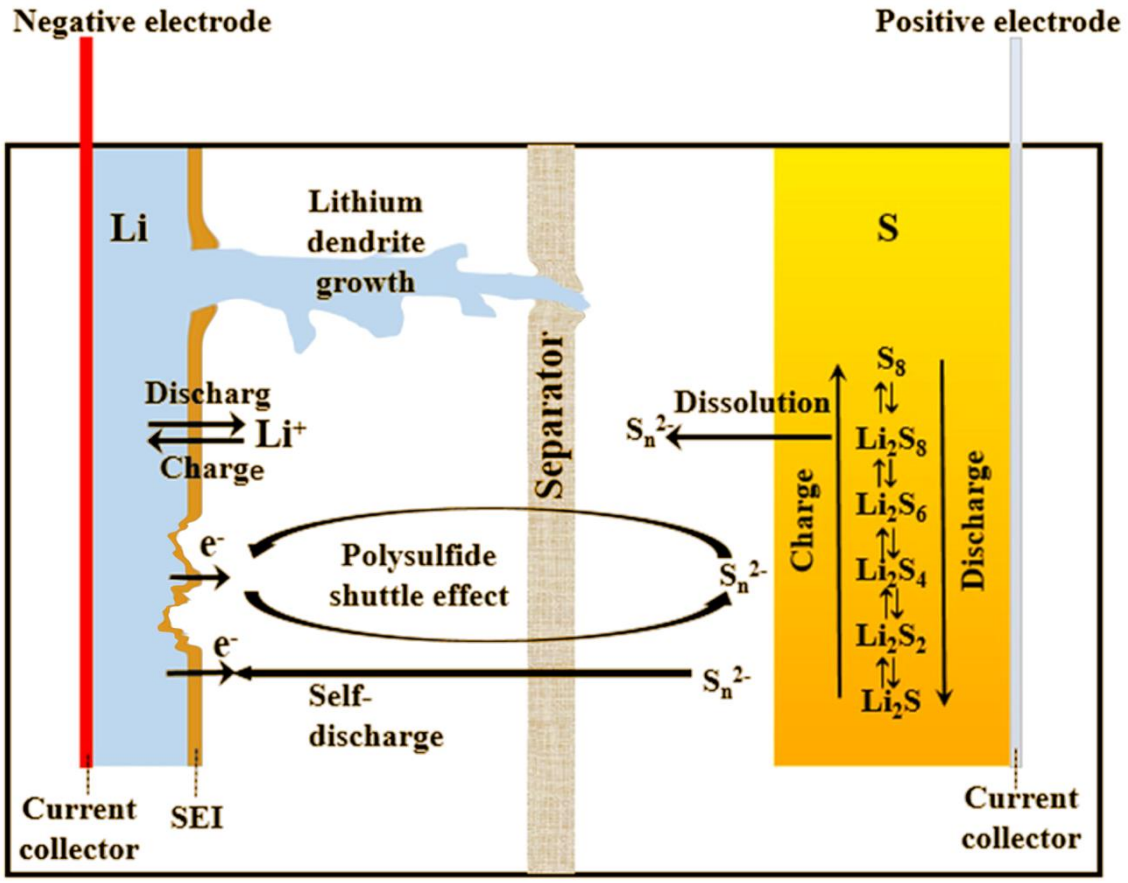

Figure 2-3 Model of a Li-S battery. On the right, the redox chain taking place on the sulfur cathode, then the polysulfide shuttle effect is shown, related to the corrosion and dendrite growth on the lithium anode.

2. Li_2S has the lowest redox kinetics in the polysulfide chain, resulting in a passivation of the sulfur electrode by this slow-reacting product.
3. During the lithiation and delithiation processes, the volume expands and shrinks of about 80% due to the different densities of molecular sulfur (~2 g/cm^3) and Li_2S (1.67 g/cm^3), resulting in a lack of stability of the electrode material [78].
4. The polysulfide intermediates (Li_2S_8, Li_2S_6 and Li_2S_4) are soluble in the liquid organic electrolyte, creating a phenomenon called shuttle effect, which is detrimental for the lithium metal anode due to corrosion and dendrite formation,

leading to premature capacity loss and lack of reversibility [79]. This effect is schematized in Figure 2-3.

5. The solubility of polysulfides also leads to loss of reversibility due to the loss of sulfur active mass in the solvent. This effect is expected to be more emphasized in research cells than in hypothetical commercial packs, the formers having a non-optimal sulfur to electrolyte ratio [80–82].
6. The different redox reactions lead to steps in the discharge voltage profile, which is not ideal for an electrode, since the stability is an important parameter in battery electrodes. The mean voltage plateau is at approximately at 2.1 V, which is detrimental to the specific energy of the whole cell.

The singular mechanism of Li/S battery can be better explained analyzing the typical charge/discharge profile of a working cell. The behavior is shown in Figure 2-4, where different regions can be observed. In fact, the chemistry of a Li/S battery, despite being complex and involving lots of side-reactions upon which the debate is still open, can be conventionally summarized as a four-stage process [83].

Stage I: elemental sulfur is reduced by means of two electrons and Li cations, forming the Li_2S_8 intermediate product. This process happens at the high voltage plateau highlighted in Figure 2-4, at about 2.3 V. Then, the lithium sulfide starts to dissolve into the electrolyte, exposing the residual S_8 and making it available for the reduction by contact with lithium.

Stage II: the reduction continues in liquid phase, where polysulfides travel across the electrolyte reaching the Li anode to push the reduction chain further. In this stage, the polysulfide chains are reduced to medium and short chain (between 6 and 4 atoms long). The voltage of the reactions is not taking place at a steady voltage, but this decreases gradually. Meanwhile, the electrolyte raises its viscosity, following the increasing of polysulfides dissolved into the liquid.

Stage III: at this stage, medium and short-chained polysulfides undergo further reduction, forming Li_2S_2 and Li_2S. This reaction happens at a well-defined voltage, and an important

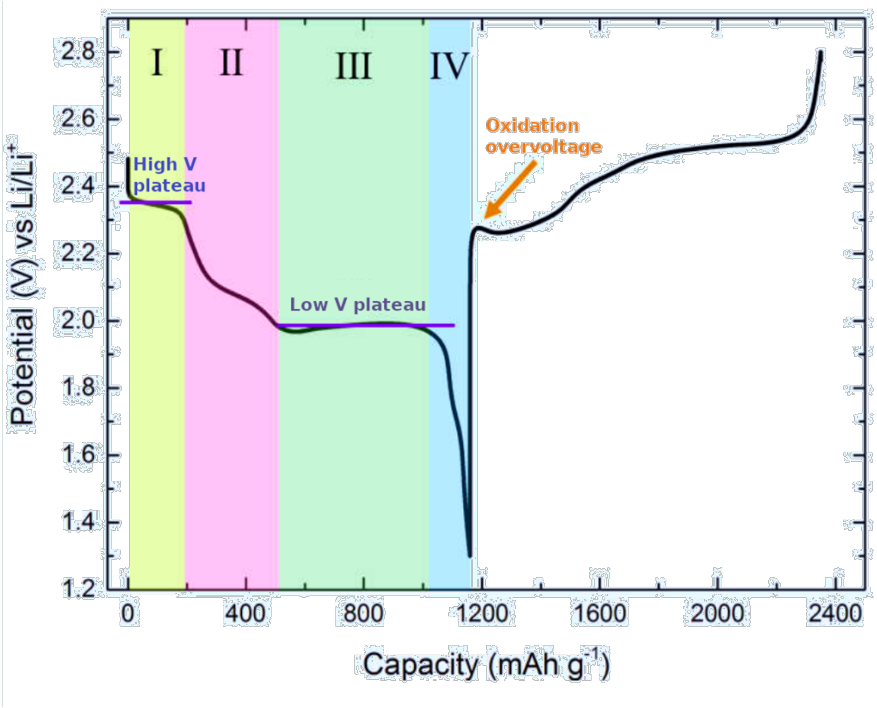

Figure 2-4 Galvanostatic charge/discharge profile of a Li-S battery. Four separate regions can be observed.

low voltage plateau can be observed at about 2.1 V. These compounds are insoluble in the organic electrolyte and deposit again on the cathodic surface.

Stage IV: is the end of the reduction chain, where all the available polysulfides are reduced to Li_2S. The voltage drops rapidly for two main reasons. On the one hand, the reduction ends, and the polarization of the device becomes explicit. On the other hand, the final stage returns at solid state, with highly dielectric species involved, thus underlining the polarization effect. During the charge process, an important overvoltage is observed. This is attributed to the oxidation of electronically insulating Li_2S, generating soluble sulfides, which then allows the liquid phase conversion steps, leading to the full oxidation of the cathode until elemental sulfur is restored. Also for Li/S batteries, there are some examples of close to commercial state; in fact “Oxis Energy”, a UK-based company already produced cells with 500 Wh/kg energy density and currently holds more than 100 patents on Li/S batteries. The cells are employed in unmanned aircraft but can

be suitable for many energy density-intensive applications, such as electric mobility, aerospace and defense [84].

2.3 SILICON BATTERIES

We are living in the Silicon Age. As our ancestors used to live in the Rock, Bronze or Iron Age, we are said to be living in the age of information (or Digital Age), which is founded on the metal-oxide-semiconductor field-effect transistor, the key component of the digital world which is mainly built on silicon semiconductor. Still, silicon is a versatile element characterized by unique properties, making it one of the most polyhedric elements of the periodic table.

2.3.1 SILICON – PROPERTIES AND SYNTHESIS

Silicon is the second most abundant element in the earth crust, composing sand, minerals and clays. It naturally occurs in form of silicon dioxide (silica) or silicates, silicon-based anions often arranged in large polymeric structures. Silicon based compounds serve many applications that do not need any chemical purifications, such as cements, bricks, glass and porcelain. Silicon in its elemental state can be produced by carbothermal reaction, by reducing SiO_2 (in the form of quartzite) with coke. In alternative, it can be carried out using aluminum as reducing agent, resulting in a aluminothermic reaction. These are summarized in (11) and (12) respectively.

$$SiO_2 + 2C \rightarrow Si + 2CO \quad (11)$$

$$3SiO_2 + 4Al \rightarrow 3Si + 2Al_2O_3 \quad (12)$$

These methods produce low quality silicon (up to 99%). To obtain semiconductor-grade material, silicon is chlorinated and the resulting tetrachlorosilane and trichlorosilane undergo fractional distillation, until a 5N purity (99.999%) is reached. Silicon in its elemental form tends to crystallize in a covalent structure with a diamond face centered cubic dress, spacegroup *Fd-3m*. From the electronic point of view, intrinsic silicon is a semiconductor with a small (1.12 eV) bandgap, that can be tuned by doping [85]. The characteristic that makes silicon interesting in LIBs is the possibility of alloying silicon with other elements. Silicon can in fact be alloyed with copper or aluminum in order to enhance some of their characteristics, and to tune their performance in peculiar applications, such as electronics, automobile castings and molds. Silicon can also be alloyed with iron, in order to tailor the magnetic properties of the so-called *electrical steel*, or to reduce the oxidation rates of stainless steel. In addition, silicon can create alloys with lithium, making it an interesting candidate as electrode for LIBs.

2.3.2 SILICON IN LIBS

As already explained, what make Si a good candidate for LIB anode is the virtuous combination among several factors, such as volumetric and gravimetric capacity, nominal working potential, stability, non-toxicity, kinetics and cost. Silicon has an impressive volumetric capacity of more than 2000 Ah/L and a gravimetric capacity of about 3500 mAh/g if calculated at full lithiation volume and weight (theoretical capacity is about 4200 mAh/g). These important capacities are common in alloying materials, but silicon has the highest theoretical capacity because it can reach a stoichiometry of $Li_{15}Si_4$ by electrochemical intercalation, which is 3.75 Li equivalents per Si atom, an extremely high ratio compared to the single Li equivalent per 6 carbon atoms of LiC_6 (specific capacity of 372 mAh/g) [86]. The phase diagram in Figure 2-5 shows that higher stoichiometries can be achieved but require metallurgical conditions. During the first alloying process, silicon undergoes a phase transition, transforming into amorphous lithium-silicon alloy

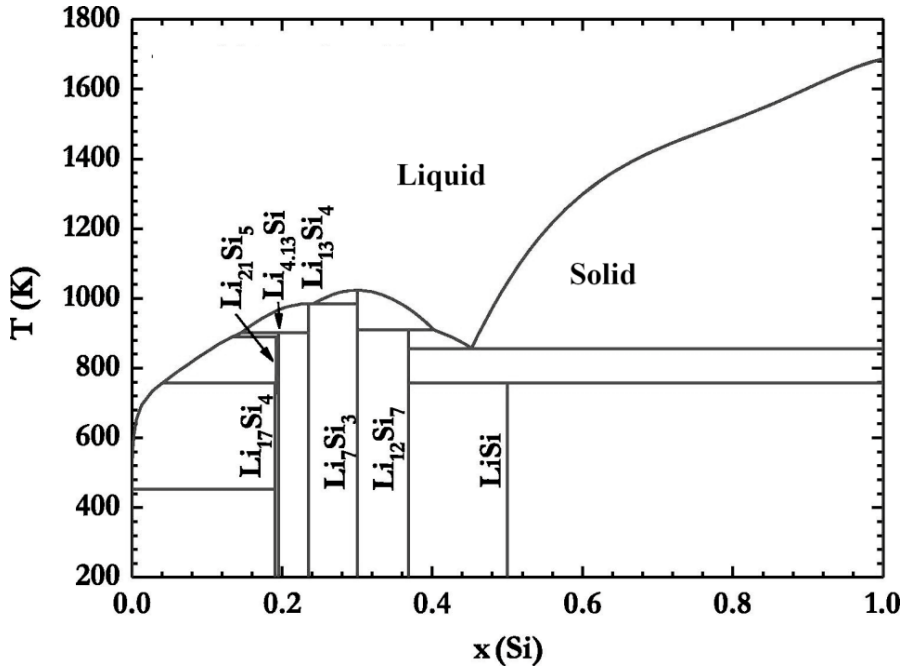

Figure 2-5 Si-Li binary alloys phase diagram.

and regaining a crystal symmetry when the potential drops below 50 mV, where the deep-lithiated $Li_{15}Si_4$ stage is reached. During the discharge phase, the lithium-silicide is delithiated back into its amorphous intermediates, until amorphous silicon is obtained. Therefore, from the second cycle, only amorphous silicon is present in the system, and the voltage profile shows major changes between the first and the second discharge. Still, Si maintains a convenient discharge profile in all the cycles, with almost all of the alloying processes taking place below 0.4 V, which is desirable since the operating voltage of a cell is the difference between the cathode and the anode working potential. In addition, silicon has almost no known toxicity, and is a sustainable material, mostly because of its abundance on the earth crust and because the purity for the battery grade material is far below the purity titles needed for electronics, making it low-cost and environmentally friendly. Unfortunately, silicon anodes have some major drawbacks that hinder its employment at industrial scale, which are summarized in Figure 2-6. One of the main

drawbacks of silicon anodes is the stability of the system. In fact, the lithiation process involves a huge expansion and the volumetric change related to (13) is up to 320%.

$$4\,Si + 15\,Li^{+} + 15\,e^{-} \rightarrow Li_{15}Si_{4} \qquad (13)$$

This swelling is typical of all alloying materials (9 ml increased volume per mole of Li, as a rule of thumb), but silicon is one of the most severe. The continuous swelling leads to the fracturing and pulverization of the active material and to the disconnection of the particle from the electrode surface (as displayed in Figure 2-6 a and b). This, in combination with the low nominal voltage of the cell, is related to an uncontrollable SEI. In fact, since the cycling conditions are ideal to trigger electrolyte decomposition and SEI formation and the fracturing of the material continuously exposes more un-passivated and highly reductive surface of the electrode, the cell hardly reaches a stabilization (Figure 2-6 c). In fact, the first cycles typically show an outstanding capacity, a combination between the high capacity of silicon and the huge SEI formation that keeps renovating in the first cycles. After the initial cycles, the SEI formation tends to stabilize, and the capacity of the electrode reaches an equilibrium. As a result of these volume fluctuations, a lot of energy is absorbed in SEI formation, and a part of active material is lost due to the fracturing of the electrode. To address these problems, many studies have been conducted, but there are three main pathways that can be summarized as:

- Tailoring of the morphology of silicon particles. Many solutions have been tested to buffer the problems related to this exceptional volume fluctuations, the most promising ones are the creation of porous silicon structures that can accommodate the volume swelling or the down-scaling of Si particles, since nano-sized particles are less susceptible to volume change related damages [87–89].
- The formulation of the electrode composition, which include the choice of the binder, the conductive agent, the solvent and their proportion in order to optimize the properties of the electrode and extend the life cycle. This can include that

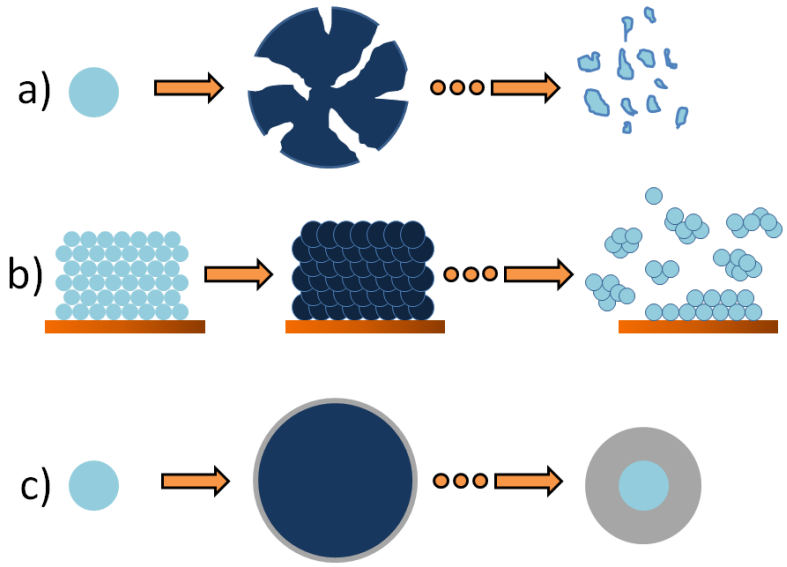

Figure 2-6 Major silicon anodes faults: a) Cracking and pulverization of the Si particles due to the swelling and shrinking upon alloying b) Anode particles detachment and disconnection from the electrode matrix and collector c) Continuous SEI formation.

promote SEI enhancing molecules [90–92] or functional conductive materials, e.g. porous carbons, with the role of confinement of the eventual pulverized silicon particles [93].

One or both of these solutions must be applied in order to achieve good performance and limit the lack of reversibility of the cell. Despite being the most promising technology, silicon-based batteries are still not available commercially, due to the problems listed beforehand. Most producers of lithium-silicon batteries are startups (Sila, Enevate, Group14, Global Graphene and Enovix among others) and the battery production is limited to niche applications [94], but the use of silicon in combination with graphite and eventually in alloys is a staple in the battery roadmap of the Battey 2030+ agenda [95].

3 CARBON NANOSTRUCTURED MATERIALS

Carbon nanostructured materials, and in particular graphene-based materials, are the *fil rouge* of this work. In this chapter, graphene and its properties are being discussed, then different synthetic methods are explained and compared. Finally, the possible roles of graphene and graphene-related materials in LIBs are explained, followed by their employment in this thesis work, with their specific role in solving the issues related to each battery chemistry already presented.

3.1 GRAPHENE

Graphene is a material that cannot exist. In fact, from theoretical calculations, it was thought that no crystalline solid could exist in only two dimensions because at any temperature different than 0 K any thermal fluctuation would cause the melting of the crystal lattice. But in 2004 Novoselov and Geim isolated a flake of single layered graphite and subsequently studied its exotic electronic transport properties, paving the way to the two dimensional world and earning them the Nobel Prize for Physics in 2010 [96]. Graphene, despite the theoretical calculations, can in fact exist thanks to curvatures and ripples that create a non-flat surface, making the material look like a nano-sized and ordered sheet of atoms. Graphene is composed by carbon atoms organized in a honeycomb lattice, where every carbon is sp^2 hybridized in an almost-planar trigonal surrounding. Graphene is a material of great interest in many fields, thanks to its extraordinary properties, given by its unique 2D structure and conjugated π bonds, which determines the overlapping of orbitals of the carbon sheet, allowing a high electron mobility, with a measured conductivity of above 2000 S/cm. This characteristic makes graphene a great electronic conductor, with an astonishing electron mobility of 200 000

$cm^2/V \cdot s$. In addition, its atomic thickness makes it almost transparent, absorbing just 2.3 % of incident light. Despite being just 0.34 nm thick (the size of a carbon atom), graphene has outstanding mechanical properties, being 200 times more resistant than steel, and its 2D properties grants a theoretical SSA of 2630 m^2/g, making it a good candidate for applications which require high specific surface materials [97–99].

3.2 SYNTHESIS OF GRAPHENE AND GRAPHENE RELATED MATERIALS

The very first studies were performed on graphene flakes isolated by micromechanical exfoliation of a graphite crystal, using Scotch Tape to separate the sheets from one to another. This method allowed the discovery of the properties of highly pure graphene sheets, which promoted the interest upon the subject of the scientific community. This method however, yields amount of material not suitable for any application other than pure research. For this reason, several methods have been proposed to obtain high quality single-layered graphene (a scheme of the different routes can be found in Figure 3-1 [100]), and the most effective quality-wise are bottom-up approaches, of which the most successful is the synthesis via chemical vapor deposition. For this method, a carbon rich gas precursor (methane or acetylene) undergoes a heterogeneous decomposition at the interface of a catalyst substrate (Cu and Ni among others), producing a highly pure and ordered sp^2 carbon sheet. This method can produce high quality, single layer graphene. However, the main drawback of this method is the product yield, that is in the range of the µg – ng, with the lateral dimension of a platelet hardly exceeding 1 mm [101]. Another high-quality bottom-up approach is the epitaxial growth, which exploits monocrystalline SiC as a precursor to obtain high quality graphene. The SiC hexagonal cell mimics the carbon arrangement in graphene (0.142 nm distance between adjacent atoms), and by aggressive thermal treatment in ultrahigh vacuum conditions (10^{-10} mbar), the superficial

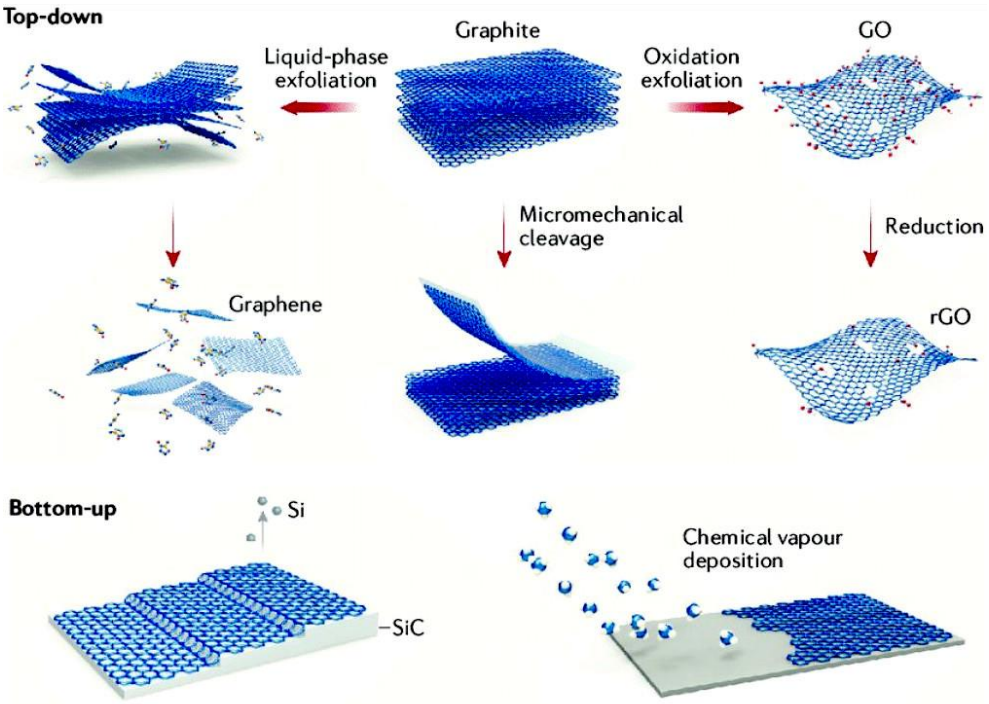

Figure 3-1 Scheme of top-down and bottom-up synthesis of graphene materials.

silicon is desorbed by sublimation and carbon undergoes a spontaneous arrangement to produce graphene in single and few layers form. This method has some issues, related to the difficult removal of the graphene sheet from the substrate and to a small amount of material, making it not suitable from an industrial and large scale employment point of view [102]. To have some scalable synthetic method, top-down approaches must be considered. These methods start from a bulk of more complex precursor that is reduced to its primitive component. The Scotch Tape method is a representative of this class of synthesis, along with the unzipping of carbon nanotubes or carbon fibers. The most interesting ones are those starting from graphite. Many physical methods have been employed, the most notable examples are the exfoliation of graphite via sonication [103–105], ball milling [106,107] or electro-exfoliation, a method that employs an applied electrical potential to intercalate ions into graphite layers, causing the expansion and the

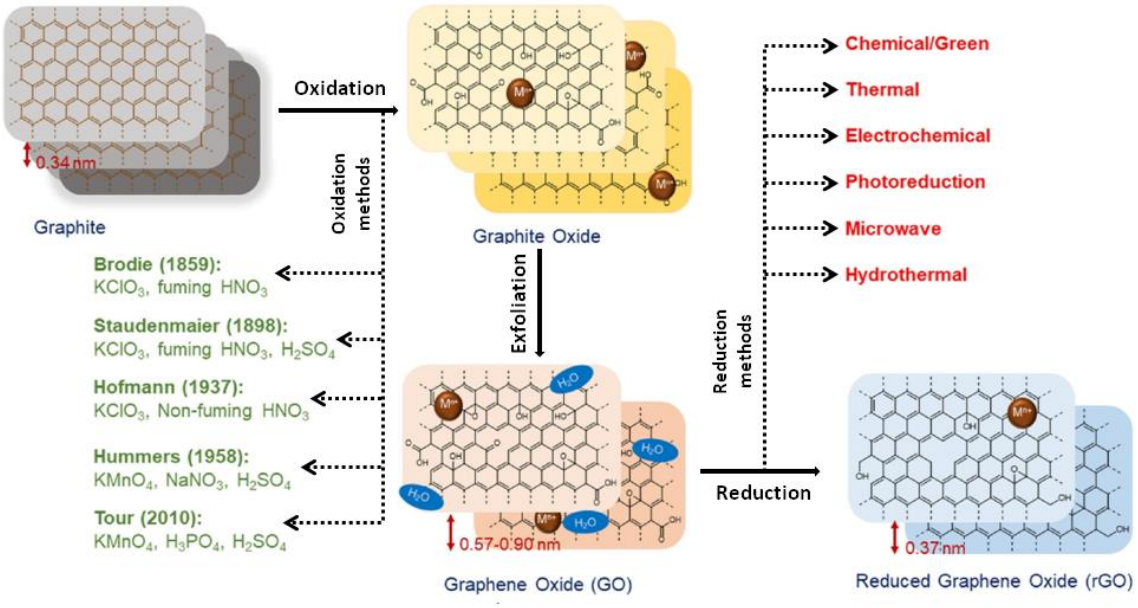

Figure 3-2 Schematic illustration of the oxidation - exfoliation - reduction process of graphite, with mention of the different oxidation and reduction methods.

subsequent exfoliation. Usually, strong acids (e.g. H_2SO_4 or HNO_3) are used as intercalating electrolytes [108–110]. Still, the most promising, scalable and industrially appealing top-down approach is the reduction of graphene oxide. This method, which is summarized in Figure 3-2, involves the chemical oxidation of graphite by means of strong oxidizing agents, creating oxidized groups such as hydroxyl, carboxyl, epoxy and lactone moieties leading to oxidized graphite, referred as graphite oxide (GO). These oxygen-containing groups overcome the Van der Waals inter sheet forces of graphite, increasing the interplanar distance and developing hydrophilicity in GO thanks to the introduced polarity on the material. GO is a non-stoichiometrical compound, and the C:O ratio is mainly controlled by the choice of the oxidizing method, i.e., the oxidizing agents. In fact, many oxidizing routes have been explored, and each method produces a different GO. In order to obtain graphene from GO, an exfoliation process is required: GO can be exfoliated, and this step can be performed by sonication in an appropriate solvent (usually water) followed by a reduction step, for which a plethora of solutions have been proposed,

but the most promising ones are chemical and thermal. In the first case, a reducing agent (as hydrazine, aluminum or boron hydrides, ascorbic acid, …) is employed. The reaction partially restores the sp^2 lattice, producing reduced graphene oxide (rGO). Another method to obtain graphene from GO is by employing a thermal reduction, which can be employed in two different ways. The first way is in the form of a slow ramp, acting as a reduction step to produce rGO after physically exfoliating the GO. The second way is in the form of an abrupt shock, to cause the sudden release of oxidized moieties, detaching from the GO sheets as CO and CO_2, and using the gas development as propulsion to cause both the exfoliation of the GO planes and their reduction. Graphene obtained by these methods tends to be more defective (mostly carbon vacancies due to the stripping of carbon oxides) and is a mix of single layers and few layered graphene. In addition, it contains small residual amounts of impurities from the oxidation step and small percentages of oxygen. Still, the output can be as high as gram to kilogram scale, thus making the GO reduction method one of the only ways to obtain bulk, free-standing graphene-based material, and therefore one of the best scalable and industrially feasible synthesis.

3.3 GRAPHENE IN LIBS

Graphene has found many applications in storage systems, ranging from hydrogen storage [111], super- and ultracapacitors [97], fuel cells [112] and LIBs [43]. For the latter, graphene and graphene related materials have been employed both for minor applications and as the main active material of the electrode. In fact, the synthesis method determines the proprieties of graphene, and the different characteristics of the materials suggest different employments. The uses of graphene in LIBs can be divided in two groups, namely as active components and inactive components. As an active component, graphene was tested as an electrode material, as a Li ions host. Graphene is an ideal

substitute to graphite as an anode material, since it can intercalate lithium on both sides of the carbon sheet, doubling the theoretical capacity from 372 to 744 mAh/g [113–116]. In practice, rGOs have been tested and the experimental capacities tend to greatly exceed the theoretical value, being as high as thousands of mAh/g in the first cycles [117], but unfortunately, this amazing capacity is not retained after the de-intercalation and the electrode is characterized by an important irreversibility, due to the SEI formation, which is extremely high when compared with graphite, due to the SSA of graphene. This requires a capacity excess on the cathode side to sustain this big Li ions consumption, or, in alternative, a preventive chemical or electrochemical passivation. After the SEI formation, graphene still displays a high reversible capacity, but most is delivered between 2.5 and 0.5 V of potential, which is significantly higher than the nominal voltage of graphite (see chapter 4.4.5 for an explanation of electrochemical characterization). In addition, a voltage hysteresis is observed in intercalation/de-intercalation processes, thus affecting the energy efficiency of the cell. These reasons, along with the still high cost of graphene, tend to disqualify graphene as an electrode on its own [118,119]. Graphene has also been tested as a non-active material, specifically as a matrix for composite anodes, in which graphene is harnessed to overcome the limitations of problematic and otherwise weak electrode materials [120]. In addition of electroactive materials, graphene can play two different but synergistic roles: on the one hand, it can act as a support for active materials nanostructures in the preparation of the electrode material, while on the other hand it can create an extensive and conductive matrix to improve the electrical contact of eventual dielectric material, whilst buffering the volume changes of alloying and conversion electrodes [121]. For their part the active particles act as a barrier to the restacking of graphene platelets, lowering the Van der Waals interplanar forces, thus preventing agglomeration of the composite. As a drawback, when the cell operates at low potential, a huge irreversible ionic consumption is observed due to SEI formation, forcing the research in the direction of low graphene to electroactive material ratios [120]. Another non electrochemically active uses of graphene in LIBs involve the sieving properties of this material, thanks to its large SSA. In fact, plastics and graphene composites are synthesized in order to functionalize separators to hinder specific

detrimental effect, such as polysulfide shuttling in Li/S batteries [122–124]. Finally, graphene has also been employed as a current collector, given its elevated electrical conductivity. The carbon material has been used either as passivation layer and as conduction enhancer on aluminum [125] and copper [126] collectors or as free standing collector on which electrode slurries can be cast [127]. Still, these applications are limited and not of broad interest. It is now clear that graphene has been extensively tested in LIBs, but, so far, the most interesting and promising possibility is the fabrication of composites of graphene/active material. In fact, the majority of the research involving graphene in LIBs employs rGO, because it is the most scalable and promising method to obtain large-scale graphene material, but its intrinsic defectivity [119] binds the material to the limitations cited above. From this point, the synergistic role of graphene material with the previously mentioned LIBs chemistries will be discussed, both in terms of literature review and the role of graphene in this thesis. Each chapter will comprehend an overview of the state of the art along with the solutions we proposed to the still unresolved issues.

3.3.1 GRAPHENE IN TITANIUM DIOXIDE BASED LIBS

As previously discussed, despite being abundant, green and characterized by good electrochemical performance, the employment of titanium dioxide as a battery anode is hindered by its intrinsic limits. In fact, bare TiO_2 batteries tend to exhibit limited reversibility and capacities way below the theoretical values, with insufficient efficiencies and a loss of capacity that makes them not suitable for effective batteries. rGO has been proposed as a solution to the low electrical conductivity of TiO_2, and the synergistic effect of these materials can help to overcome the inadequacies of both the single components of the composite. Scientific literature is rich of examples of titania-rGO composites, and even more mature and recent works exploit the combination of nanosizing titania to improve the contact between the electroactive material and the rGO matrix. Some notable examples include the combination of rGO with titania in form of quantum-dots [128],

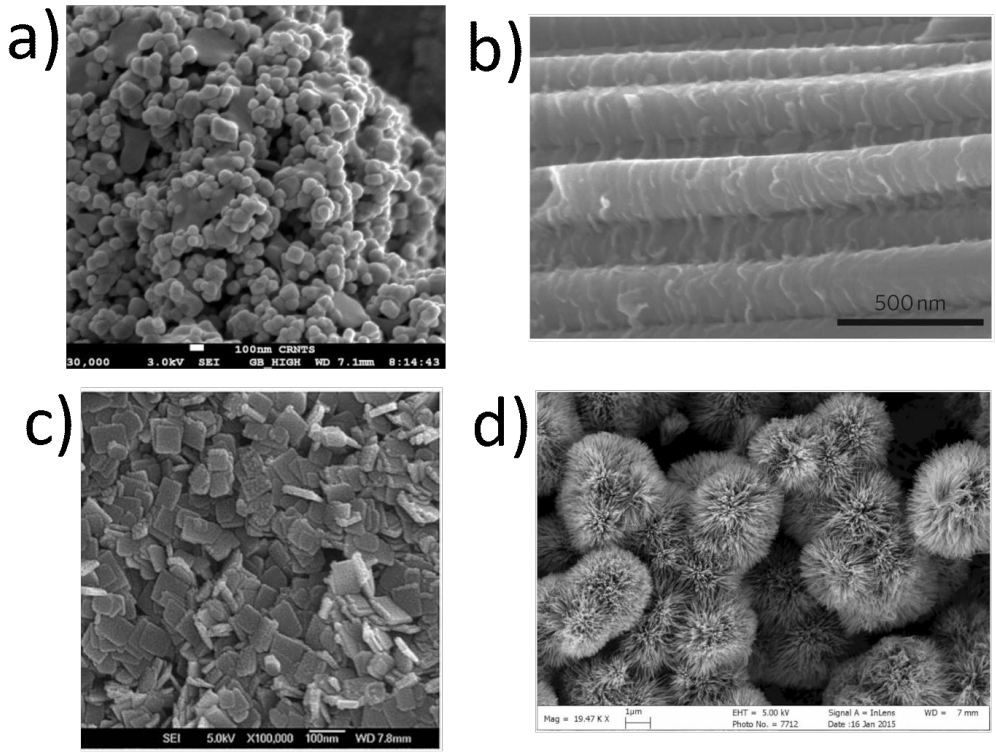

Figure 3-3 SEM images of a) TiO_2 nanosphere b) TiO_2 nanotubes c) TiO_2 nanosheets and d) TiO_2 urchins

nanotubes [129], nanofibers [130], nanosheets [131] and porous nanospheres [132] (as shown in Figure 3-3), to have an elevated surface area to improve the electrical contact and to mitigate the low ionic diffusion of the material. In the current research work, both approaches were followed, thus creating a nanosized TiO_2-graphene composite has been synthesized and tested as a LIB anode. In particular, a highly defective thermally exfoliated GO has been tested [133], with the twofold role of conductive matrix and substrate for the synthesis of the TiO_2 nanocrystals. In fact, the defective surface of graphene is known to act as a nucleation site for heterogeneous growth thus grating finely dispersed and anchored crystals. To exploit this phenomenon, in this work an in-situ TiO_2 decoration of the carbon backbone has been performed, and the TiO_2 NPs were directly grown on the surface of the rGO. The morphological and electrochemical effects observed will be discussed in the chapter 5.1.

3.3.2 GRAPHENE IN SULFUR BASED CELLS

Carbon has always played a vital role in Li/S batteries. In fact, carbon can buffer all the major vulnerabilities of this battery chemistry. Carbon can in fact solve the problems related to the insulating character of sulfur by establishing a good contact with sulfur particles and creating a conductive network, as already explained for the case of TiO_2. In addition, an appropriate carbon-supported electrode can dampen the polysulfides shuttle effect by confining the soluble intermediates inside the pores of the host structure, allowing an extended capacity and cyclability (i.e. life) of the system. Lastly, the carbon support can accommodate the continuous volume expansion/contraction of the active material during the cycles of the cell. In 2009 a pioneering work showed how an opportunely impregnated nanostructured carbon host (CMK-3) could improve the performance of a sulfur cathode [134] and hence the search for the most suitable carbon matrix and the best method to synthesize the composite started. A wide variety of high surface area and porous carbon hosts was tested, ranging from pyrolyzed bio-waste materials [135–137], to porous templated carbons [138,139] up to graphene materials [140–142]. Graphene, despite being expensive, is proposed as the best remedy to all the above discussed issues thanks to its unique properties. Many different graphene-based materials have been tested, with different sulfur-infiltration methods.

In this work, a comparison between the above mentioned thermally exfoliated GO and a chemically reduced GO has been performed, along with a comparison among different decoration methods. In particular, decoration by means of thermal infiltration, chemical precipitation and both solid-state and wet ball milling were carried out, and the different results have been tested and analyzed.

3.3.3 GRAPHENE IN SILICON BASED LIBS

Silicon-based anodes have a long history shared with carbon. Also in this case carbon has a twofold role, either as electrical, or mechanical support for the electroactive material. Carbon is traditionally used to provide an electrically conductive network, to facilitate the electronic flow, which is associated with the charge/discharge process and as a support for Si particles. As a support, carbon needs to encapsulate silicon whilst being able to accommodate its volume fluctuations and act as a sieve in order to hold in place eventual fragmentation product. In fact, fragmentation is an unavoidable process, that leads to loss of capacity, but if the fragmented active material is held by a porous network, the capacity loss is limited to the SEI formation, due to the freshly exposed surface and the material is no longer lost into the electrolyte. Also in this case, many carbonaceous materials and many possible structures (e.g. core-shell, yolk-shell, porous, embedded, …) have been proposed [143–145], but even in this case, graphene outperforms other candidates due to its outstanding electrical, mechanical and surface area characteristics.

In this research work, a big effort was spent in the synthesis of nanostructured silicon particles by a synthetic route that obtains nanoparticles as small as 3 to 4 nm. Electrochemical performance were tested and a comparison between CB and thermally exfoliated GO as conductive matrix was carried out and discussed.

4 EXPERIMENTAL METHODS AND MATERIALS CHARACTERIZATION

The production of composite systems of different electroactive materials and graphene was carried out. In this chapter, the experimental procedures to obtain the carbon materials and the active materials will be discussed, then the synthesis of composites will be explained. Lastly, the production of the electrode and the final device will be illustrated. The final section will describe the characterization techniques of both materials and assembled devices.

4.1 SYNTHESIS OF GRAPHENE-RELATED MATERIALS

Two graphene-related materials have been synthesized and studied in this thesis work. Both are exfoliated and reduced GO. The first one is a thermally exfoliated GO (TEGO), in which an abrupt thermal shock is employed to promote the sudden release of CO and CO_2 gases from the GO oxidized moieties, which act as a propeller for the layer separation under dynamic vacuum conditions. This synthesis leads to a well exfoliated graphene-based material, with an average of 3 graphitic layers with turbostratic disorder, as demonstrated by neutron scattering experiment [146]. TEGO can be produced in large batches (gram scale), but the material is very defective as a consequence of the harsh synthetic conditions, that leads to a lot of in-plane defects and vacancies. The second one is a chemically reduced GO, which is synthesized through a wet method but has the advantages of being a low temperature process carried in water environment. For this process, L-ascorbic acid (LAA) was chosen as the reducing agent, since it is a green and

abundant reagent. The obtained material was called L-ascorbic acid – reduced GO (LAA-rGO).

4.1.1 SYNTHESIS OF TEGO

The preparation of TEGO [133] follows a top-down approach starting with the oxidation of graphite (SGL Carbon, RW-A grade, 66 μm mean size). The oxidation was performed following the Brodie method [147], in which 5 g of graphite powder was ground with 40 g of sodium chlorate and cooled via ice bath at about 2 °C. The powder was mechanically stirred and mixed with 50 ml of fuming nitric acid (99+ %), drop by drop. In this procedure it is important that the temperature of the slurry does not increase out of control, thus requiring a strict control over the ice bath and the effective mixing. In addition, a nitrogen flux is maintained to prevent the oxidation byproducts (i.e., Cl_2O and ClO_2^-) from building up, that could result in a potentially explosive atmosphere. After all the nitric acid was added, a thick slurry was obtained. The mixture was heated at 60 °C with a slow ramp and kept at that temperature for 8 h. After the reaction occurred, the slurry appeared dark greenish. The mixture was diluted in Milli-Q water and filtered via fritted Büchner. The solid was then recovered and dispersed in a diluted (1 M) HCl solution and filtered again. The solid was then suspended in Milli-Q water, filtered, and washed until effluents showed neutral pH. The GO was then dried in a 60 °C oven, mortared to powder. About 7.34 g of dry GO was obtained. A small portion of GO was placed in a quartz vial and swiftly inserted in a tubular furnace at 1150 °C for 30 min under dynamic vacuum (10^{-4} mbar). This harsh step leads to the gasification of oxygen-containing moieties, which acted as propellers for the detachment of the graphite sheets. The reaction was almost instantaneous, with a visible volume increase of the material, resulting in fluffy, fluttering flakes. After the vial was extracted and cooled to room temperature (RT), it was transferred to an Ar-filled glove box (<0.5 ppm of O_2 and H_2O) (MBraun Labmaster 130) to avoid the passivation of the reactive defects by oxygen and ambient humidity.

4.1.1.1 VOLUME REDUCTION OF TEGO

Since the weight ratios between sulfur and carbon reported in literature are quite carbon-rich, highlighting compositions between 50 to 70 wt% as optimal [140], a very large amount of TEGO is needed. TEGO is characterized by a huge apparent volume, and in order to fit the amounts required for lab synthesis (about 100 mg), a volume reduction of the graphenic material is needed. To achieve this, graphene was transferred into Schlenk glassware with Rotaflo stopcock inside an Ar-filled glove box. Anhydrous degassed tetrahydrofuran (THF, Sigma-Aldrich 99.9%) was condensed inside the vial via a Schlenk vacuum line, and the suspension was magnetically stirred overnight. Then, THF was condensed back in another Schlenk vial by immersing it in liquid nitrogen and applying a pressure lower than 10^{-4} mbar, until TEGO was completely dried and reduced in volume. It will be referred as volume reduced TEGO

4.1.2 SYNTHESIS OF LAA-RGO

The synthesis of LAA-rGO follows a parallel path to the TEGO production procedure. For this sample, graphite (SGL Carbon, RW-A grade, 66 μm mean size) was oxidized with the Tour (modified Hummers) method [148]. For this method, 4.5 g of graphite powder were ground and thoroughly mixed with 27 grams of $KMnO_4$. The powders were transferred in a flask and cooled to 2 °C by an ice bath. The powders were mechanically stirred and a 9:1 mixture of concentrated H_2SO_4 (540 ml) and 85% H_3PO_4 (60 ml) was poured dropwise. The wetting process took about 2 hours, then the system was heated to 50 °C for 12 hours. After the slurry reached RT, it was slowly poured on 600 ml of iced Milli-Q water, and then 15 ml of 30% H_2O_2 were added and stirred, and the solution became pale brown / yellowish. The suspension was filtered on a fritted Büchner, and the solid was then resuspended in Milli-Q water and filtered again. Further suspensions and

filtrations were performed with HCl 1 M, water, ethanol (two times) and finally with diethyl ether. The product was dried in a 60 °C vacuum oven, then mortared to powder. The reaction yielded 7.84 g of oxidized graphite, resulting in a major weight gain compared to the previously obtained GO, meaning a more important oxidation. To obtain LAA-rGO, a 1 mg/ml suspension of GO in Milli-Q water was prepared and magnetically stirred overnight. For a typical experiment, 200 mg of GO were dispersed in 200 ml of water and underwent sonication overnight, with a 30-minute sonication and a 30-minute rest pattern to avoid heating effects. Since GO is highly oxidized and hydrophilic, sonication is known to help the exfoliation of multilayers and single layer sheets [149]. The treatment produced a good dispersion with a good stability, and no deposits were noticeable even several days after the treatment. The reduction step was carried out by adding 4 g of LAA to the suspension, and the mixture was stirred until complete dissolution of the reducing agent, then the reaction was heated to 50°C for 24 h at reflux. After this time, the suspension became black and hydrophobic, floating on the surface of the water, meaning that a graphite-like apolarity was restored. LAA-rGO was filtered with a coarse paper filter through a Büchner funnel and washed with abundant Milli-Q water, until effluents became neutral. The solid was filtered and mortared. Typically, a 20% weight loss was observed after the reduction step.

4.2 SYNTHESIS OF ELECTROACTIVE COMPONENTS AND COMPOSITES

In this section, the synthesis of both electroactive materials and the preparation of their composites with graphenic materials is thoroughly described.

4.2.1 EXPERIMENTAL METHODS: TITANIUM DIOXIDE BASED MATERIALS

4.2.1.1 SYNTHESIS OF TITANIUM DIOXIDE NANOPARTICLES

This synthesis was performed to obtain pure titania NPs, that were used as a carbonless reference for the investigation. The aforementioned solvothermal approach was chosen for the employment of relatively safe and inexpensive reagents, the facile execution and the scalability of the process. TiO_2 NPs were synthesized in an autoclave reactor, as summarized in Figure 4-1, by hydrolysis of titanium (IV) isopropoxide (TTIP) (97%, Sigma-Aldrich Co.) [150], an organometallic precursor. Under inert Ar atmosphere, 3 ml of TTIP were inserted in a Pyrex glass vial which was then located inside a Teflon® lined stainless steel autoclave reactor. 5 ml of Milli-Q water was poured inside the reactor, having care to avoid contact between the TTIP and water, to prevent uncontrolled hydrolysis of the precursor due to premature contact between the reactants. The reactor was sealed through its flanges and placed at 180 °C for 17 hours. In this condition, steam

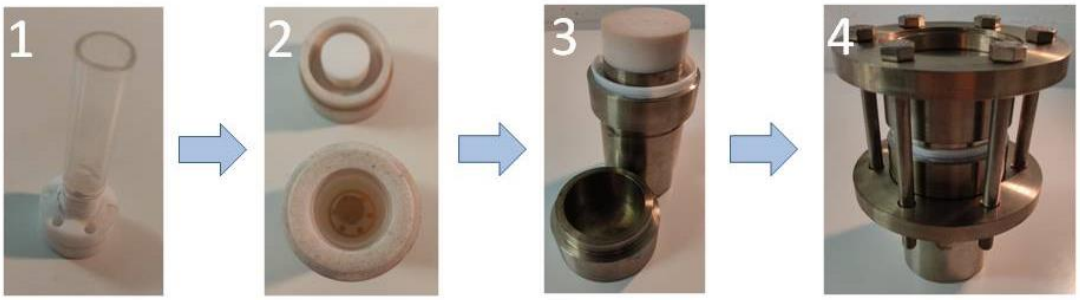

Figure 4-1 Solvothermal synthesis of TiO2 nanoparticles. (1) TTIP was inserted in a Pyrex glass vial. (2) the Pyrex vial was inserted in the Teflon chamber and water was added in the interspace between them. (3) The Teflon vial was inserted into the stainless-steel autoclave. (4) The reactor was sealed through its flanges and underwent thermal treatment

was produced from the water locked inside the reactor, and the reaction reported in reaction (14) took place.

$$Ti(OCH(CH_3)_2)_4 + 4\ H_2O \rightarrow TiO_2 + 4\ (CH_3)_2CHOH \qquad (14)$$

The reactor was cooled at room temperature, opened and the product was dried in a 60 °C oven overnight to evaporate the remaining water and isopropyl alcohol. The titania product was mortared to obtain a fine powder.

4.2.1.2 DECORATION OF TEGO WITH TITANIUM DIOXIDE NANOPARTICLES

This synthesis employs the same procedure used for the preparation of TiO_2 NPs. In addition, TEGO was inserted inside the Pyrex glass vial along with 3 ml of TTIP, soaking the carbon host. For this synthesis, TEGO was always kept under Ar atmosphere and had no contact with air since its exfoliation, to maintain its defects non passivated. As in the previous synthesis, Milli-Q water was added in the cavity between the Pyrex vial and the inner walls of the autoclave. The reactor was sealed and underwent the same thermal

treatment as the synthesis of mere titanium oxide NPs (180°C for 17 hours). The hydrolysis of the organotitanate happens following Equation 13, but the presence of TEGO catalyzes the crystallization in heterogeneous condition, thus decorating the carbon matrix. After the reactor reached RT, the wet product was collected, dried in a vacuum oven at 60 °C and mortar ground to obtain a fine powder. Two different TiO_2 to TEGO weight percentages were produced and compared, being namely 80:20 and 99:1. The first product appeared dark grey, almost black, while the second appeared light greyish.

4.2.1.3 SOLID STATE DECORATION OF TEGO WITH TITANIUM DIOXIDE NANOPARTICLES

In order to compare the TiO_2-decorated TEGO obtained with the hydrothermal synthesis, a sample prepared by simple solid-state mixing of the two components (TiO_2-HT and TEGO) was synthesized. Both TEGO and hydrothermally synthesized TiO_2 were placed in an agate mill jar along with 3 agate balls (8 g each) in a high energy vibratory ball milling (FRITSCH Mini-Mill PULVERISETTE 23). The reagents underwent 3 runs of 10 minutes milling at 30 Hz frequency, with a rest time of 5 minutes between the milling stages to avoid overheating and eventual side reactions. After the milling treatment, the powder was recovered from the bowl. A 99:1 TiO_2:TEGO weight ratio was produced and analyzed.

4.2.2 EXPERIMENTAL METHODS: SULFUR BASED MATERIALS

Three different synthetic routes were identified to synthesize sulfur-graphene composites, each of which with its peculiar advantages.

4.2.2.1 BALL MILLING DECORATION OF TEGO WITH SULFUR

This synthesis involved the combination of sulfur (99.998% purity, Sigma-Aldrich Co.) with TEGO. To achieve the effective combination of the precursors, sulfur and volume reduced TEGO (about 200 mg of dry powders) were placed inside a 15 ml ZrO_2 mill jar along with five milling balls (13.5 g each) of the same material. In order to match the long processing time reported in literature for planetary ball milling [151,152], a 1 hour treatment was chosen. The whole process was divided in 6 runs of 10 minutes milling at 30 Hz frequency (as in TiO_2 milling process), with a rest time of 5 minutes between the milling stages to avoid overheating and eventual side reactions. The powders obtained were recovered after the milling process, and the samples were called S:TEGO BM. Another approach was investigated, since a flourishing literature involves the addition of a liquid medium in the grinding system that acts as a process control agent (namely, wet ball milling). In wet ball milling (W-BM), the liquid medium acts as a lubricant and as a force control agent, limiting the impact forces of the milling process and favoring the shear stresses. Two approaches were chosen: the first one involved ethanol (EtOH) as the wet medium, in which elemental sulfur is slightly soluble (0.066 w/w %), which is already reported as a good dispersing agent in W-BM [153,154]. As a comparison, Milli-Q water was tested. Sulfur is insoluble and TEGO is non dispersible in water, thus the liquid acts as a mere buffer for the process. To our knowledge, no study has been conducted so far using water as dispersing medium. In a typical experiment, 200 mg of dry powders were poured in the milling jar along with 3 ml of liquid medium. After the process, the slurries were slowly dried in a 60 °C oven and the powders obtained were called S:TEGO W-BM.

4.2.2.2 THERMAL INFILTRATION OF TEGO WITH SULFUR

One of the first methods reported in literature to infiltrate sulfur in nanostructured carbon was to thermally infiltrate sulfur inside the scaffold. To obtain these composites, both volume-reduced TEGO and sulfur (99.998%, Sigma-Aldrich Co.), were mixed and finely dispersed in an agate mortar inside an Ar-filled glove box, then the powder was transferred in a glass vial and flame-sealed with a slight depression, leaving about 500 mbar of argon inside the reaction tube. The tube was then transferred in a muffle and heated at 155°C for 12 hours. It was in fact observed that at 155 °C sulfur exhibits its lowest viscosity and can easily permeate inside the host structure [134], while at lower temperatures the molten sulfur leaves evident non-incorporated residues. Both carbon and sulfur are non-polar species and sulfur can impregnate the scaffold for capillary action. The process is facile and effective, thus becoming a standard in these procedures [155,156]. After the thermal treatment, the vial was left cooling at RT and then opened in ambient atmosphere. The sample was called S:TEGO dT, representing its thermally-driven synthesis.

4.2.2.3 CHEMICAL PRECIPITATION AND DECORATION OF GRAPHENE WITH SULFUR

A chemically derived sample was then developed and compared with the physically synthesized samples. For this route, the reaction was carried out in water environment, harnessing the precipitation of sodium thiosulfate ($Na_2S_2O_3$) by means of an acid reactant. The reaction taking place is (15) reported below.

$$Na_2S_2O_3 + 2\,HCl \rightarrow 2\,NaCl + H_2O + S + SO_2 \qquad (15)$$

To achieve a good decoration of the carbon host, a hydrophilic carbon needs to be employed, to achieve the heterogeneous precipitation of sulfur on the surface of the host material. Since GO has been characterized as highly oxidized and is well dispersible in water, it was picked as a scaffold for this sample. In an ordinary experiment, GO was dispersed in Milli-Q water in a concentration of 1 mg/ml, obtaining a brown suspension. The mixture was then stirred for 2 hours and underwent sonication overnight, with a 30-minute sonication and a 30-minute rest pattern, as in the preparation of LAA-rGO. Then, sodium thiosulfate was added to the reaction vessel and stirred until complete dissolution of the salt. Then, an excess of hydrogen chloride (about 100 ml with a 0.2 M concentration) was slowly added to the solution, via a dropping funnel in about 1 hour. The solution was continuously stirred, and after the addition of some milliliters of HCl, started to appear cloudy and milky, meaning the precipitation of sulfur was taking place. After 1 hour of vigorous stirring, LAA was added to the solution and the system was heated at 50 °C for 24 hours. After this time, the solution appeared completely transparent with the rGO floating on the surface of the aqueous solution, meaning that no unbound sulfur is left in the solution and that GO turned hydrophobic, thus being effectively reduced. Both sulfur decoration and reduction were successfully achieved in a one-pot process. The suspended solid was filtered through a fritted funnel and washed until effluent turned neutral. The filtered product was then dried in an oven at 60 °C, mortar ground and labeled as S:LAA-rGO.

4.2.3 EXPERIMENTAL METHODS: SILICON BASED MATERIALS

4.2.3.1 DISPROPORTIONATION OF SILICON MONOXIDE

In order to disproportionate SiO, a few grams of the reagent were placed inside a tubular furnace inside a quartz vial, as shown in Figure 4-2. The system was then evacuated by a turbomolecular pump reaching up to a 10^{-5} mbar. Then, the pump was isolated, and the system was purged by blowing a mixture of 5% H_2 and 95% Ar v/v % for about 1 hour. Then the system was heated without interrupting the hydrogen flow, which is needed to create a reductive atmosphere to prevent undesired reactions between elemental silicon

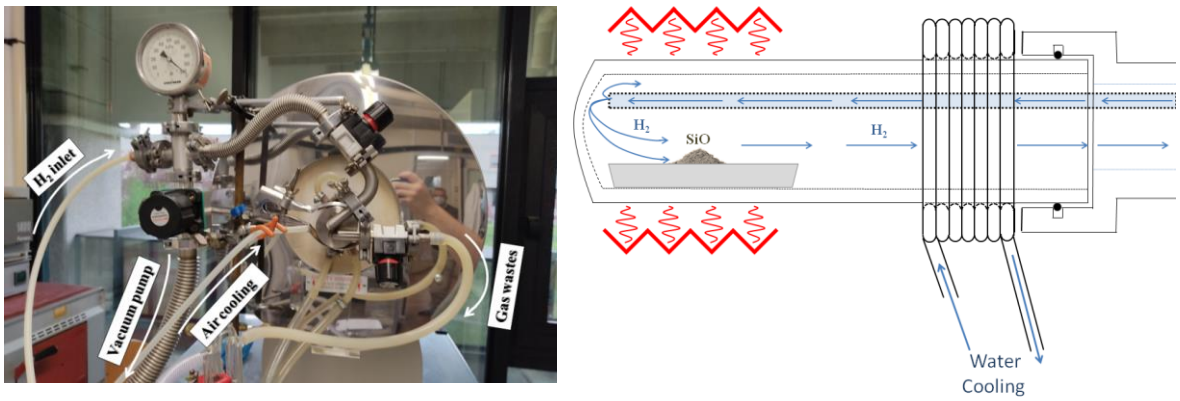

Figure 4-2 On the left: photo of the piping system used for the atmosphere-controlled disproportionation of SiO. On the right: scheme of the reaction chamber, a quartz tube conveys the hydrogen:argon mixture directly on the sample. The system operates in a slight H_2 overpressure, and the excess H_2 in sent to the waste line.

and eventual traces of O_2 or H_2O. Different temperatures between 950 and 1100 °C and different treatment times were tested and compared, in order to achieve the smallest crystal size. The occurred reaction is reported below:

$$2\,SiO \rightarrow Si^{0} + SiO_2 \qquad (16)$$

After the treatment, the system was slowly cooled at RT, then the quartz vial was evacuated and opened inside an Ar-filled glove box, to prevent possible passivation of the silicon nanoparticles.

4.2.3.2 PURIFICATION OF DISPROPORTIONATED SILICON MONOXIDE

The disproportionation of SiO produces Si NPs dispersed in a SiO_2 matrix, as shown in Equation 16. For this reason, a selective etching of the oxide fraction must be carried out to obtain pure silicon NPs. To obtain a selective etching for both SiO_2 and SiO while leaving Si unaltered is, HF is traditionally used both in silicon semiconductor wafers [157,158], to deep clean the surface, and to remove silicon oxide particles [159,160]. A well-established method to achieve a quantitative removal of the oxide fraction involves a solution of HF (48 vol %) and ethanol in a 2:1 ratio, but in order to perform a safer procedure, the HF solution was substituted with a 6 mol % NH_4HF_2 solution in Milli-Q water. This leads to a slower kinetic in the etching process, and longer reaction times are needed [161]. In order to prevent oxidation of Si NPs, the reaction vessel was prepared in an Ar-filled glove box and all the treatments were carried out under Ar atmosphere. In addition, all solutions were degassed to remove oxygen from the solvents via the freeze-thaw-pump method (reaction setup schematized in Figure 4-3a) [162]. In a typical experiment, about 1 g of disproportionated SiO (a mixture of Si, SiO and SiO_2) and 20 g of NH_4HF_2 were placed in a plastic reaction vessel equipped with a polycarbonate cap inside a glove box (reactor shown in Figure 4-3 b), then all the vents were sealed, and the system was placed under a fume hood. Then, Ar was fluxed in the system to prevent any air contamination, and the water:ethanol solution was added to the reaction vessel through a Teflon straw, thanks to an Ar overpressure. Then, the solution was magnetically stirred for 6 hours to promote the dissolution of silicon oxides. The reactions taking place inside the vessel can be schematized in the following equations. First, ammonium bifluoride dissociates in aqueous conditions:

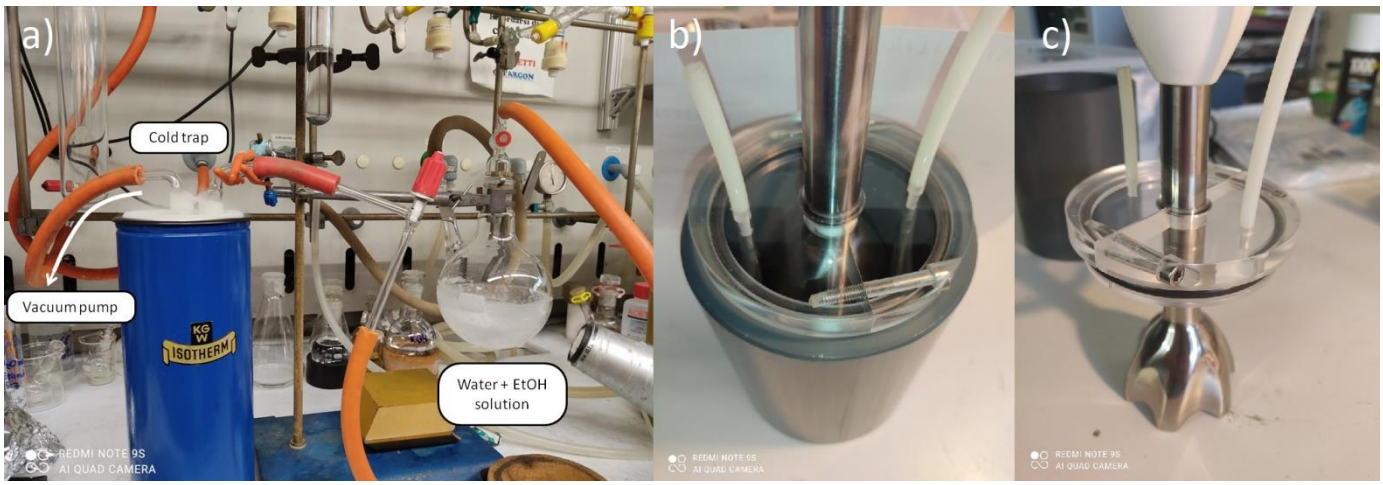

Figure 4-3 a) Freeze-pump-thaw setup. The solvent is frozen, and vacuum is pumped during the melting of the solid, where the gas solubility is at its lowest. The process is repeated at least three times until no bubbling is noticeable. b) Reaction vessel for the etching reaction. The polycarbonate seal cap helps the monitoring of the reaction, the straws are employed to grant the Ar flow. c) Close detail of the immersion blender attached to the cap used to create the water-hexane emulsion, and the O-rings used to make a good seal of the vessel.

$$NH_4HF_2 \leftrightarrow NH_4^+ + HF_2^- \quad (17)$$

The dissociated HF_2^- species can undergo hydrolysis and generate free HF in the solution, following:

$$HF_2^- + H_2O \rightarrow 2\,HF + OH^- \quad (18)$$

In aqueous environment, silicon dioxide is selectively dissolved, and the overall reaction is reported:

$$SiO_2 + 4\,NH_4HF_2 \rightarrow 4\,NH_4F + 2\,H_2O + SiF_4 \quad (19)$$

Silicon can be dissolved in the form of SiF_4, which is a gas, that is easily removed by the argon flow or undergoes further reaction with HF and remains in aqueous solution in the form of H_2SiF_6, which is a stable complex composed by $2H_3O^+ \cdot [SiF_6]^{2-}$. Since the reaction takes place in acidic environment, etched silicon NPs are hydride-terminated and

are non-polar. In order to extract the NPs, a liquid phase extraction was chosen. Hexane was chosen, being non polar organic solvent, immiscible in water and known as a good solvent for Si NPs [161,163]. 100 ml of degassed n-hexane were added to the reactor, and an immersion blender was inserted in the liquid mixture (Figure 4-3 c) and the high energy shear force was employed to create an emulsion between the water and the organic phase, to enhance the transfer of the Si NPs between the phases. After 10 minutes, the blender was stopped, and after the emulsion separated again, a plastic straw was used to remove the organic phase. The Si in hexane was transferred in a Schlenk vial under a protective Ar atmosphere, ready to decorate a carbon scaffold by impregnation with this suspension of Si NPs.

4.3 PRODUCTION OF HALF-CELLS

Figure 4-4 CR2032 coin cell. This schematic representation shows the standard architecture of any electrochemical device produced and investigated in this thesis work. Titania and sulfur battery employ aluminum foils as collectors. The system is soaked in suitable electrolyte.

All the electroactive products and composites were tested in half cells, namely a cell composed of active material operating vs a pure lithium metal electrode, which operates as both counter and reference electrode. The manufacturing of electrodes was carried out by mortaring the components of the electrode materials, namely active/composite material, a plastic binder (polyvinylidene fluoride, PVDF, Solvay, Solef®5310 for TiO_2-containing LIBs, polyacrylic acid, PAA, Sigma-Aldrich, for sulfur and silicon batteries) and eventually CB (Timcal, Super 65) if carbon fraction was too low or absent, to ensure a good electronical conductivity. The powder was then soaked adding NMP (anhydrous 99.5%, Sigma-Aldrich) drop by drop, until a thick slurry is obtained. The slurry was

mixed overnight, and then spread onto a metal collector foil (aluminum for sulfur and titania, copper for silicon) using a notch-bar, with thicknesses ranging from 0.3 to 1 mm. The solvent was then slowly evaporated in a 60 °C oven for a few hours, and in a 70 °C vacuum oven overnight. The film was then pressed with a hydraulic press (7 MPa) for a few minutes and punched in 12 to 16 mm diameter discs, which were pressed again under the hydraulic press, dried at 70 °C in a vacuum oven overnight and transferred in an Ar-filled glovebox. Typically, electrodes were loaded with 0.5 – 3 mg of active material per cm^2, and were tested after being assembled in CR 2032 coin cells (Tmax - Xiamen Battery Systems). The preparation of a coin cell device follows the architecture reported in Figure 4-4 and all the system was soaked with about 1 ml liquid electrolyte, namely a 1.0 M $LiPF_6$ EC/DMC 50/50 (v/v) [164] (Sigma-Aldrich, battery grade, <15 ppm H_2O, <50 ppm HF contaminant) for titania and silicon batteries, while sulfur batteries employed 1 ml of 1 M bis(trifluoromethane)sulfonimide lithium salt (LiTFSI, 99.95 % Sigma-Aldrich) solution in 1,3-dioxolane (DOL) : 1,2 dimethoxyethane (DME) 50/50 (v/v) [83,165] with 1 % w/w $LiNO_3$ as a passivating agent for metallic lithium anode [166–171]. After the negative case was placed on top, the device was pressed in a mechanical press inside the glovebox, to tightly seal the case. In this configuration, lithium metal acts as a counter electrode and always acts as the anode of the system, having the lowest reduction potential (-3.04 V vs Standard hydrogen electrode, SHE). So, despite titania and silicon act as anode in full cell configuration and sulfur is employed as a cathode vs Li metal or other anodes (graphite [172], silicon [173], …), in all half cell devices all active materials have a higher reduction potential than lithium and operate as cathodes.

4.4 MATERIAL CHARACTERIZATION

The samples prepared were characterized with different analytical techniques. First, the structure of the obtained materials was investigated in order to understand the crystal structure, weight fractions, structure and morphology of the samples. Namely, since each of those is a crystalline material, powder X-ray diffraction (PXRD) was employed to investigate the crystal structure of all active materials, while scanning electron microscopy (SEM) and transmission electron microscopy (TEM) were employed to investigate the micro and nanostructure and morphology. In the case of TiO_2 samples, Raman spectroscopy was also employed in order to evaluate the chemical structure and the polymorphism of nearly amorphous samples. An operando experiment was carried out using synchrotron radiation to evaluate different titania electrodes inside half cells during discharge/charge cycles. Electrochemical characterization was carried out by chronopotentiometry (CP) technique, namely galvanostatic charge/discharge (GCD), in order to evaluate the capacity and stress behavior of produced devices.

4.4.1 POWDER X-RAY DIFFRACTION (PXRD)

PXRD is a non-destructive technique employed for the structural analysis of crystalline powders. XRD is a powerful technique used to investigate the periodic arrangement of atoms, ions and molecules inside an ordered lattice. Even though the knowledge of the atomic arrangement is not crucial in electrodes such as sulfur and silicon, that undergo dissolution and amorphization upon the first discharge, the understanding of the crystal structure is crucial in materials like TiO_2, in which different polymorphs are characterized by different properties. In fact, in this work, PXRD has been heavily employed as a characterization tool to investigate the properties of synthesized material, mostly for the determination of crystal structures of electroactive materials. PXRD is based on the

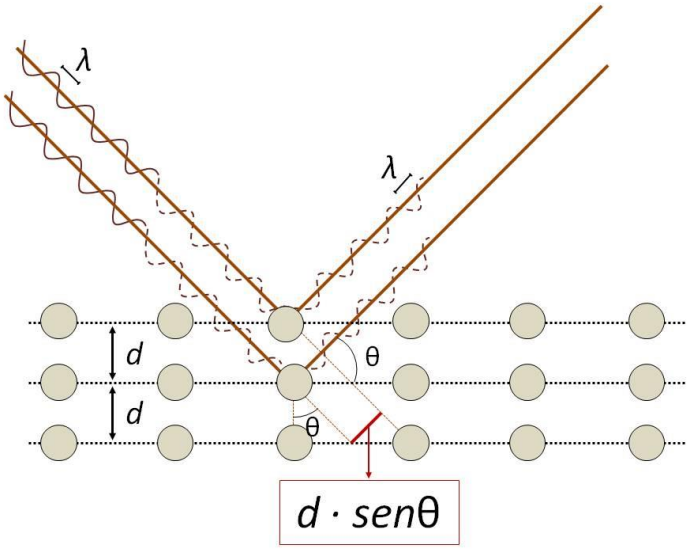

Figure 4-5 Schematization of Bragg's law. Incident radiation is reflected by a family of planes of the crystal lattice. Constructive interference takes place when Bragg's law is satisfied.

interaction of a photon beam (X-ray) and a crystalline sample. The technique is based on the elastic scattering phenomenon, happening when suitable electromagnetic radiation interact with a crystalline solid material (powder); in fact, when crossing a medium, photons are deviated from their original trajectory due to interactions with matter. In the case of XRD, it relays on the interaction of X-rays and atoms. In an XRD experiment, atoms act as scattering centers for the incident radiation, and the scattered photons are characterized by interference patterns, that are consequence of repetitive interatomic distances and the periodicity of atom positions, typical of crystalline materials. PXRD exploits coherent and elastic scattering, which gives constructive interference and produces a well-defined pattern of scattered X-rays intensities that follow Bragg's law, that is reported below:

$$n\,\lambda = 2d\,\sin\theta \qquad (20)$$

This formula gives an empiric interpretation of the constructive interference phenomenon of photons scattered by a crystal lattice. It considers crystalline planes as evenly spaced sheets constituting the crystal structure (characterized by Miller's indices h, k and l), with a recurring distance *d* from adjacent planes. In this model, planes act like mirrors, hence adjacent places will scatter light undergoing constructive interference when the angle θ between planes and light result in an integer (*n*) multiple of the X-rays wavelength λ (~1.54148 Å in case of a copper tube source), as summarized in Figure 4-5. In a PXRD measurement, constructive interferences are translated in peaks in a diffractogram, and information about the material are provided by the position, the intensity and the shape of the peaks. The relative positions of peaks are related to the symmetry of the crystal, namely the periodic cell unit in which the crystal is arranged. The intensity of each peak, on the other hand, depends on the atom positions in the unit cell. Lastly, the shape is related to both instrumental parameters of the measurement and intrinsic properties of the material, mostly the particle size of the investigated material. In this thesis, two different instruments have been employed to perform PXRD, operating in different geometries. The first instrument, operating in Bragg-Brentano geometry was a Bruker D2 Phaser, equipped with a copper tube source (CuK_{α}) and a Linxeye detector. Measures were performed on samples placed on a silicon zero-background sample holder, which was spun to achieve a homogeneous measure. In case of air sensitive samples, a polycarbonate airtight dome was mounted on the sample holder. The sample was placed on the sample holder and the airtight dome was closed inside an Ar glove box, and the atmosphere was preserved during the measure. The other measurements were performed in a Debye Scherrer geometry with a D8 Advance Bruker instrument. The system was also equipped with a copper anode, and a Rayonix MX225 was used as a 2D detector. All samples were sealed into glass capillaries of 0.5 – 0.7 mm diameter and spun during the diffraction analysis. Air-sensitive samples were prepared inside an Ar-filled glove box, while the other ones were prepared at room atmosphere conditions. After the diffractogram was collected, specific softwares were employed to perform data analysis (FullProf Suite [174], Fit2D [175]), the identification of the crystal phases (Crystalimpact Match [176]) and the Rietveld or Le Bail refinements (GSASII suite [177]), used to fit the experimental

data against a structural model through the least square methods, to investigate sample parameters such as the crystallite size (via the Scherrer method).

4.4.2 RAMAN SPECTROSCOPY

In this work, micro-Raman spectroscopy was employed to identify non-crystalline phases which resulted challenging to understand using PXRD. It was also employed to confirm results obtained with different techniques, such as phase identification and nanocrystal dimension estimation. Raman, like PXRD, harnesses the interaction between photon and matter, but in this case a high intensity monochromatic laser is employed. The interactions happen between the laser and the sample. Most photons are elastically scattered, meaning that the direction of the wave is altered but the wavelength and frequency are maintained; this phenomenon is called Rayleigh scattering. However, a small amount (1 in a million) of photons undergoes an inelastic scattering; inelastically scattered photons have a different energy than that of incident light and are called Raman-scattered photons; for that, part of the initial energy is exchanged with the vibrational modes of the sample. The wavelength of the Raman-scattered photon depends on the initial properties of the light source and on the properties of the analysed material. The energy difference between the scattered and the incoming radiation corresponds to the vibrational energy of a molecular vibration. In the Raman spectrum, the vibrational frequencies are obtained and usually are expressed as wavenumbers (or Raman shift) in cm^{-1}. The Raman spectrum features the characteristic peaks of the vibrational modes of molecules, crystals or amorphous solids. Both qualitative and semi-quantitative analysis can be performed with Raman spectroscopy; in this work it was used to estimate both the phase and the mean size of TiO2 nanocrystals. Measurements were performed with a Horiba Jobin Yvon LabRam (HORIBA Scientific, Kyoto, Japan) confocal micro-spectrometer (300 mm focal length), equipped with an Olympus BX40 microscope (Olympus, Tokyo, Japan), using a 50x ULWD objective, an 1800 groves/mm grating, a XY motorized stage and a Peltier cooled

silicon CCD. The 473.1 nm line of a doubled Nd:YAG laser was used as excitation, with a spectral resolution of ~4.0 cm^{-1}. The spectra were acquired in the spectral range from 100 to 2000 cm^{-1}. The system was calibrated using the 520.6 cm^{-1} Raman peak of silicon. To avoid heating effects on the samples, the laser excitation power was lowered by means of density filters. Typical acquisitions were 60 s repeated at least 10 times. Data analysis was performed with the LabSpec 5 software [178].

4.4.3 TRANSMISSION ELECTRON MICROSCOPY (TEM)

TEM microscopy is a powerful and versatile analytical method used in research. It employs a high energy electron beam flowing in a vacuum chamber and directed onto a very thin flake of specimen. The advantage of using electrons instead of visible light is that the smaller wavelength of electrons offers a better resolution of the images, orders of magnitude better than a traditional light microscope. The electrons transmitted through the sample are then projected on a fluorescent screen and the image of the crossed portion of matter is reconstructed. The imaging is built upon the scattered electrons passing through the sample. Electrons are scattered depending on the crystal orientation and composition of the specimen. Un-scattered electrons give rise to the "shadow image" of the specimen, in which the changes in density of the sample impart differences in the displayed darkness. TEM has an anatomy similar to those of optical microscopes, including apertures and condenser, objective and projector lenses, but in this case the optics are in fact electromagnetic components, mostly solenoid coils that impart their magnetic field onto the electron flow. The schematical representation of a TEM system is reported in Figure 4-6 [179]. In this work, TiO_2 samples were investigated with TEM in order to investigate the effective decoration of carbon scaffold with titania NPs, to better understand the morphology and distribution of the system. TEM analysis was performed via a field emission JEM-2200FS high-resolution microscope (JEOL Ltd., Japan). The electron source was a Schottky gun with an accelerating voltage of 200 kV,

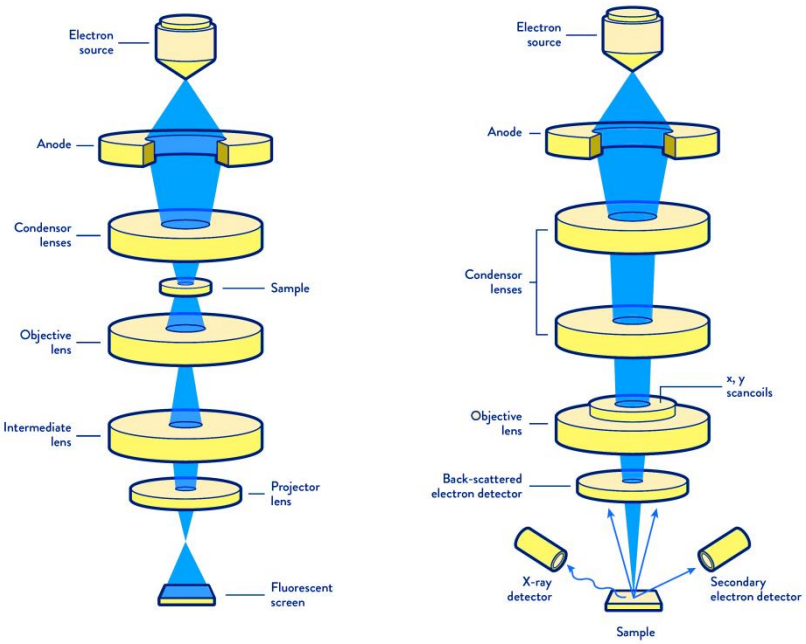

Figure 4-6 Schematic representation of the geometry and optics of TEM (on the left) and SEM (on the right). The light blue beam represents the electrons sourced by the electron gun and interacting with the sample.

with a point resolution of 0.19 nm. Signal was cleared through an in column "omega-type" energy filter before reaching the detectors (STEM detectors, high resolution CCD camera and an EDS detector). To perform the TEM investigation, the as-synthesised powders were dispersed in isopropanol (about 1 mg per ml of solvent). Few drops of the suspension were dropped onto a holey carbon film supported on a copper grid, and the sample was placed in the microscope.

4.4.4 Scanning Electron Microscopy (SEM)

Similarly to TEM, SEM is used to plot and recreate the image of a surface using an electron beam. The electrons interact with the atoms of the sample and produce many signals from which a variety of information can be extrapolated. In order to produce an

image, secondary electrons are collected from the detector, and their energies and intensities are used to raster the 2D image with a depth of image that recreates the morphology and topography of the analysed sample, as schematized in Figure 4-6. This technique is characterized by a lower resolution compared to TEM and can investigate lower magnification, but it provides a characteristic depth of field of images which cannot be obtained by TEM. In this thesis work, SEM measurements were performed with a Zeiss EVO MA10-HR microscope. To perform a standard analysis, powders were loosely on C tape, which was then stuck onto an aluminum stub. To perform topography of low-conductivity samples, few nanometers of gold were sputtered on the surface of the specimen, to mitigate electrostatic events happening onto insulating samples that may cause drifting of the image.

4.4.5 GALVANOSTATIC CHARGE/DISCHARGE (GCD)

GCD is a technique that does not provide information about the mere material, but on the final device. In fact, much information about an electrochemical cell can be obtained from this analysis. In a GCD experiment, a cell is connected to the instrument and a constant current is provided, leading to the repeated charge and discharge of the device, while the voltage is measured and acquired at close intervals, in the range of few seconds. One of the most relevant pieces of information that can be deduced with this measure, is the capacity of the active material, that is the total electric charge stored in the cell, namely the current integrated in the time span of the measure, that is the product between current and time of each semicycle (either a charge or discharge cycle). The current applied is decided upon the type and weight of the active material, tuning a parameter called C-rate. C-rate is defined as the current needed for a full theoretical charge or discharge of the cell in a fixed amount of time. It can be intended as the frequency (in hours) of a full semicycle, and is expressed as C/X, where X are the hours calculated for a full semicycle. For instance, a C/5 (or 0.2 C) rate corresponds to the current needed to perform a full

semicycle in 5 hours. C rate is calculated upon the theoretical specific capacity (C_{th}) of a material, that is calculated following Equation 20:

$$C_{th} = \frac{\Delta x \cdot F}{M} \cdot \frac{1000}{3600} \quad (21)$$

where Δx is the maximum moles of lithium that can be inserted in or extracted from the material of molecular weight M, and F represents the Faraday constant. The specific capacity is finally expressed in mAh/g, thanks to a conversion factor. Thanks to this analysis, which requires many cycles (100 or above) of charge/discharge processes of the device, the long-term reliability (ageing) of the devices is examined, and parameters like capacity loss can be understood. In addition, during a GCD analysis, various C-rates are tested, in order to investigate the cell behaviour under ideal and stressful conditions. In a typical measure in fact, sets of ten cycles were performed at various C rates (C/10, C/5, C/2, C, 2C) to investigate the cell behaviour at different current rates. If the charge/discharge process is performed at very slow C-rates, galvanostatic curves can depict a good approximation of the open circuit voltage (OCV) of the cell. If the cycling takes place at high C-rates, the electrochemical cell operates in non-equilibrium condition, and spurious effects can be observed, thus voltage profile deviates significantly from the ideality. In these conditions, polarization effects and differences between charge and discharge profiles are observed, and these phenomena are referred with the name of overpotentials. Such deviations η are described as:

$$\Delta V_{real} = \Delta V - \sum \eta \quad (22)$$

and can have many different causes and explanations, including:

• Charge transfer: polarization effect caused by the low transfer kinetics between electrolyte and electrode interface.

• Diffusion: lithium ions may have slow diffusion inside the electrode, or in the interfaces of the cell. This usually happens during high-rate charge/discharge, and determines a gradient of lithiation, decreasing along the depth of the electrode.

• Reaction: this voice includes chemical reactions taking place in the bulk of the electrode or the electrolyte. Typically, a not so relevant contribution.

• Crystallization: this phenomenon is a consequence of crystallization or plating of lithium ions on the surface/interface of the electrode [180].

The overpotential translates in a potential offset with respect with the ideal voltage profile. Usually, overpotentials tend to create a lower potential during discharge and a higher potential during charge, along with polarization bumps. Possible consequences include cells that appear completely charged or discharged even if not the whole electrode is completely lithiated (or delithiated), or metallic plating effects that could create dendrites that could short circuit the cell among others. Overpotentials are related to Ohm's law that relates current intensity and resistance with potential:

$$\eta = IR \tag{23}$$

Hence, overpotential tend to occur with high current densities and in case of insulating materials, like the pure active materials studied in this work. Graphene will show a beneficial effect also in the reduction of these occurrences. In this work, GCD measurements were performed via a Landt CT2001A apparatus.

4.4.6 SYNCHROTRON LIGHT DIFFRACTION

Synchrotron radiation is an extremely concentrated and bright X-ray. The X-rays are generated when electrons circulating near the speed of light are forced to alter their linear direction. In order to produce this event, electrons are first generated by a thermionic gun

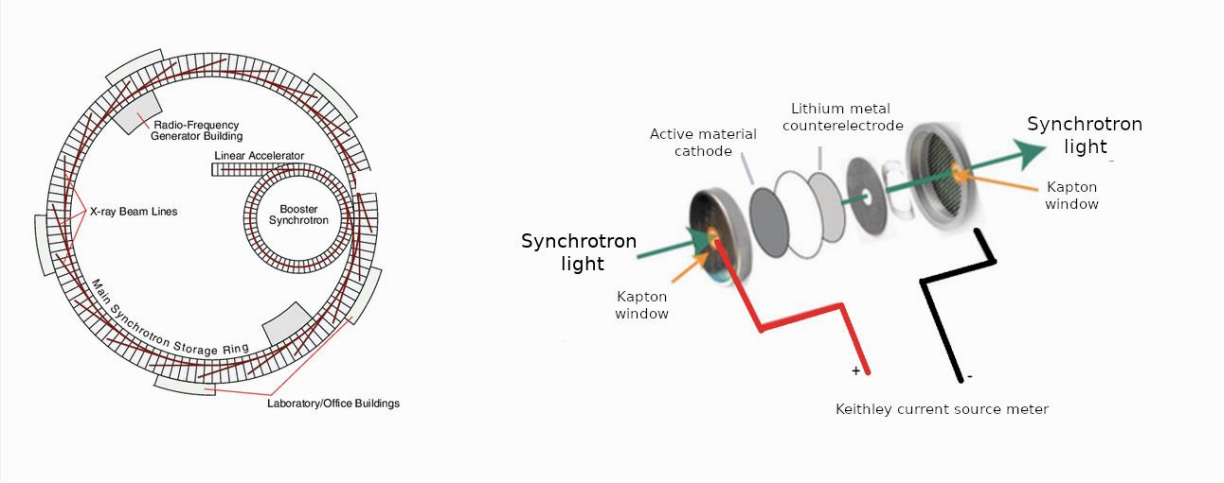

Figure 4-7 On the left, schematic representation of a synchrotron accelerator. On the right, the cell architecture employed for the operando experiment on the MCX beamline at the Elettra synchrotron light source in Trieste.

and accelerated in a linear accelerator, that injects the electrons in a circular booster synchrotron. In this chamber, electrons loop thousands of times gaining energy for every round and are accelerated to the final energy, in the range of a few GeV. Once their energy is climaxed, the electrons are injected in a storage ring, where they are deflected by bending magnets to maintain the circular trajectory. When the electron flow is deviated, a loss of energy occurs in the form of X-ray emission, thus synchrotron light is released tangentially to their primitive direction and conveyed to the appropriate beamlines. At the end of the beamlines, samples and detectors are positioned in order to perform experiments. Other components are focusing magnets, that concentrate the electromagnetic beam in a narrow spot and Radio-Frequency generators (ondulators), magnetic devices with alternating polarity that produce high energy X-rays and feed energy to the circulating electrons, to compensate the emission losses. A basic scheme of a synchrotron is depicted in Figure 4-7 [181]. For this work, an operando analysis on TiO_2-containing LIBs was performed by means of synchrotron powder X-ray diffraction (SPXRD), in order to monitor and compare the crystal evolution of the active material in samples with different synthetic stories. To inspect in-operando batteries, CR2032 coin-cell cases were properly modified to allow the passage of synchrotron light, as shown in

Figure 4-7. In particular, the cell case and the current collector were drilled to keep a transparent path for the beam, operating in transmission configuration. Kapton® windows were glued to the cell case to keep the cell airtight and to prevent leakages. In this configuration, the synchrotron radiation passes through the electrode material along with the aluminum foil used as cathodic collector, the Celgard® separator, lithium counter-electrode and the Kapton® window. The experiments were performed on the MCX beamline at the Elettra synchrotron light source in Trieste (Italy) [182]. Powder patterns were collected at 12 keV (λ = 1.0332 Å) using a MAR-CCD165 area detector (80 μm pixels size), after suitable calibration using a LaB_6 standard (SRM660a from NIST [183]) with 10 s per acquisition separated by 5 min breaks. Data reduction and integration of the 2D patterns were carried out using the GSAS-II suite [177]. For each sample, the 2D patterns for the entire run of cycling were merged together to detect spurious features repeating over time, which were then masked effectively prior integration. A minority of extra features randomly occurring during the operando experiments were easily spotted and removed. Integrated patterns were analysed by means of sequential Rietveld refinement starting using the known phases of pure and lithiated TiO_2. The low profile-resolution posed by this particular geometry is well compensated by the high resolution in time obtained using a fast 2D detector. To gather additional information on the most interesting samples, pristine powders, composing the active materials of the batteries, were measured also on MCX at 12 keV in Debye-Scherrer geometry on the 4-circle Huber goniometer equipped with a high count-rate scintillator detector and receiving slits open at 0.2 mm (vertical) and 0.3 mm (horizontal). Borosilicate capillaries (0.3 mm diameter) were filled with powders and measured at room temperature while spinning at 300 rpm. The two known phases of anatase and brookite were Rietveld refined against the data using GSAS-II [177]. A silicon standard (640c by NIST [184]) was used for establishing the instrumental profile for both 1D and 2D detectors in both geometries.

5 RESULTS AND DISCUSSION

5.1 TITANIUM DIOXIDE-BASED CELLS

As previously discussed, both the nanosizing of TiO_2 and the combination with TEGO, which acted as a conductive, high surface area additive, has led to an important improvement of titanium dioxide batteries. In this chapter, the characterization of the pure TiO2 material and their composites with graphene is discussed. The materials were investigated with PXRD, Raman and TEM to study the structure and morphology, while GCD was employed to evaluate the electrochemical performance of electrodes. Finally, SPXRD was carried out on in-operando devices to analyse the crystal evolution of different samples.

5.1.1 CHARACTERIZATION OF TEGO

TEGO synthesis has been extensively discussed in the previous chapter. Here, the properties of the material will be discussed. In Figure 5-1 the evolution of intermediate and final products is evidenced by means of PXRD. Graphite, the starting material, has its main crystallographic feature in the (002) reflection, which is related to the intermittent (Bernal, or ABA [185]) stacking periodicity of the graphitic planes. These planes have an interlayer distance of 0.335 nm and this corresponds to the peak at $2\theta = 26.6°$ (Figure 5-1). After the oxidation treatment with the Brodie method, an increase in the stacking distance was observed thanks to the shift of the (002) peak, which is found at $2\theta = 14.5°$ in the GO sample. This expansion was quantified by the refinement of the model and results in a 0.611 nm interlayer distance in the oxidized sample; this is due to the

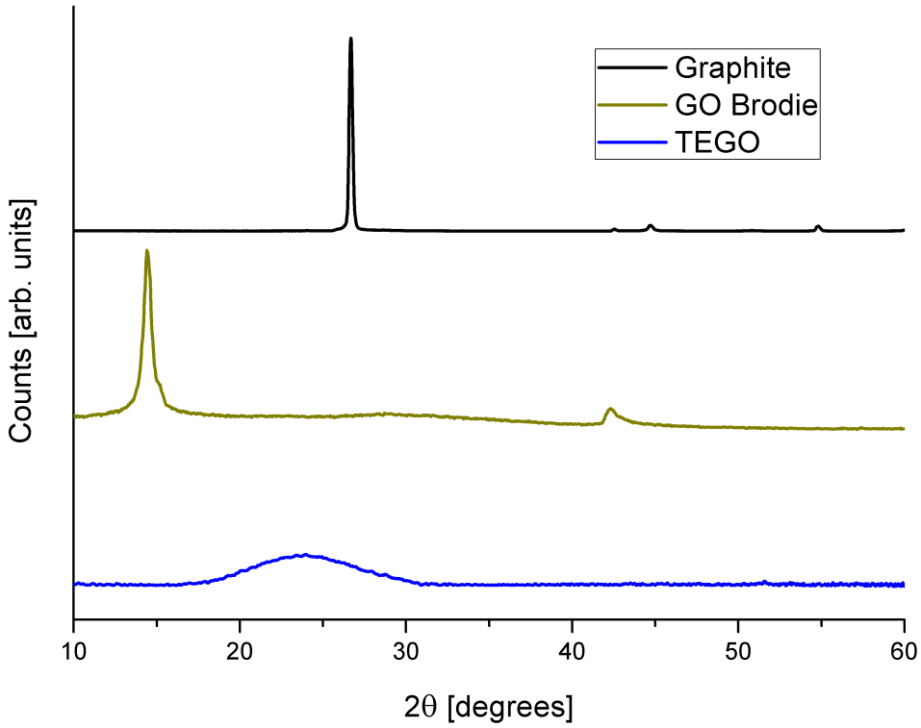

Figure 5-1 PXRD performed on graphite, TEGO and the GO intermediate, obtained with the Brodie method.

formation of oxidized moieties, which expand the graphite planes and weaken the Van der Waals forces that are responsible for the tight stacking of pristine graphite layers. This is mainly caused by hydroxyl, epoxy, ketonic, quinonic and lactonic moieties, which are found as in-plane modifications. On the other hand, acidic groups are mainly found on the edges of GO and are responsible for the water solubility of the materials, meaning that an abundance of –COOH groups lead to a water-dispersible GO. Brodie has a low acidic fraction (about 2.7 % [147]), so it is not suitable for water based processes, but it can be efficiently exfoliated by quick thermal treatment, obtaining TEGO, which has almost no crystalline features, since the (002) periodicity is lost upon exfoliation. A broad bump is noticeable at $2\theta \sim 25°$ in the diffractogram, meaning that the mean stacking distance is similar to graphite and no more oxidized moieties remain in TEGO. In addition, this almost amorphous contribution means that no long-range order is

observable along the stacking direction of the graphite planes. Previous neutron scattering experiment confirmed that TEGO that TEGO is a multilayer graphene with turbostratic disorder, with 3 layers as average [146], meaning that single layers co-exist with few-layered graphene. TEGO is also characterized by a high surface area: Braun-Emmet-Teller (BET) analysis performed with nitrogen at 77 K yielded a specific surface area of ~ 600 m^2/g [186]. The DC conductivity of TEGO was measured as 9.4 (1) S/cm.

5.1.2 STRUCTURAL CHARACTERIZATION OF TITANIUM DIOXIDE NPS AND COMPOSITES

From now on, the samples of TiO_2 NPs and TiO_2 NPs composites with TEGO will be referred with a short ID to facilitate the readers in following the onward discussion section. The table below summarizes the synthesis, composition, and ID of the samples.

Table 5-1 List of samples studied in the current work, including long name, synthetic route, TiO_2 : TEGO weight ratio and a short ID to better identify the samples in the paper.

Sample	Synthesis method	TiO_2:TEGO (wt ratio)	Short ID
TiO_2 blank	Hydrothermal	100	**BL (Blank)**
TEGO scaffolded TiO_2	Hydrothermal	99:1	**HT1**
TEGO scaffolded TiO_2	Hydrothermal	80:20	**HT2**
TEGO ball milled TiO_2	Ball-milling	99:1	**BM**

As a first investigation step, a blank consisting of pure hydrothermal titanium dioxide nanoparticles (BL) was synthesized and tested along with two stoichiometries of

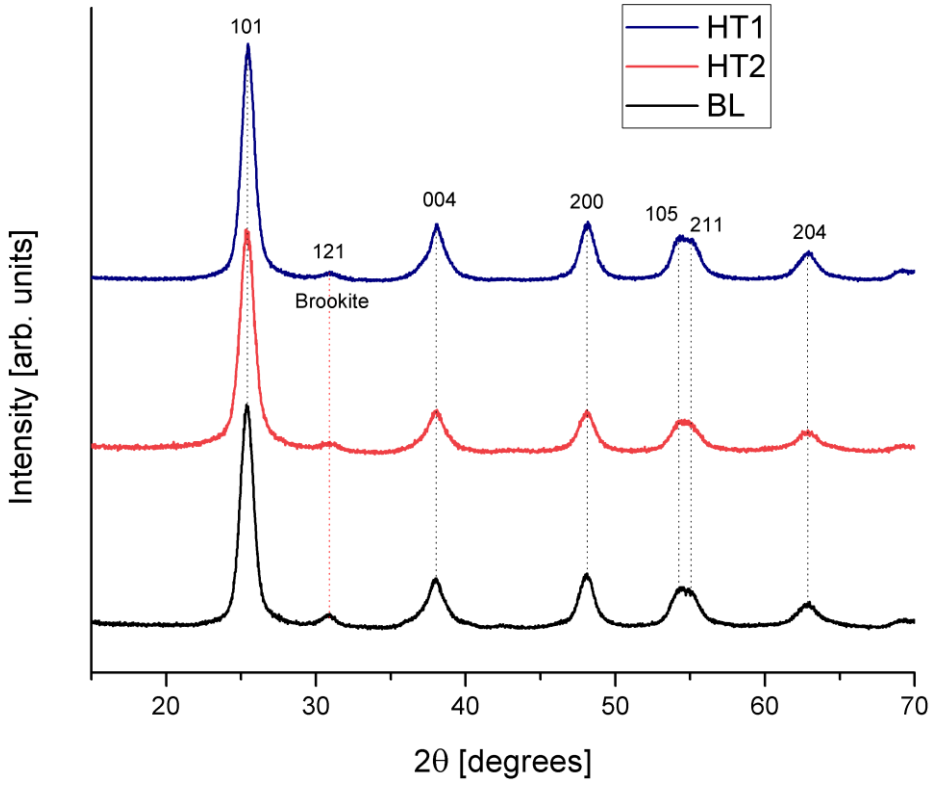

Figure 5-2 PXRD patterns of TiO_2-based samples, from top to bottom: TiO_2-decorated TEGO 99:1 (HT1, blue), TiO_2-decorated TEGO 80:20 (HT2, red) and pure hydrothermal TiO_2 (BL, black). The brookite peak (at $2\theta = 31°$) depletes and becomes less pronounced in the carbon scaffolded material.

hydrothermal synthesized TEGO-scaffolded TiO_2, to understand the optimal ratio between TiO_2 and carbon. Both HT1 (99:1) and HT2 (80:20) were investigated. Successively, a solid-state mixture between TiO_2 NPs and TEGO was tested following the 99:1 stoichiometry, which resulted being the optimal compromise in terms of graphene quantity/performance ratio. BL consists in a mixture of two TiO_2 crystal phases, namely anatase and brookite, as shown by PXRD (Figure 5-2). The mean crystal size of BL, calculated from the broadening of the diffraction peaks using the Scherrer equation through Rietveld refinement, results in an average 17.2(5) nm equatorial size. Rietveld method was also employed for the quantitative phase analysis. Anatase and brookite phase fractions were calculated being 87.1(3) % and 12.9(6) wt % respectively. The Zhang and Banfield estimation [187] allowed us to confirm the ratio between the two

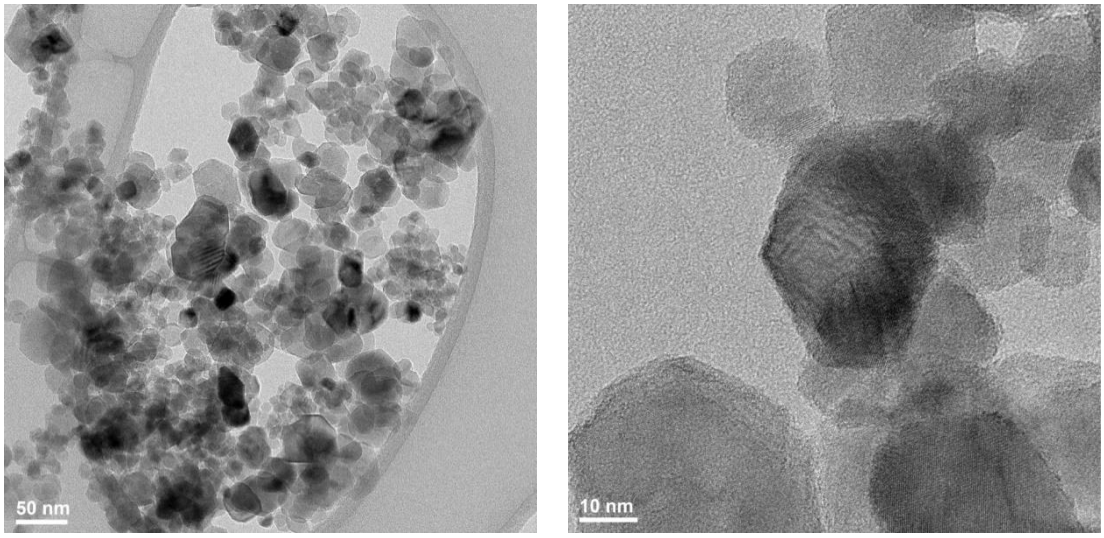

Figure 5-3 HRTEM images of BL. On the left, the size distribution of the crystal can be noticed, while on the right, at higher magnification, the characteristic shape of anatase can be appreciated. NPs have a mean size above 10 nm, thus the Scherrer estimation is confirmed.

phases within a narrow approximation. In the HT samples, ratios between anatase and brookite have proven to be slightly different than in BL. Both the HT1 and the HT2 samples showed a weight fraction of anatase of 91.5(5) %, and a brookite fraction of 8.5(1.0) %, thus showing a selective effect of the heterogeneous growth, favoring the anatase polymorph. In fact, it is known that heterogeneous crystallization on defective TEGO can promote the nucleation of smaller crystallites [146] and that TiO_2 nano crystallites with dimensions below 14 nm have the lowest total free energy, because of surface stress effects; this leads to a synergistic effect that achieves a higher selectivity towards the anatase phase. In addition, the TiO_2:TEGO ratio does not affect the polymorph selectivity, since their relative percentages remain unaltered by the TEGO content. The crystallite size estimation, performed with both Scherrer and the Zhang and Banfield estimation, gives 8.0(6) nm for HT1 and 7.1(5) nm for HT2 respectively. The BM sample is not reported in the PXRD diffractogram because its crystal symmetry was severely compromised by the milling process and its morphology will be better explained by HRTEM and Raman analysis. These estimations were confirmed by HRTEM characterization, which was conducted on the aforementioned samples. In Figure 5-3, BL

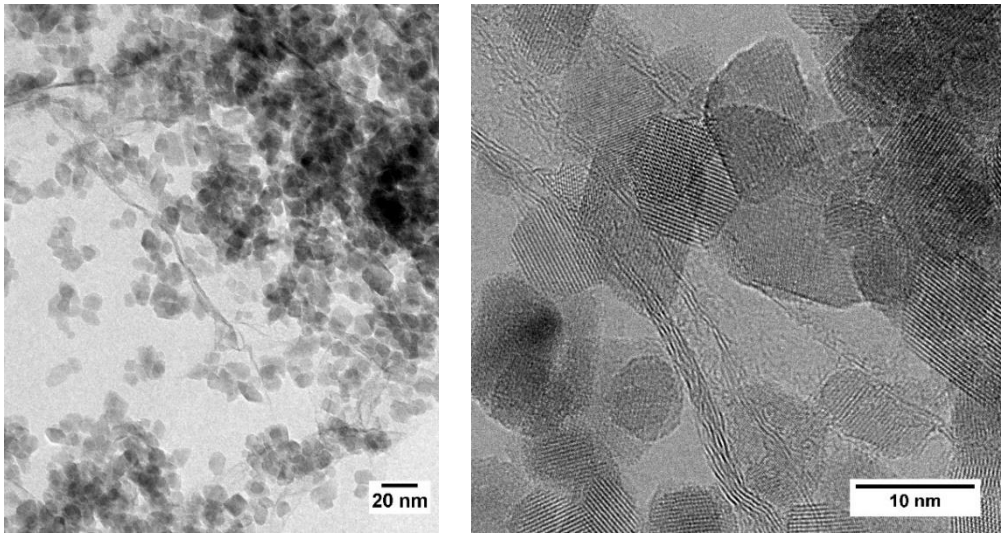

Figure 5-4 HRTEM images of HT1 at different magnifications. Both TiO_2 NPs and TEGO cross sections can be identified and characterized.

is shown at different magnifications. A spread distribution of crystal size can be noted in BL. The morphology of the crystallites shows the typical anatase features, i.e., truncated bipyramid shape (quasi octahedral, almost barrel-like). In some crystals the morphology appears different, and an almost spherical shape is observable. Also, in the case of HT samples, HRTEM analysis confirms the Scherrer-derived crystal size of TiO_2 NPs and give a clearer insight on the morphology of the sample. In particular, in Figure 5-4, two different magnifications of HT1 are reported. It immediately appears that the mean size is lower than in the BL sample, and also in this case both truncated bipyramids and quasi-spherical crystals coexist. In the high-magnification image, the typical 0.35 nm interplanar distance of the (101) periodicity can be visualized. In addition, when twisted at the right angle, the cross section of TEGO can be observed. It appears as wrinkly layers crossing the sample diagonally in both magnifications, but at higher resolution, the stacking of graphitic planes can be clearly seen. For this reason, in TEM analysis it is hard to detect single layered TEGO. Finally, HRTEM analysis was performed on BM sample. As aforementioned, no significative crystallinity was observable in the BM diffraction and this is confirmed by the TEM image, where the ordered and well-shaped

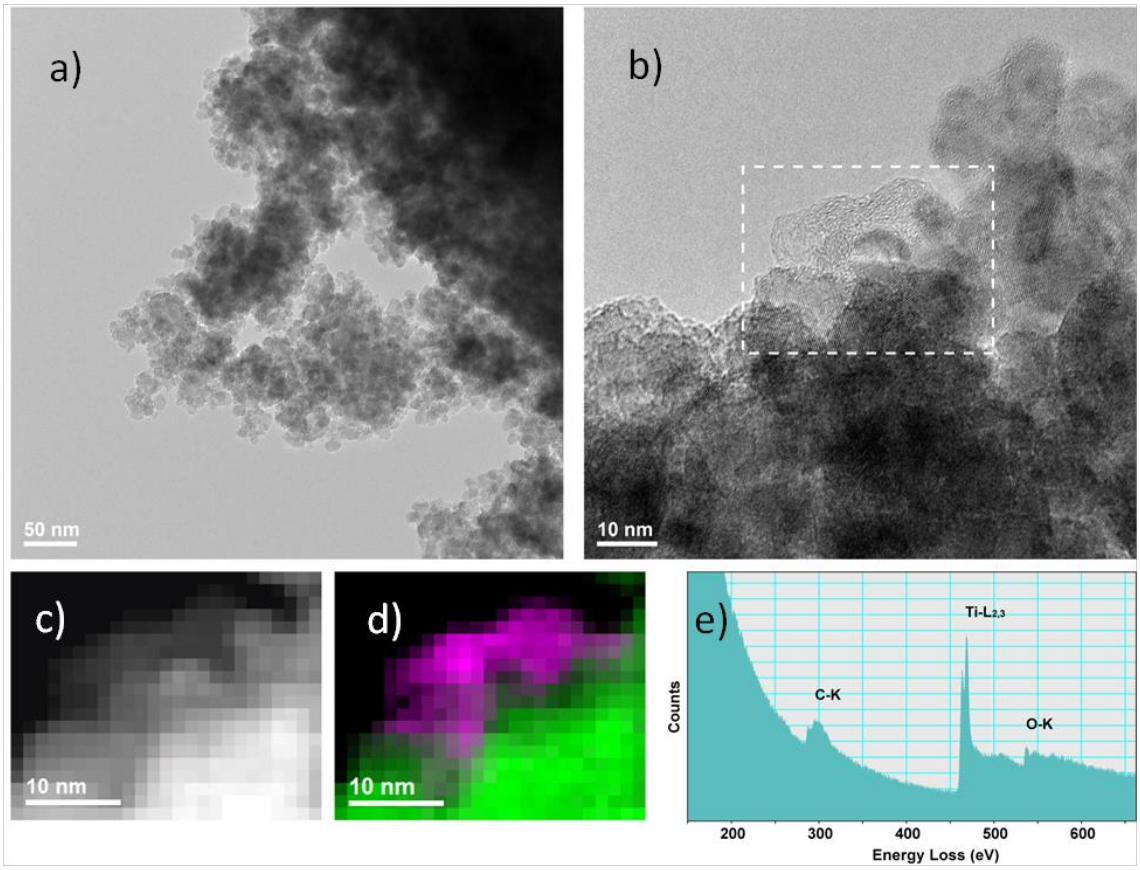

Figure 5-5 On top, figure a and b – TEM images of BM morphology, with an increasing magnification. Inside the white dashed line, a close up of carbon extending from the edge of the superstructure. On the bottom, c – crop of ADF signal of the region confined by the dashed line. d – colour map (C = purple, TiO_2 = green) employed to highlight the carbon in the sample, otherwise hard to detect. e – EELS spectrum of the crop.

bipyramid anatase nanocrystals observed in the previously investigated samples are not noticeable, and an almost amorphous cluster of TiO_2 NPs is observed (Figure 5-5). Apparently, high-energy ball milling tends to agglomerate TiO_2 in bulkier superstructures and amorphize the crystallites. In this study, longer milling times were also tested, all having the results of agglomerating the NPs, and eventually, after an initial amorphization, rutile, being the thermodynamically most stable polymorph, started to crystallize. In BM images, it is hard to see the periodicity of crystal planes, and the surface of the particles appears jagged, probably related to the high energy of the milling process. As a collateral result, TEGO does not appear as a sheet widely spread onto which TiO_2 NPs are tightly bound, but the milling process causes its folding in a nest-like structure

onto which the NPs are surrounded. It is possible to identify and quantify the carbon content at the edges of these superstructures, and its morphology appears more amorphous than pristine TEGO. Despite the amorphization, EELS spectrum integration confirms the weight percentages of TiO_2 and TEGO in BM. EDS quantitative measurement taken in a bulk region, with high particles density, produces the atomic and weight percentages reported in Table 5-2, that are similar to the expected values within a small degree of uncertainty, meaning that carbon was not lost during the process, despite being hard to recognize at a first glance.

Table 5-2 Elemental atomic and weight percentage composition of BM measured by EDS on TEM

Z	Element	Atom. Fraction (%)	Atomic Error (%)	Mass Fraction (%)	Mass Error (%)
6	C	3.58	0.74	1.65	0.18
8	O	64.51	18.62	39.66	9.08
22	Ti	31.91	7.87	58.69	10.16

The nanostructure of TiO_2 nanoparticles combined with TEGO was also proved by micro-Raman spectroscopy. Raman spectra on the HT and BL samples are shown in Figure 5-6. Crystalline anatase and brookite spectra are reported as reference in Figure 5-6a. As well as observed with the PXRD analysis, the BL sample consists mainly of anatase nanocrystals, together with a minor contribution of brookite (Figure 5-6a). The five Raman peaks of the anatase structure were found at ~147, 198, 397, 516 and 637 cm^{-1}, whereas weaker signals corresponding to brookite features were detected at ~243, 320, 355 cm^{-1} [188,189]. The strongest peak of anatase, occurring at 147 cm^{-1} with a linewidth (FWHM) of 22 cm^{-1}, is shifted and broadened compared to that of crystalline anatase (peak position at 143 cm^{-1}, FWHM 14 cm^{-1}). This behavior is typical of nanoparticles smaller than 15-20 nm [190,191]: according to the phonon confinement model, the anatase Raman peaks broaden and shift following their phonon dispersion curve.

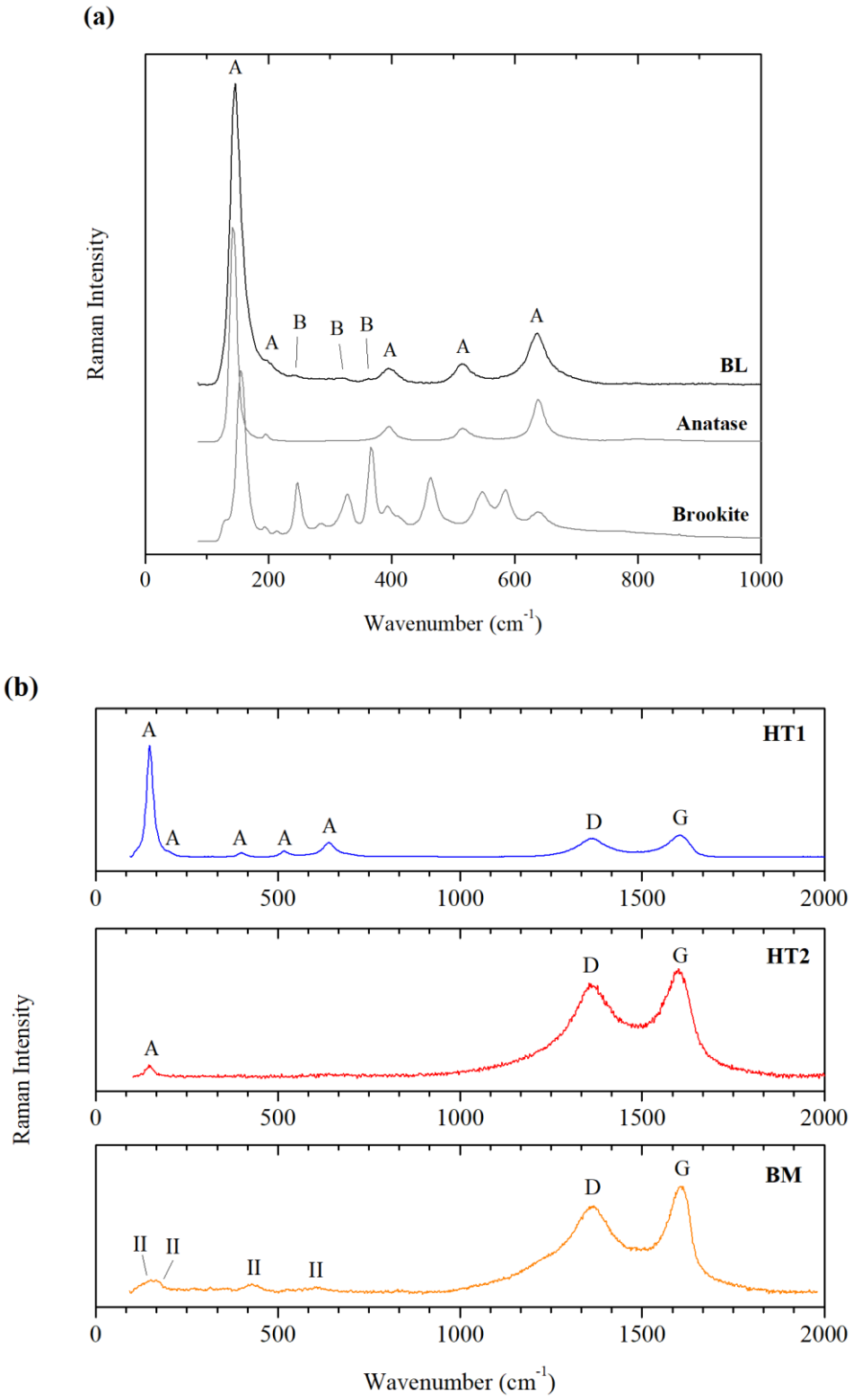

Figure 5-6 Raman spectra on BL and reference spectra of crystalline anatase and brookite; (b) Raman spectra on HT1, HT2 and BM samples. TiO_2 features are marked: anatase (A), brookite (B), TiO_2-II (II). Graphene features are marked as D and G bands.

Conversely, a sharp peak is observed in crystalline anatase, at the frequency typical of the Γ point of the Brillouin zone. In both HT1 and HT2, TiO_2 was identified mainly as nanocrystalline anatase, as shown in Figure 5-6b. In HT1, the anatase main peaks have been found at ~148, 200, 395, 517 and 640 cm^{-1}, whereas the brookite features are hardly visible. In HT2 and only the strongest peak of anatase has been detected. As well as observed for the BL material, the shift and broadening of the strongest anatase peak are assigned to the nanometer crystal size. Differently, in BM (Figure 5-6b), TiO_2-II has been obtained after the ball-milling treatment. Broad bands occurring at ~ 145, 170, 425 and 605 cm^{-1} were observed, corresponding to the high-pressure phase, as expected from a high-energy ball-milling treatment [192]. In the high wavenumber spectral range in Figure 5-6b, graphene signals are detected with the D and G bands, peculiar of carbon-based materials. The two broad bands occur at ~1360 cm^{-1} and ~1600 cm^{-1}, respectively. As the D band arises from disorder effects or defects in the imperfect crystalline structure, the defective structure of TEGO is further confirmed by the presence of the broad D band [193].

5.1.3 ELECTROCHEMICAL CHARACTERIZATION OF TITANIUM DIOXIDE NPS AND COMPOSITES

Electrochemical performance were tested via GCD analysis, within a potential window ranging from 2.5 to 1 Volt vs Li/Li^+. This range was chosen because it is an established protocol, already well known in literature [128,194,195]. The charge/discharge mechanism is already reported in paragraph 2.1.2. The cycles were performed with a rest time of 30 minutes between charge and discharge processes, as shown in Figure 5-7. The rest time is applied to give the electrode some time in order to reach the equilibrium state. In fact, after each semicycle, and mostly after high rates semicycles, the polarization of the electrode causes a gradient of lithium charges inside the electrode, with a subsequent

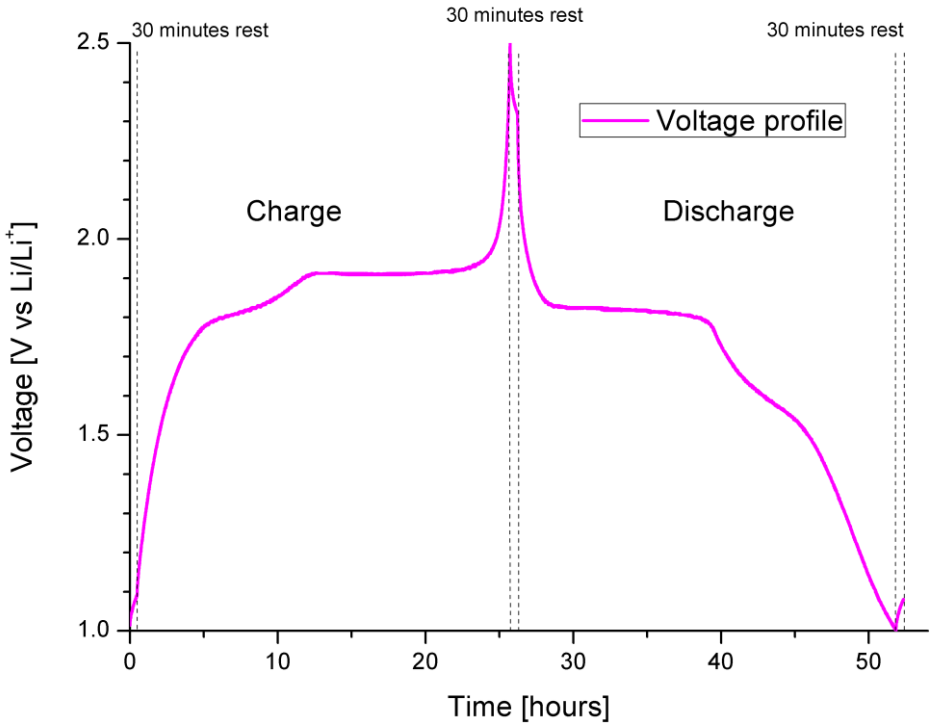

Figure 5-7 Typical charge/discharge profile of a titanium dioxide battery. Here is reported a slow rate (C/25) of a BL sample. After each semicycle, the cell undergoes a rest time of 30 minutes.

overestimation of the OCV. On the one hand, this protocol allowed us to understand the unbiased OCV after either the charge, or the discharge, since the system is in a non-equilibrium state at the edges of the potential window, while, on the other hand, allowed lithium to homogenously distribute from the front to the back of the electrode, whose motion is hindered by the known low Li ion diffusion inside TiO_2 matrix. From the capacity-cycles plot (Figure 5-8), a comparison between the different HT stoichiometries and the blank sample can be made. Pure TiO_2 shows no stabilization of the reversible capacity within the first charge-discharge cycle. At C/5 rate, a large specific discharge capacity of 184 mAh/g is achieved, but still a sudden capacity drop happens after few cycles, decreasing by 50% at the 10^{th} cycle. The reason of the important loss of reversibility is the impossibility of the system to perform a full lithiation and delithiation even at slow rates, due to the dielectric nature of the active material. With the addition of

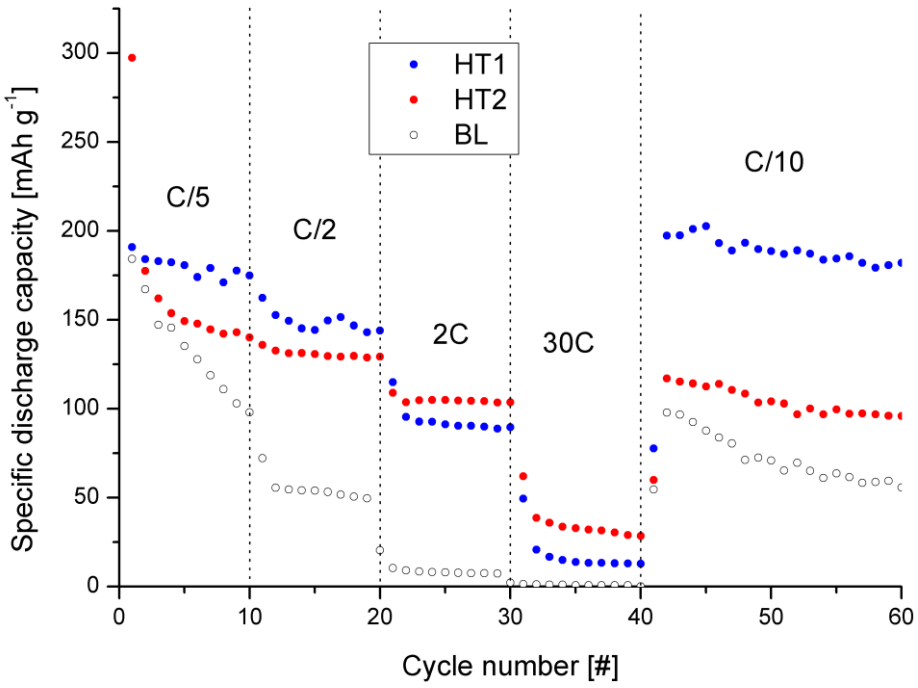

Figure 5-8 Comparison of BL, HT1 and HT2 sample. The capacities are displayed as a function of the cycle number. Different rates (from C/10 to 30C) are shown.

a moderate amount (1%) of TEGO (HT1) this effect is successfully buffered, leading to a capacity fading of just 8% within 10 cycles. In the sample HT2, a new phenomenon is observed. An enormous 297 mAh/g first discharge is registered, lowering at about 150 mAh/g after the first few cycles. This can be caused by the considerable TEGO fraction, which starts to show its own capacitive mechanisms at about 1.5 volt. As reported elsewhere, TEGO has a high surface area (~ 600 m^2/g [186]) and displays a huge first cycle capacity [196] that reduces almost ten times during the subsequent cycles. This is caused by a massive SEI formation that employs a lot of energy to develop through all the surface of the material, leading to a high irreversible capacity that stabilizes within the first couple cycles of the device. In HT2 this effect is highlighted by the relevant TEGO content of the electrode. At higher C rates, BL shows poor performance due to the low electrical conductivity of the system, despite the generous (10%) addition of carbon

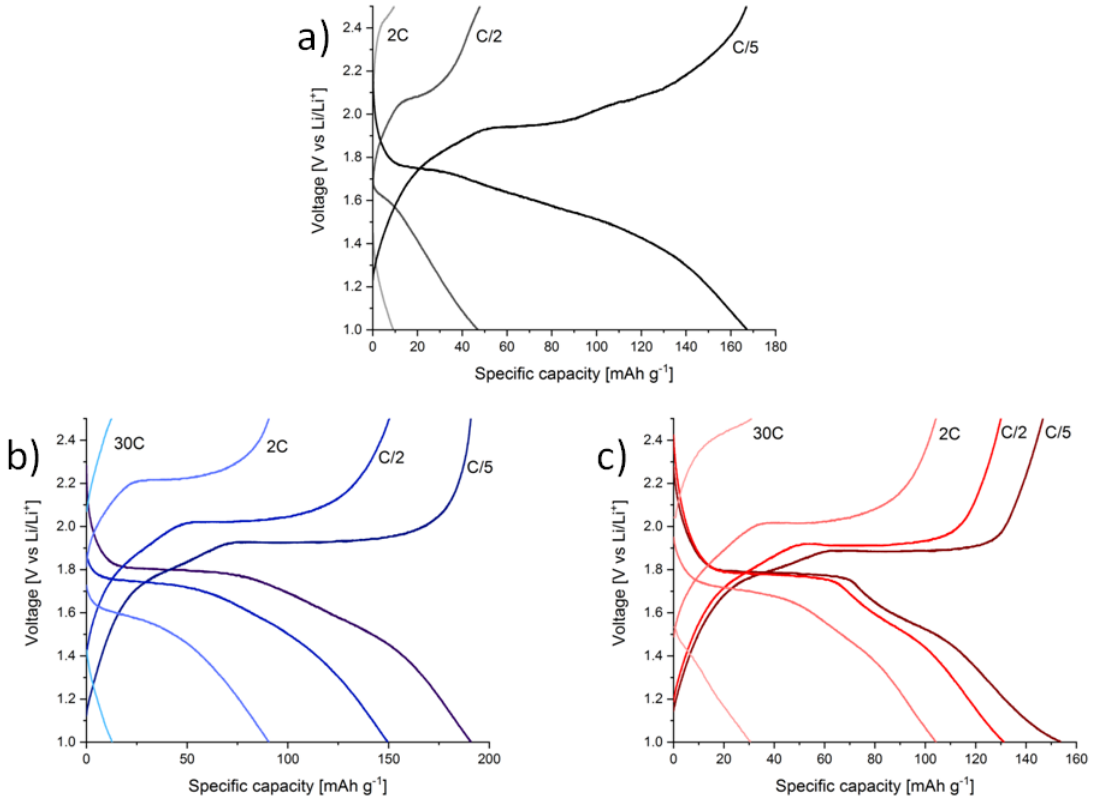

Figure 5-9 Charge-discharge voltage profiles of a) BL, b) HT1 and c) HT2. Several C rates are shown to highlight the samples behavior at different conditions. Higher TEGO content highlights a well-defined plateau, meaning that the redox contribution is predominant respect to the capacitive effects.

black in the preparation of the slurry. Anatase nanoparticles polarize immediately when solicited with high currents (up to 5 A/g) leading to a close to zero lithiation capacity. In HT1, it can be noticed how impactful a small amount of TEGO is: at 2C rates, the reversible capacity reaches up to 90 mAh/g, while depletes under 20 mAh/g at 30C. HT2 on the other hand, despite showing modest performance compared to the 99:1 stoichiometry at low C rates, proves its benefits at high C rates. The considerable amount of TEGO surrounding the anatase nanoparticles improves the high rate cyclability of the system allowing a reversible capacity above 30 mAh/g at 30C, meaning about 20% of the theoretical capacity in less than two minutes of charge time. The increased capacity at high rates is allowed by TEGO in two independent ways: on the one hand, the electrical

conductivity of TEGO allows high-rate charge-discharge processes preventing polarization effects; on the other hand, anatase decorated TEGO displays a smaller crystallinity, allowing a more rapid and efficient lithium exchange at high rates. As it is known, these high-rate processes mostly operate via fast mechanism on the surface of TiO_2 nanocrystals, meaning smaller particles may lead to better high-rate storage. In fact, the charge-discharge mechanism can be divided into three regions [65], that can be observed in the capacity/voltage diagrams reported in Figure 5-9. These 3 regions can be divided as:

1. A first, monotonic steady stage in which voltage drops rapidly due to the onset of the lithium insertion/extraction, in a quasi-solid solution mechanism.
2. A second stage, a long flat plateau corresponds to the crystal phase transition of the lithium titanate. This phase transition is dictated by the intake/release of Li ions, which causes a shift in the atomic arrangement of TiO_2.
3. At this point, no more lithium can be reversibly intercalated inside the TiO_2 structure, however further storage can occur at the particle interfaces. The third stage is thus characterized by a steep decrease of the potential, since no phase transition occur [65].

Since the HT1 was proven as the best overall sample, with the exception of high current density charges and discharges in which the HT2 stoichiometry provided better results, a different synthetic approach was tested maintaining the same TiO_2:TEGO ratio. BM sample was produced with a 99:1 weight ratio as reported in the Methods (4.2.1.3) section. The electrode and the half-cell were then assembled in the same fashion of the other samples. This sample was synthesized and tested to better understand the role of crystal size and TEGO. It was proved that TiO_2 nanoparticles grown on TEGO show smaller mean crystallite size, as compared with bare TiO_2 sample, but to better understand the electrical role of the material we reduced the crystallite size of BL and mixed it with a tiny amount of TEGO, to confirm the crucial role of the impregnation of the matrix by the organometallic precursor. An improvement in capacity and reversibility was achieved compared to BL sample through this fast and facile synthesis, even though the results did

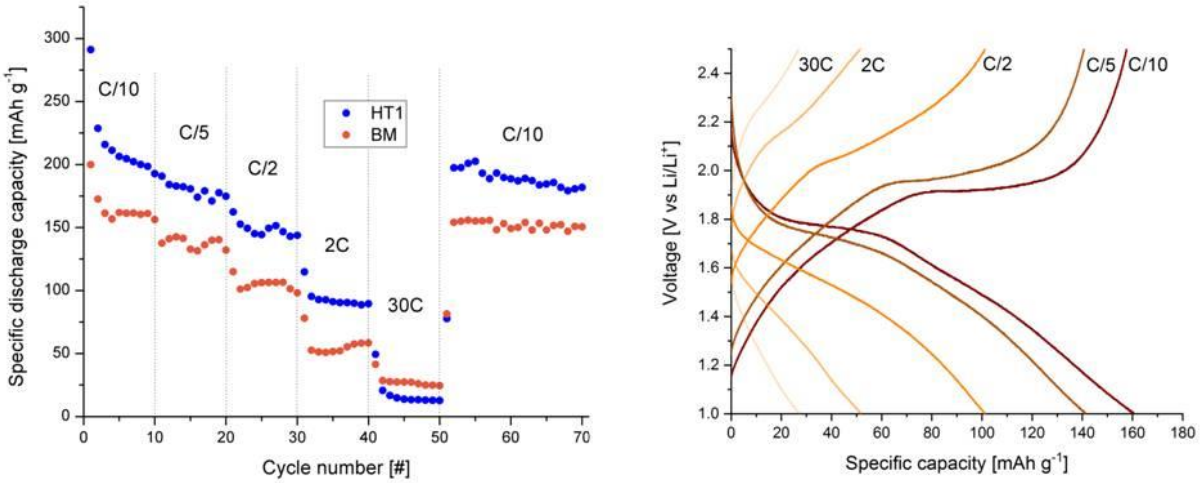

Figure 5-10 On the left: Comparison between the specific gravimetric capacities of HT1 and BM. On the right: Charge-discharge voltage profiles of BM

not outperform HT1 sample, as shown in Figure 5-10. Electrochemical performance still offer an improvement to the blank sample. By simple milling of the conductive carbon a good enhancement of the specific capacity is observed, and even though slow rates capacity is lower than HT1, at high current densities an improvement of the milled sample is highlighted. This could be explained by the good dispersion of the carbon material due to the high energy milling, that can cause the reduction of the lateral size of the graphene platelets, thus obtaining a more distributed graphene network.

5.1.4 STRUCTURAL CHARACTERIZATION OF OPERANDO TITANIUM DIOXIDE BASED BATTERIES

To understand and compare the lithiation mechanism of the BM and HT1 sample, an operando powder diffraction experiment to analyze the structural evolution of the operating cells was carried out at ELETTRA on the beamline Materials Characterization

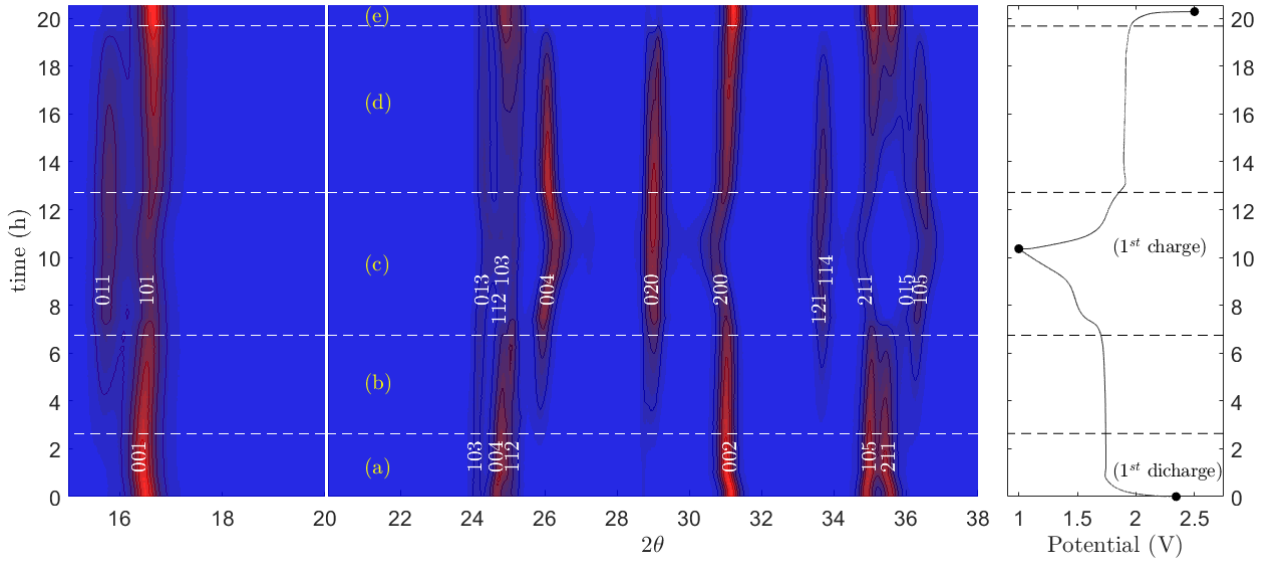

Figure 5-11 : 2D diffraction evolution (left panels) and galvanostatic discharge/charge profile (right panel) for the BL half-cell cycled at C/10. Different indexing of peaks during time highlights the main reflections characterizing the evolution from the initial anatase structure to $Li_{0.5}TiO_2$ in the lithiated electrode. Dashed horizontal lines mark the topic onsets in the structure and discharge/charge profile (see main text). Contrast in the range 20-38° in 2θ has been increased compared to range 15-20° to show less intense peaks.

by X-ray diffraction (MCX). SXRPD patterns were collected operando both for the BL electrode and for the most performing 99:1 systems HT1 and BM upon cycling at C/10. From a structural point of view, the data acquired show a smooth phase transition of the anatase upon lithiation. Figure 5-11 reports the data collected on the blank TiO2-containing LIB (BL). For the sake of clarity, the minor fraction of brookite (barely observed at this grade of profile resolution) was neglected from the following analysis. The first complete discharge (about first 10 hours in Figure 5-11) is followed by a complete charge (about from 10 to 20 hours). During the first drop in voltage [region (a) in Fig. 5-11] the powder patterns can be entirely indexed using the anatase phase, the main reflections of which are indexed in the figure. In parallel to the establishment of the 1st plateau in the voltage [region (b)], the reduction in intensity of the tetragonal anatase peaks is accompanied by the increase of the Li_xTiO_2 orthorhombic peaks. Of particular relevance is the appearance of the 011, 004, 020, 121, and 114 peaks which are forbidden reflections in the *I4₁/amd* lattice. During the 2nd plateau and across the switching in current of the 1st charge [region (c)], the entire electrode is lithiated to the orthorhombic

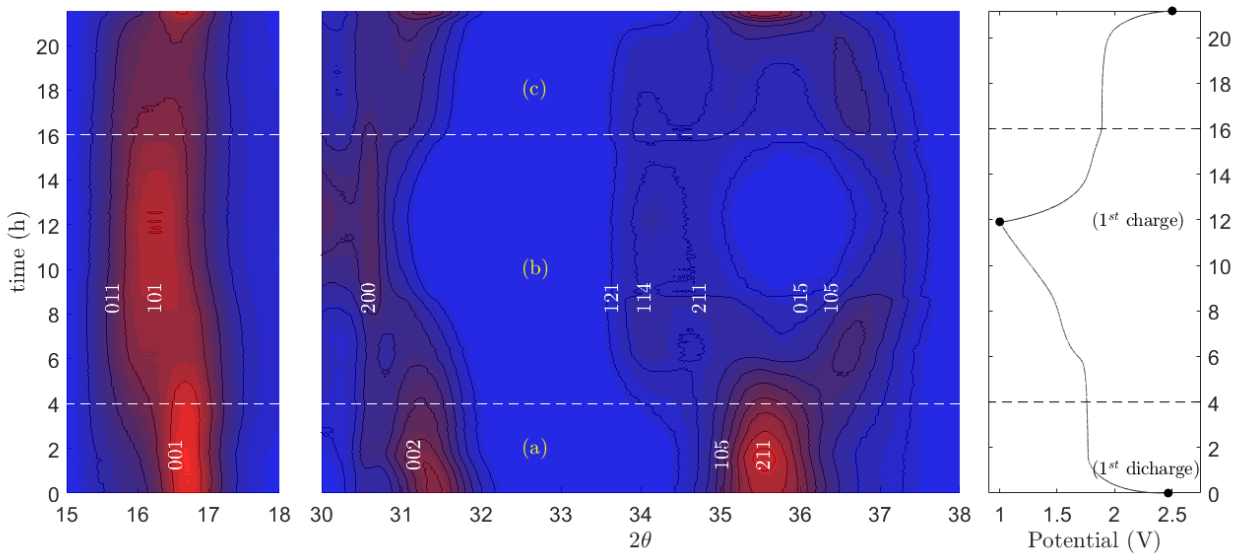

Figure 5-12 2D diffraction evolution (left panels) and galvanostatic discharge/charge profile (right panel) for the HT1 half-cell cycled at C/10. Different indexing of peaks during time highlights the main reflections characterizing the evolution from the initial anatase structure to Li_xTiO_2 in the lithiated electrode. Dashed horizontal lines mark the topic onsets in the structure and discharge/charge profile (see main text). Contrast in the range 30-38° in 2θ has been increased compared to range 15-18° to show less intense peaks.

phase. Upon reaching the minimum voltage, the Li_xTiO_2 phase shows further contraction along the *c*-axis and expansion along the *a*-axis, as highlighted by the shifting of the 004 and 200 reflections and as observed in detailed studies of pure TiO_2 nanoparticles [197], pointing to the formation of $Li_{0.5}TiO_2$, which corresponds to the maximum uptake of lithium. From the structural point of view, the 2nd plateau during the charge process [region (d)] and the final rise in voltage [region (e)] display specular features with respect to the discharge process, ultimately leading to the complete and reversible conversion of $Li_{0.5}TiO_2$ to anatase. The diffraction patterns of the electrodes composed by HT1 and BM samples appear much less clear in terms of peaks separation and intensity compared to BL and the main cause might be found behind factors such as a lower fraction of active material under the beam, finer sizes of the particles, and an increased disorder. For example, the 105 and 211 reflections in the anatase phase or the 011 and 101 ones in the Li_xTiO_2 phase, which were well deconvoluted in the BL patterns, now appear as single convoluted peaks for HT1 and BM, due to profile broadening. Moreover, and increased number of extrinsic features was observed in these patterns (mostly due to scattering from

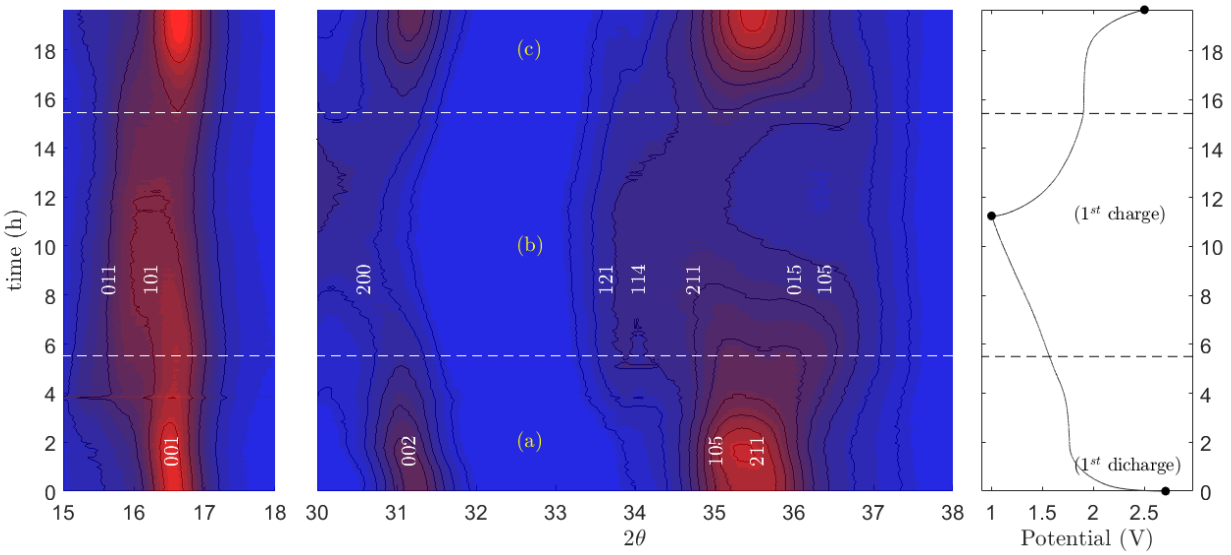

Figure 5-13 2D diffraction evolution (left panels) and galvanostatic discharge/charge profile (right panel) for the BM half-cell cycled at C/10. Different indexing of peaks during time highlights the main reflections characterizing the evolution from the initial anatase structure to Li_xTiO_2 in the lithiated electrode. Dashed horizontal lines mark the topic onsets in the structure and discharge/charge profile (see main text). Contrast in the range 30-38° in 2θ has been increased compared to range 15-18° to show less intense peaks.

the aluminum electrodes) which were not possible to mask completely during the data reduction procedure or fit as background during the refinement process. Given the scarce resolution, a quantitative analysis based on the Rietveld approach appears daunting. Nonetheless, it is still possible to qualitatively follow the structural changes occurring during the discharge/charge process by focusing the attention on the most relevant ranges highlighting changes in symmetry and appearance of forbidden reflections. For this purpose, figures 5-12 and 5-13 display magnified ranges at 2θ=15-18° and 30-38°, less affected by extrinsic features and featuring the main distinct peaks of anatase and Li_xTiO_2. The HT1 electrode displays a progressive lowering in intensity of the 001, 002, 105, and 211 reflections during the beginning of the first discharge [region (a) in Figure 5-12] followed by the appearance of orthorhombic features (in particular, reflections 011 and 101 at low angle and 200, 114, and 105 at higher angles) during the second part of the discharge and the beginning of the 1st charge [region (b)]. At the maximum extent of lithiation the peaks ascribed to the anatase phase are completely extinct. In the final part of the 2nd discharge [region (c)] the anatase peaks appear again at the expenses of the

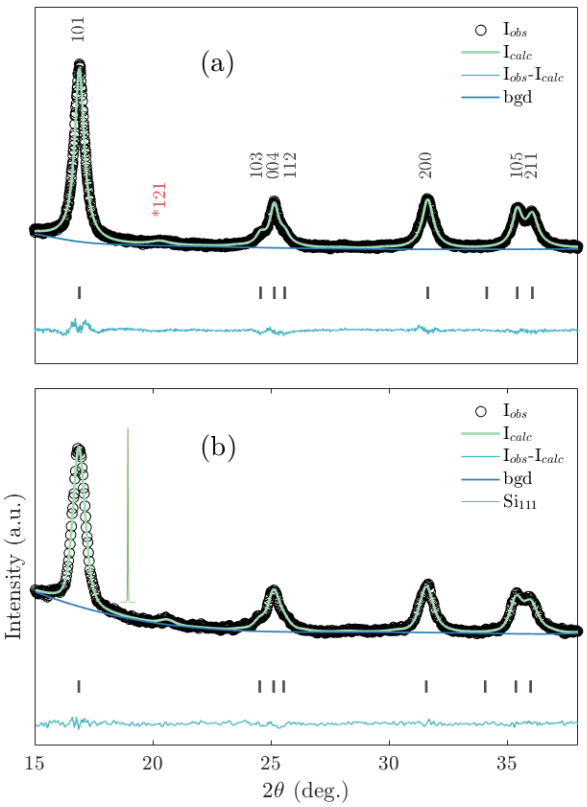

Figure 5-14 Rietveld refined parameters for Pure TiO_2 and HT1 analysed from high-resolution SXRPD reporting the relative weight fractions for anatase and Brookite and main structural parameters for anatase (axial and equatorial domain sizes, isotropic microstrain, and lattice parameters).

Li_xTiO_2 features. The discharge/charge process of the BM electrode (Figure 5-13) is even harder to quantify due to a lack of distinct features in the high angle range. However, it is still possible to trace the transition from anatase to Li_xTiO_2 by following the initial shift of the 001 peak [region (a) in Figure 5-13] followed by its further broadening, marking the appearance of the 011 and 101 Li_xTiO_2 reflections [region (b)] and the ultimate reversible conversion to anatase in the second half of the 1st charge process [region (c)], marked by the reappearance of the 002, 105, and 211 reflections of anatase. While the 1st plateau at 1.7 V, corresponding to the first transition from anatase to Li_xTiO_2 (for x between 0.05 and 0.25) is clearly observed in all three samples, the second plateau, related to the further lithiation from x=0.25 to 0.5, is clearly discernible only for BL and HT1, suggesting a less-uniform trend of lithiation in BM. Overall, the best performance

obtained for HT1 calls for a more detailed comparison between pristine TiO_2 and the sample obtained via hydrothermal impregnation. Figure 5-14 reports the high-resolution SXRPD patterns of BL and HT1 as measured for the powders using the 1D detector and the goniometer, showing the same range displayed in Fig. 5-11. The best refinement was obtained using both anatase and brookite phases and allowing for the profile fitting employing the model for uniaxial size broadening and the isotropic microstrain approximation. The results are displayed in table 5-3. The sample obtained via impregnation method using only 1 wt% of TEGO (HT1) results in a slightly larger fraction of anatase composed by smaller nanoparticles (below 10 nm as opposed to 15-20 nm of BL). A slight variation is also observed in the refinement of the lattice parameters, which leads to a slightly expanded lattice for HT1. Microstrain effects appear to be not negligible and comparable for both samples, most likely due to surface effects typical of nanosized particles. The reduced size of crystalline domains for HT1 is suggestive of a more efficient nucleation process occurring when TEGO is used as support.

Table 5-3 : Room temperature synchrotron X-ray powder diffraction data and Rietveld refinements for (a) BL and (b) HT1 powders. Vertical tick marks highlight reflections of anatase, with Miller's indexes in (a) featuring the main reflections of anatase (black). The most detectable reflection of brookite (121) is emphasized (in red) by an asterisk. The silicon 111 reflection is also displayed, rescaled in intensity, in (b) to show the instrumental resolution.

Sample	**Anatase (%)**	**size-ax (nm)**	**size-eq (nm)**	**μ-strain (Δd/d %)**	**Brookite (%)**	**size-iso (nm)**	***a,b* (Å)**	***c* (Å)**	**R_{wp} (%)**
BL	87.1(3)	19.3(4)	14.7(2)	0.85(4)	12.9(6)	6.0(3)	3.7911(4)	9.4972(7)	6.7
HT1	91.5(5)	11.6(4)	9.25(16)	0.93(1)	8.5(1.0)	7.2(2)	3.7977(4)	9.5086(12)	4.4

5.2 SULFUR-BASED CELLS

In this chapter, the crystal structure, morphology and electrochemical performance of sulfur cathodes is discussed. Three different techniques were tested to produce sulfur:carbon composites, namely thermal infiltration, high energy ball-milling (both all-solid state and liquid assisted milling) and chemical decoration. From now on, in order to make the dissertation easier to read, the samples obtained by thermal infiltration will be referred as "*S - TEGO dT*", the ones synthesized by ball-milling method as "*S - TEGO BM*", or "*WBM*" in case of wet ball mill, and finally the ones prepared by chemical decoration will be called "*S - LAArGO*". The synthesized materials were investigated by PXRD technique, in order to observe the crystal structure of the active material. Subsequently, SEM imaging was carried out on some of the most representative samples, in order to understand the morphology of the sulfur composites. Finally, GCD was performed and the different techniques and stoichiometries were compared, in order to understand the most performing way to decorate the investigated high surface area carbons.

5.2.1 STRUCTURAL CHARACTERIZATION OF SULFUR BASED COMPOSITES

As in the case of TiO_2-containing LIBs, the first investigated sample consisted of a pure sulfur electrode (*blank*). The blank electrode was prepared starting from elemental sulfur from Sigma-Aldrich (S_8, 99,998% purity) that was mortar ground with CB and PAA. At first, a high cathodic loading was tested (75 active material, 5 CB and 20 PAA w/w%), but the cells prepared with this procedure did not achieve any significant results. When a higher CB ratio was tested (40 active material, 40 CB and 20 PAA w/w%),

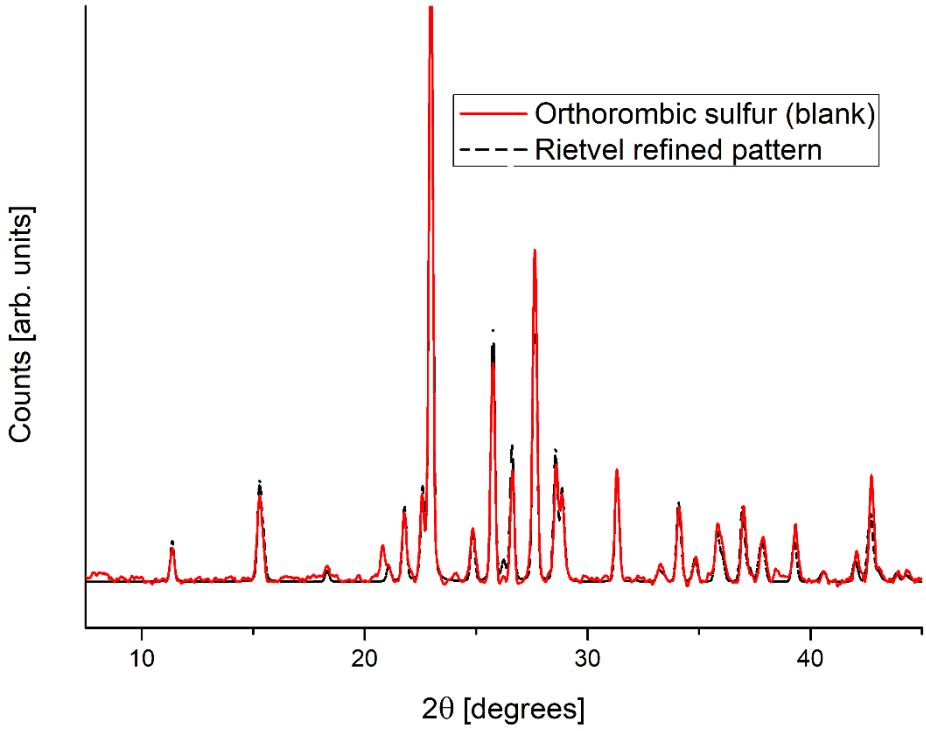

Figure 5-15 Diffractogram and Rietveld refinement of pristine sulfur (Sigma-Aldrich)

electrochemical results were observed. This is a known phenomenon, and normally high carbon:sulfur ratios are employed, in order to buffer the typical Li/S cell detrimental effects listed in chapter 2.2.2. Molecular sulfur bought from Sigma-Aldrich is high purity (99.998 %) and was employed without further purification processes (diffraction pattern shown in Figure 5-15). The crystal dress of the powder matches the orthogonal phase, which is the most stable polymorph at room temperature. The crystal structure was Rietveld refined and cell parameters a,b and c were quantified as: a = 10.4(6) Å, b = 12.8(7) Å, c = 24.4(8) Å. After the blank sample, a simple solid-state composite was synthesized, from now on referred as S-TEGO BM. For this synthetic route, both S:TEGO 50:50 and 70:30 weight ratios were produced and analyzed. For this synthesis, TEGO previously reduced in volume and sulfur were ball-milled. No transformations in the crystal structure is observed after the high-energy milling, as shown in Figure 5-16. The orthorhombic lattice is maintained during the process, but a small broadening of the peaks

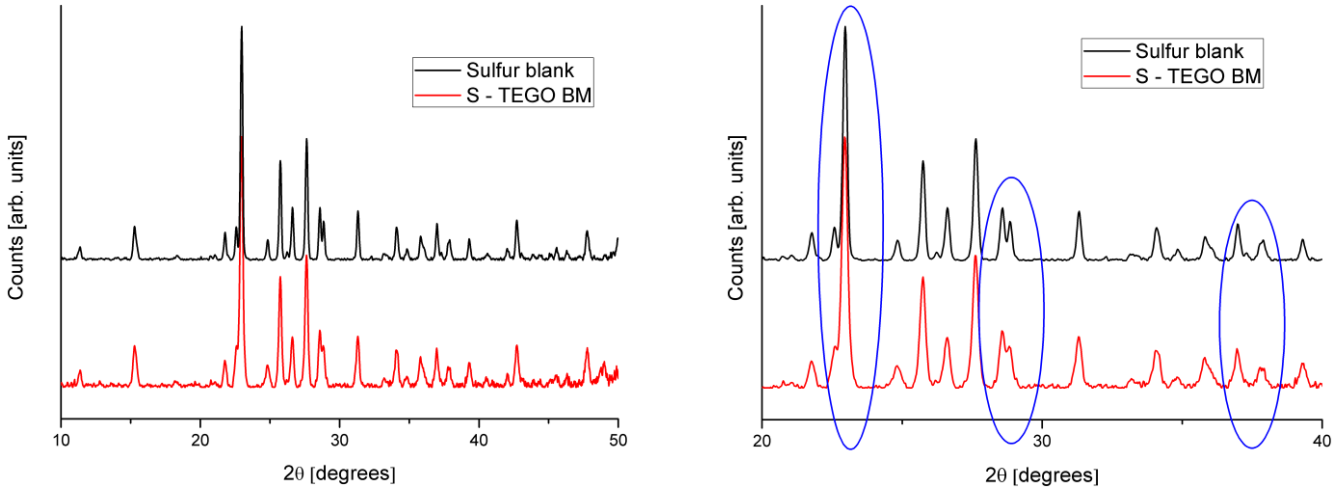

Figure 5-16 Comparison between the diffractograms of pristine sulfur and S – TEGO BM composite. On the right, a close detail of the broadening of the milled peaks, where some signals merge because of the decreased crystal size.

is noticeable, due to the fracturing of the coarse sulfur crystallites into smaller pieces. The resulting particles still have a crystallite size of a few microns and the Rietveld refinement cannot provide a precise estimation of the particle size. Macroscopically, the milling process leads to an almost impalpable black powder. When observed at SEM, it appears that the material agglomerated in corpuscles, with sizes ranging from a few microns up to hundreds of microns, as shown in Figures 5-17 and 5-18. High magnification images help to unravel the nature of these corpuscles, which are in fact made of TEGO sheets that were agglomerated into these superstructures, in which sulfur is both trapped and decorating the surface, as it can be seen in higher magnification images, where sulfur crystallites eventually show their orthorhombic sharp facets. In these samples, the trapping of the molecular sulfur is not very effective, since the active material should be hosted inside the carbon structure and not on the surface. In addition, the carbon structures show many differences from the TEGO wrinkly layers observed by TEM in chapter 5.1.2, appearing as tightly bound and closed structures, which may likely cause an obstacle in making all the active material available for the redox process in the final device. The

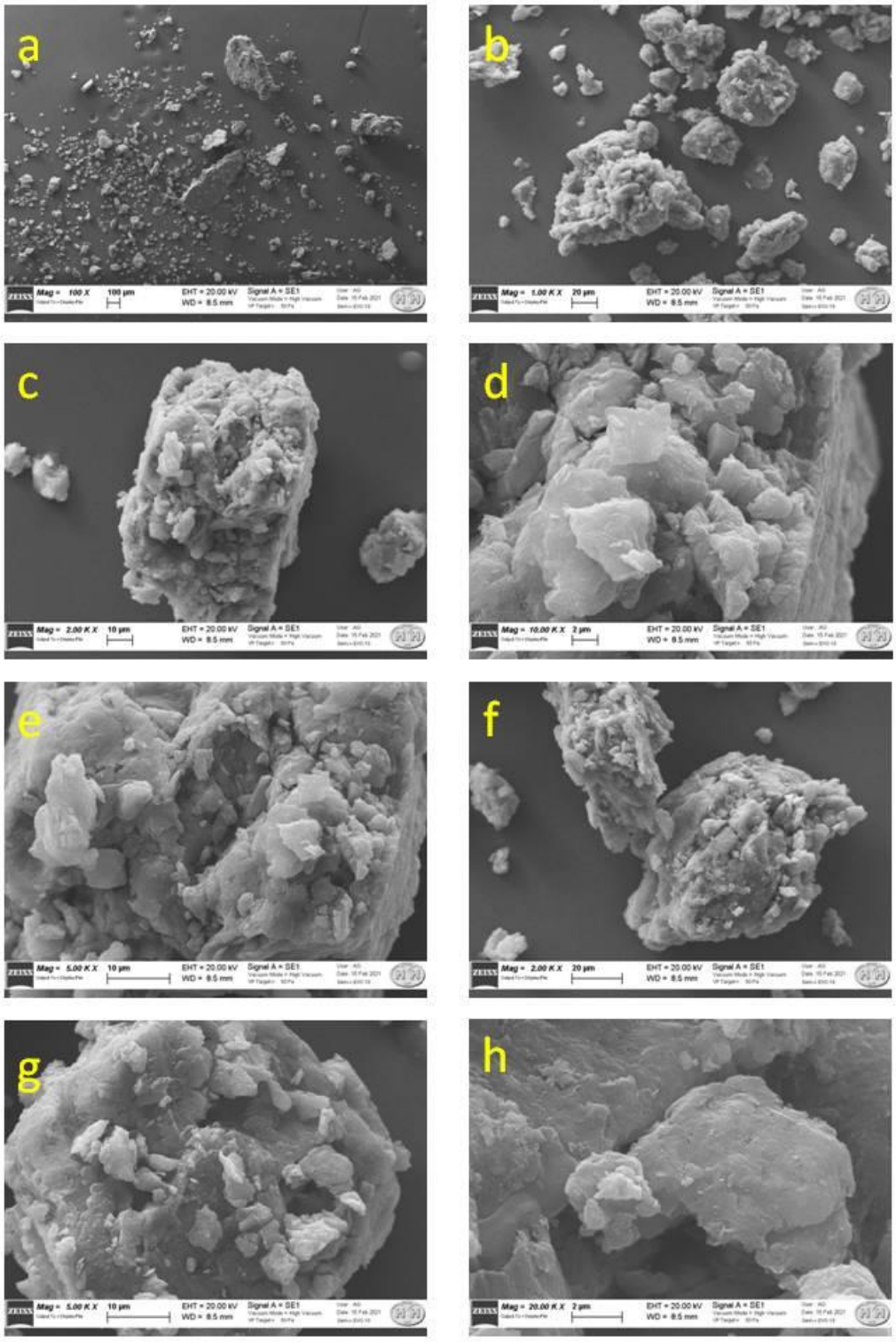

Figure 5-17 SEM images at different magnification of S - TEGO BM 70:30. The sample appears powdery and organized in globules and flakes. The appearance of TEGO is deeply altered by the milling process.

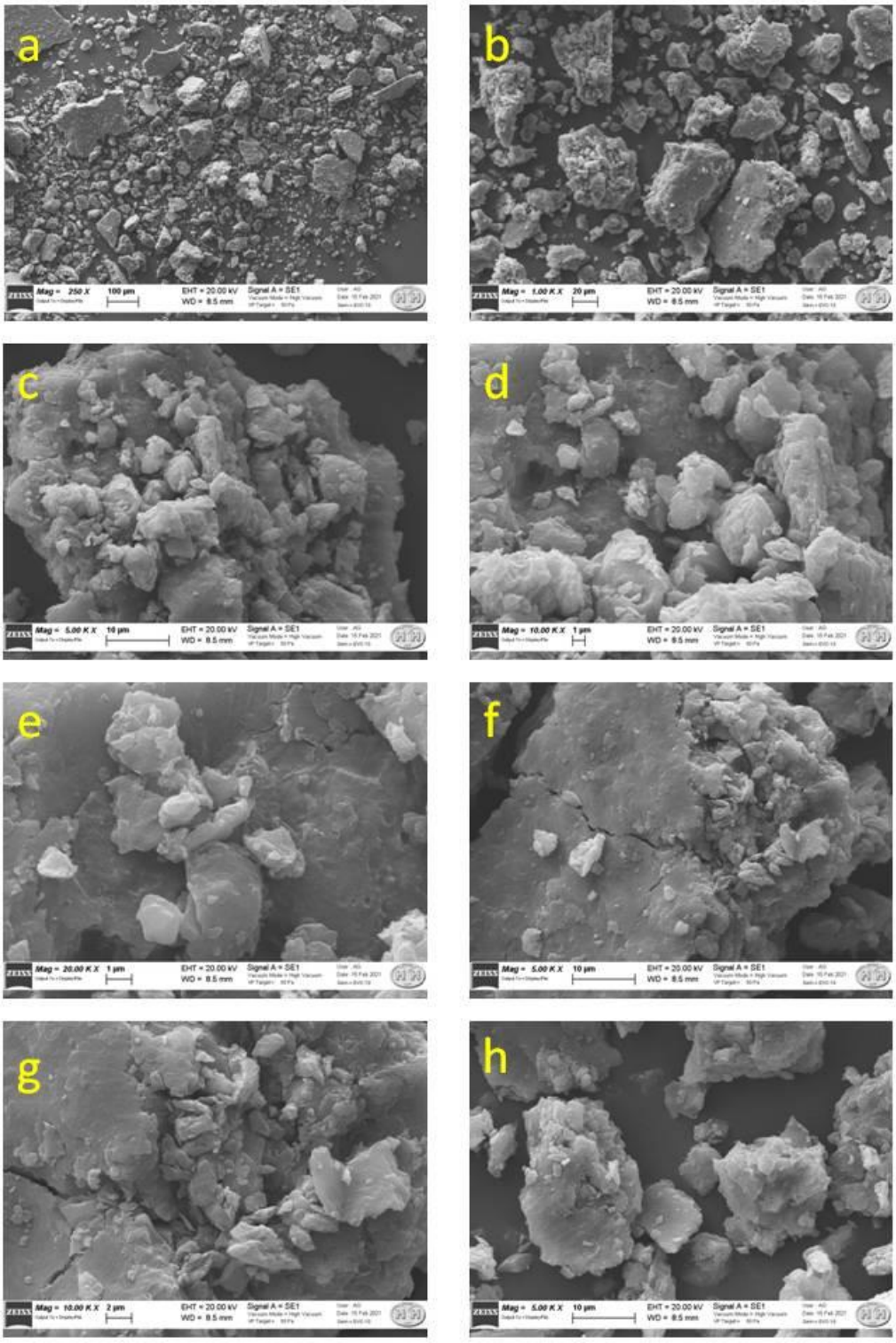

Figure 5-18 SEM images at different magnification of S - TEGO BM 50:50. The material appears similar to the 70:30 sample. Elemental sulfur appears to be less abundant, sometimes even hard to detect. It must be kept in mind that the ratios are in weight, and that the apparent volume of carbon is higher than sulfur.

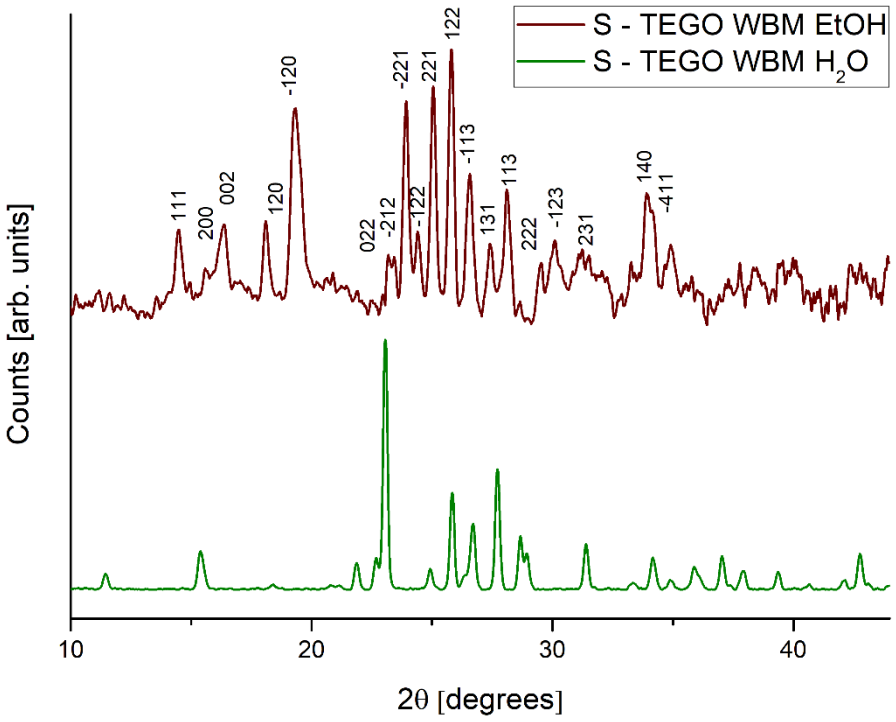

Figure 5-19 Comparison between the two liquid-assisted ball mill synthesis. The samle employing ethanol as a process liquid shows a monoclinic structure, while the one employing water remains orthorombic like the starting material.

described features are observed in both the S – TEGO BM 70:30 and 50:50 samples, reported respectively in Figure 5-17 (70:30) and 5-18 (50:50). In addition to solid-state ball milling, two tests employing a liquid phase inside the grinding jar were carried out. The liquid-assisted milling process dampens the impacts in the jar and helps to dissipate the heat generated from the mechanical energy. Both water and ethanol were tested. In the former solvent, both sulfur and TEGO are completely non-soluble, while the latter can suspend TEGO and has a low K_{sp} for sulfur. This process leads to two structurally different products, as shown in Figure 5-19. within the case of water-assisted ball milling, the diffractogram shows a little variation with respect to the pristine sulfur, meaning that the crystal structure is maintained, and only a slight broadening of the peaks can be registered. On the other hand, when EtOH is employed, the crystal structure changes dramatically, obtaining a monoclinic system. This can be attributed to the dissolution and recrystallization process taking place during the milling procedure, in which during the

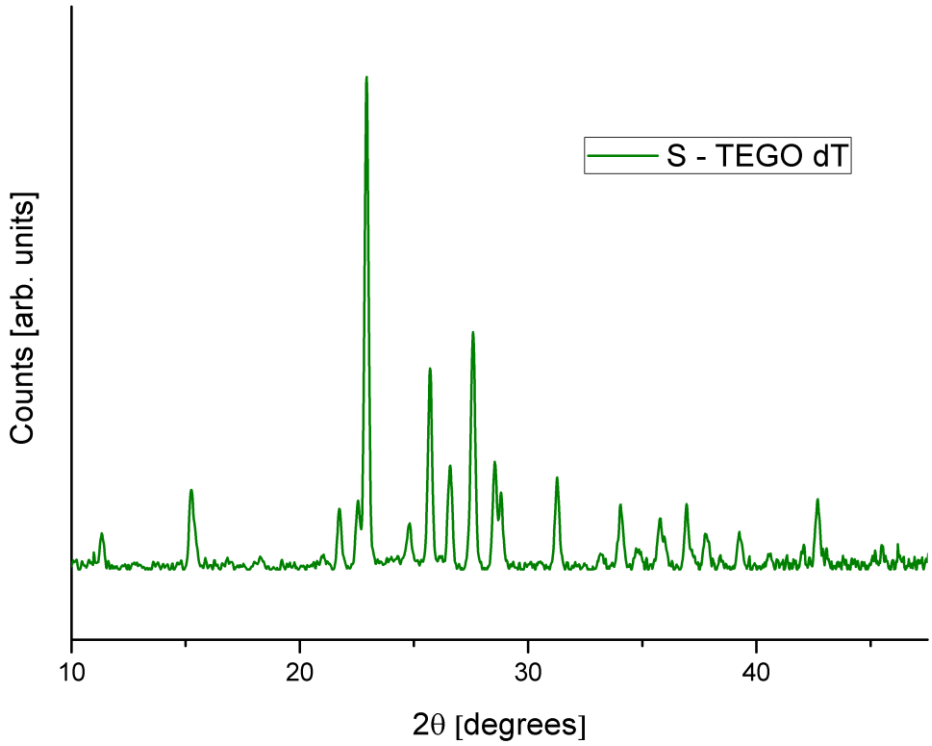

Figure 5-20 TEGO decorated with sulfur, obtained via thermal infiltration of the molten electroactive element. After the cooling of the system, the orthorhombic structure is restored, being the thermodynamically stable arrangement at RT.

milling process the system heats and successively, during the rest phases, cools down fast enough to allow a precipitation of the dissolved sulfur. This fast cooling favors the crystallization of the monoclinic (β) phase, which is stable at temperatures higher than RT, but it is retained if the cooling is fast enough. The crystalline symmetry of the material does not affect the performance of a Li/S cell, since sulfur is a conversion compound and the redox flow takes place regardless the crystal structure [198,199]. After the synthesis and characterization of ball-milled samples, another facile synthesis to obtain composites was tested. The second route was the thermal infiltration of molten sulfur inside a porous carbon host. Also in this case, TEGO was employed after being reduced in volume, to favor samples handle. The process included a slow cooling of the material after the thermal treatment, hence the orthorhombic structure was restored after

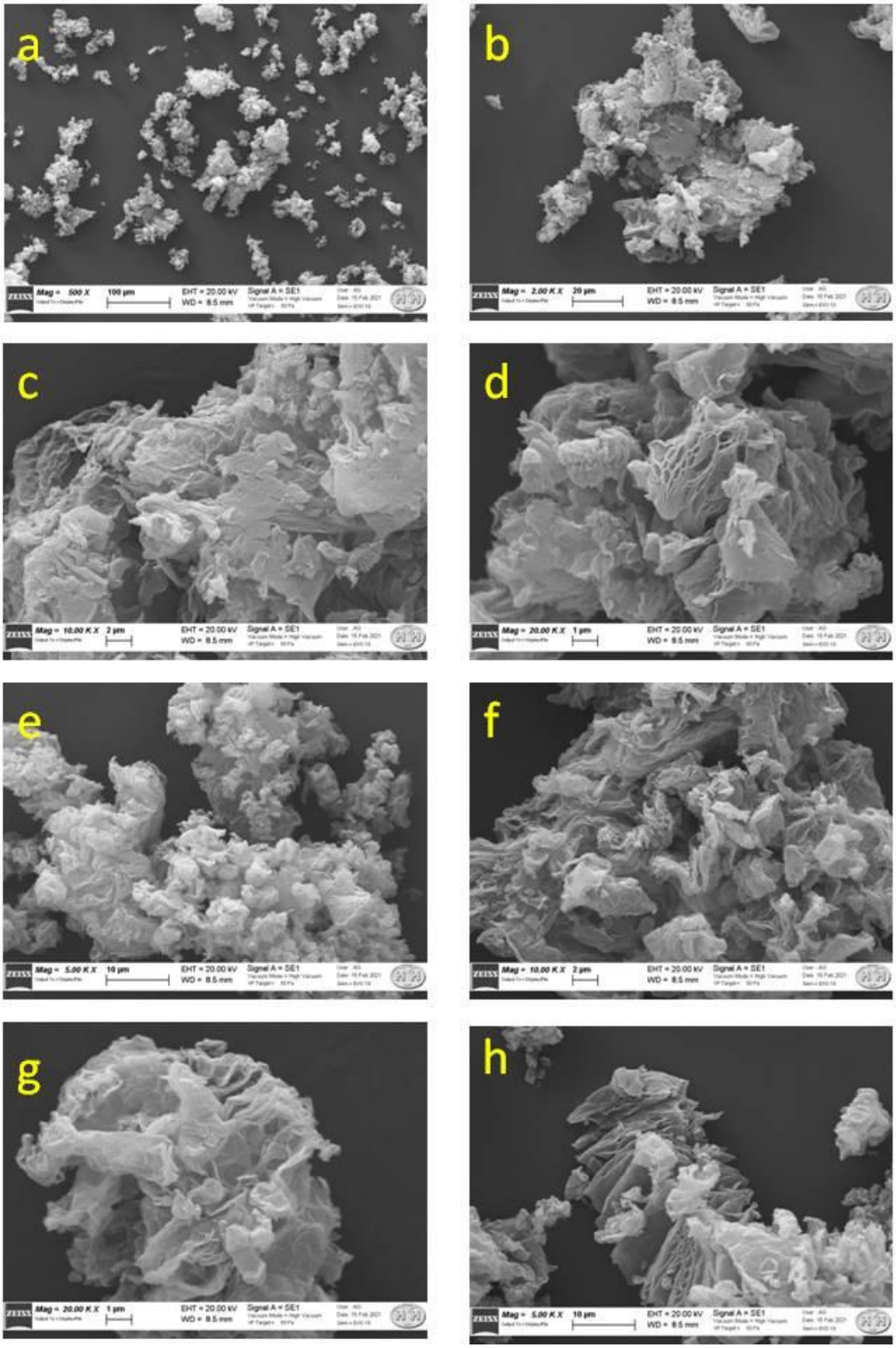

Figure 5-21 SEM images at different magnifications of S - TEGO 70:30 before (a,b,c,and d) and after (e, f, g and h) the thermal treatment, in which sulfur is effectively infiltrated inside the porous structure of TEGO, being barely noticeable on the surface of the scaffold in the latter images.

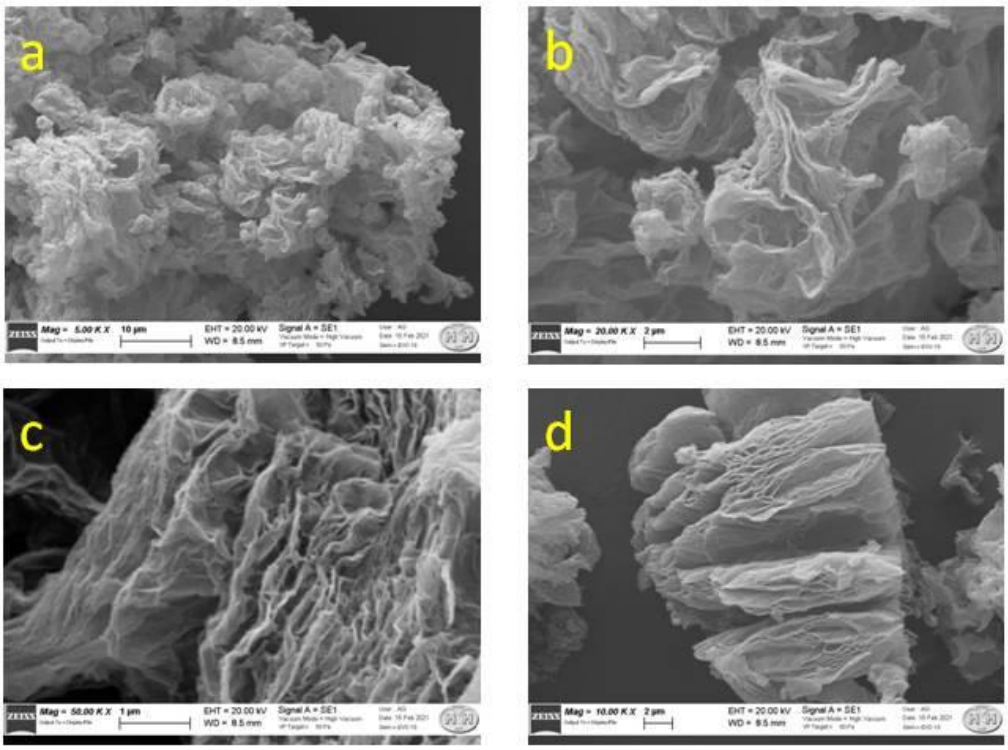

Figure 5-22 SEM images taken directly after the thermal infiltration of S - TEGO 50:50. Different magnifications are shown and the porous structure of TEGO can be noticed.

the melting and diffusion process, as shown in the diffractogram in Figure 5-20. Also in this sample, PXRD diffractograms suggest that the sulfur particles are in the hundred nanometers range, although this estimation was hard to confirm by SEM investigation. In fact, as shown in Figure 5-21, where the electronic microscopy images of S – TEGO dT 70:30 are reported, sulfur is hardly detectable after the thermal infiltration treatment. The first 4 images (a, b, c, and d) were taken before thermal infiltration, meaning that pristine sulfur and volume reduced TEGO are depicted after a brief mortaring process. TEGO appears as formed by wrinkly sheets. The soaking of the solvent and the mortar action clumps the material in agglomerates, but the main morphological properties observed at TEM (Figure 5-4) are confirmed. Sulfur particles can be observed decorating the TEGO surface, but after the thermal treatment (Figure 5-21. images e, f, g and h) disappears completely from the surface of the porous carbon. This effect was also observed by Xiulei

et al. [134], that described the progressive disappearance of sulfur in the carbon host, being barely visible after treatment at 145°C and being almost undetectable after treatment at 155°C, being found as the optimum for thermal infiltration. In figure 5-21, S – TEGO dT 50:50 is shown after the thermal infiltration. Also in this sample, sulfur particles are almost undetectable and the porous structure of TEGO is still observable. At lower magnitudes, it appears as a foamy, expanded structure, while at higher magnification, the exfoliated stacking of graphite can be recognized when observed in cross section.

Finally, a chemical synthetic route was explored. A well-known path was followed, in which sulfur is obtained by acidification of a sodium thiosulfate aqueous solution, resulting in the disproportionation of the salt. Elemental sulfur forms a colloid in the polar environment and is slowly adsorbed on the GO platelets present in the environment. A still unexplored route was tested, consisting in carrying out the chemical reduction of the GO in the same vessel, obtaining the decoration and reduction step in a one pot reaction. After both processes took place, the water phase appeared crystal clear, meaning that no more unbound sulfur was free in the vessel, while the rGO floated on top of the reactor, meaning that a high degree of polarity was restored in the GO. After filtration, several washing and drying the powder appears coarse and hard, difficult to mortar, shiny as small crystals. The sample was investigated by means of SEM after being mortared, in order to better understand the structure of the composite material. The coarse, hard and compact structure of the material was confirmed by the microscopy (Figure 5-23); in fact, the particles appeared agglomerated in structures with size of up to 200 µm with sharp edges. The texture of the surface of these agglomerates is jagged and porous and is studded with sulfur particles. It was decided to perform a further step in order to infiltrate the sulfur inside the bulk structure of the carbon host, then a further thermal treatment at 155 °C was performed under inert atmosphere. In Figure 5-24 the microscopy images of the same sample after the thermal annealing are reported. Obviously, the size of the agglomerates did not change, but the texture of the surface appeared different, since most of the external shell of the blocks were smooth and without sulfur particles. The jagged texture remained

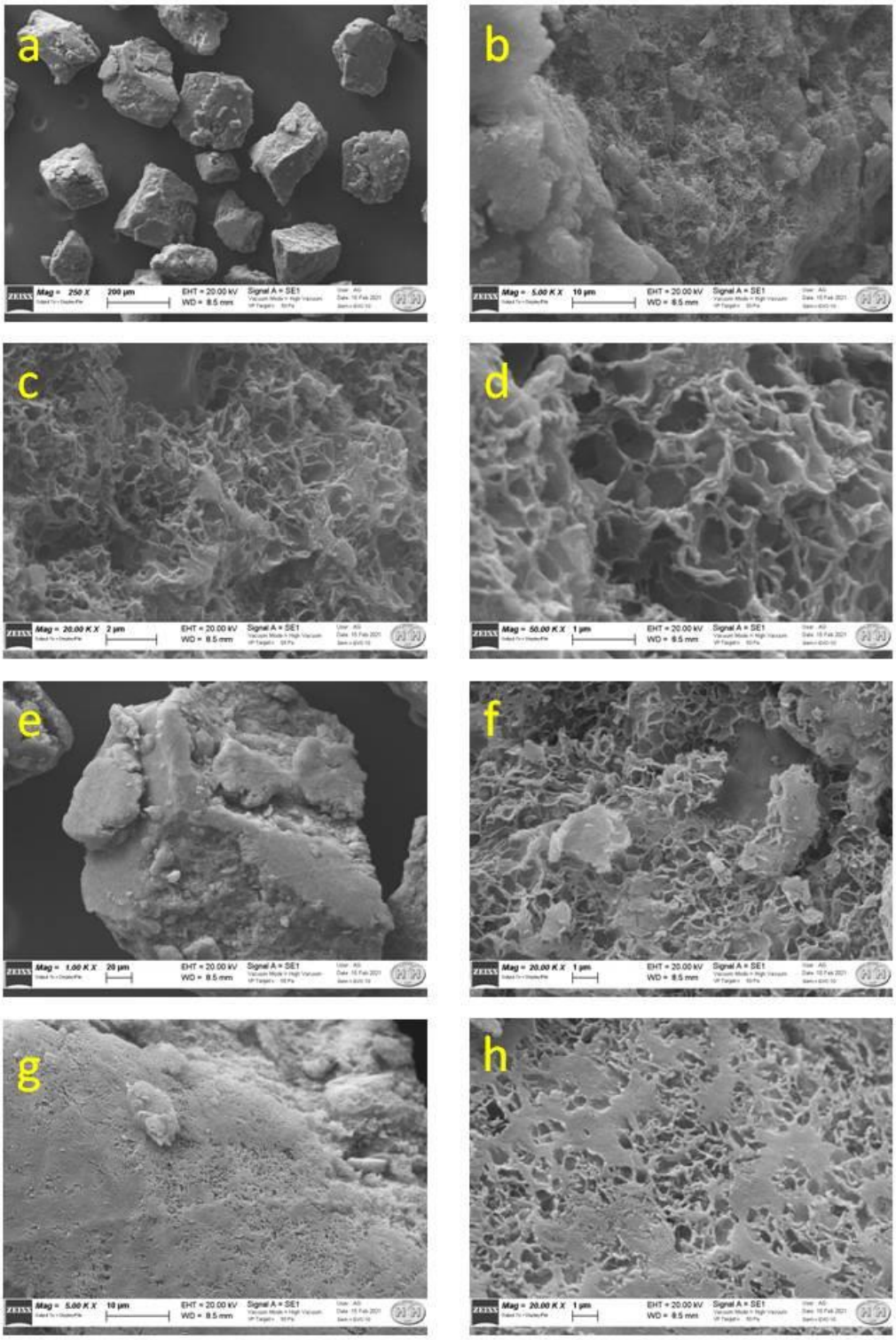

Figure 5-23 SEM images of S – LAArGO 70:30 after the chemical decoration and drying of the composite. The porous structure of the rGO can be seen and sulfur droplets decorate the surface of the coarse particles.

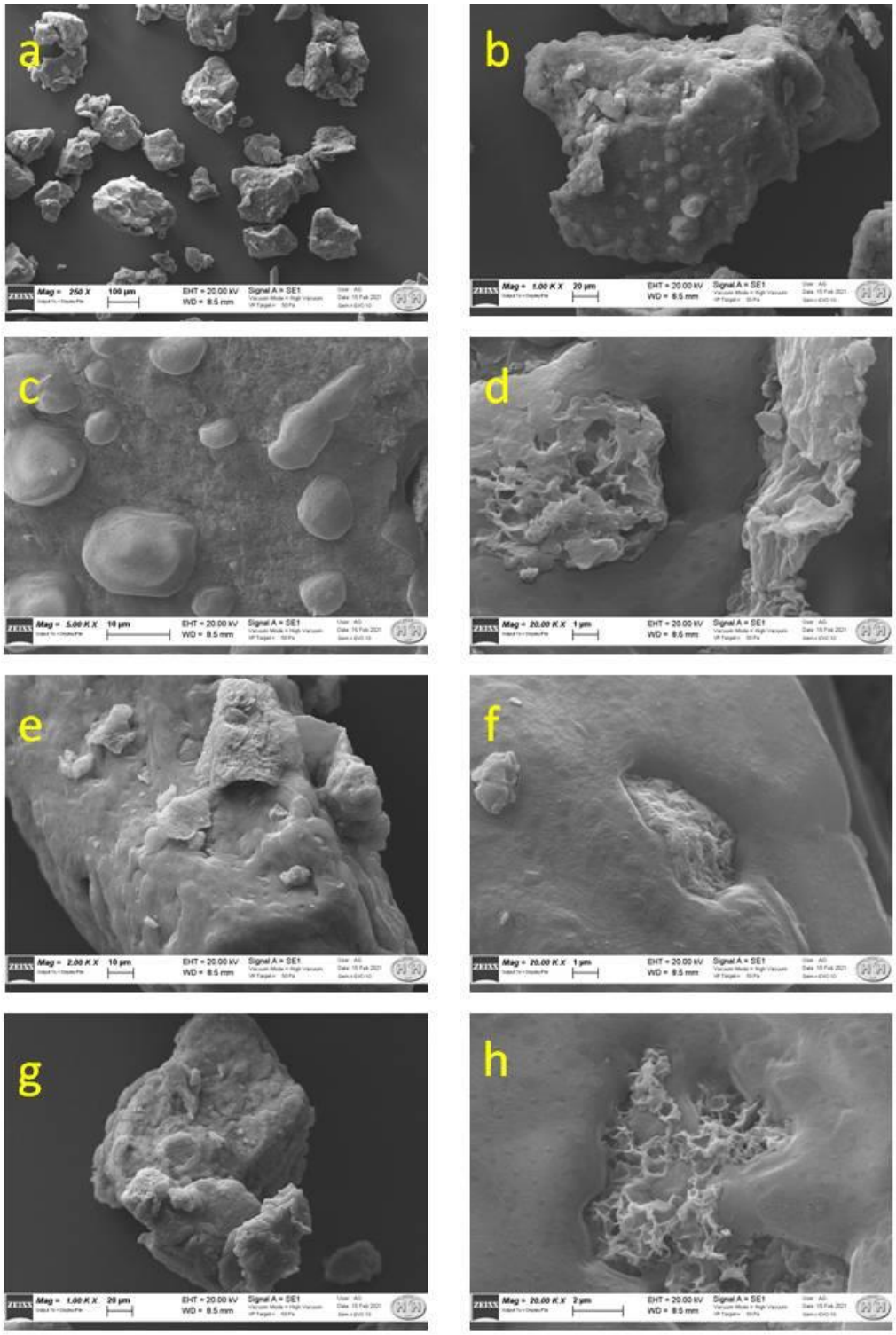

Figure 5-24 SEM images of S – LAArGO 70:30 after the thermal treatment. The annealing obtained important modifications on the material, covering most of the surface of the rGO particles in sulfur, since almost no jagged carbon is visible.

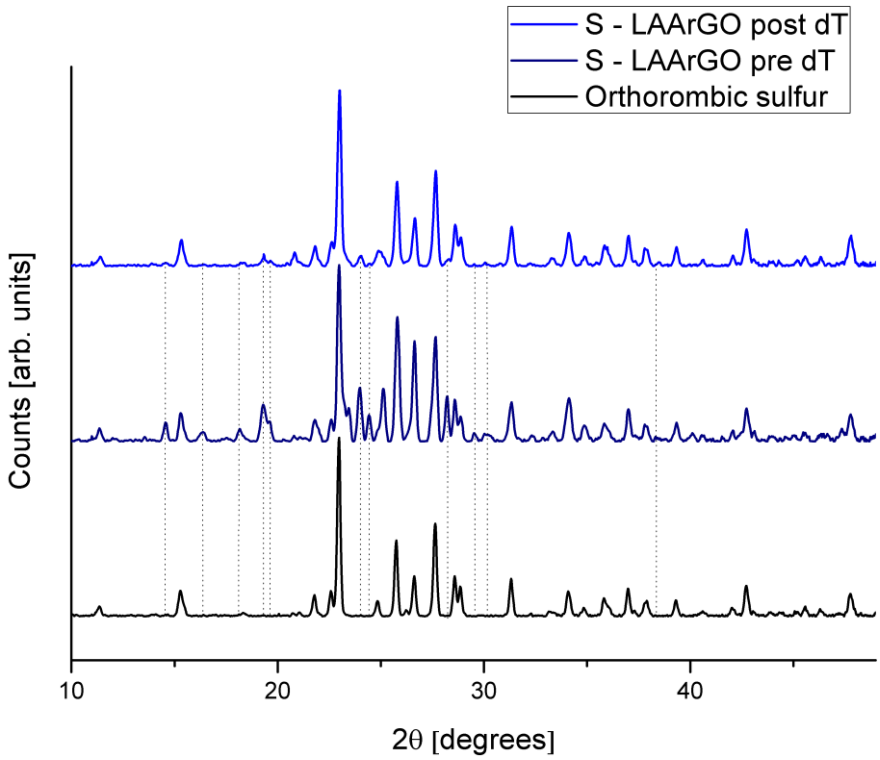

Figure 5-25 PXRD of S-LAArGO. After chemical decoration, a mix between orthorombic and monoclinic sulfur can be observed, while after the recrystallization of the electroactive material, most of the sulfur in converted in the termodinamically stable allotrope. The dotted lines highlight the peaks of the monoclinic polymorph in order to compare the three diffractograms.

visible only in some little spots (Figure 5-24, images d, f, h), while the rest of the sample was covered in a smooth cover of sulfur. This effect is probably due to the fact that the thick bulk of the LAArGO host (observable in both 5-23 and 5-24) is not as porous as the samples previously investigated (ball milled and thermally infiltrated). When studied by means of PXRD technique, an interesting fact was observed: after the chemical synthesis and the drying of the powder, carried at 50 and 60 °C respectively, sulfur displays both the orthorhombic and monoclinic structure (P21/c space group). After the thermal treatment above the melting point of sulfur, the orthorhombic fraction increased, but a small amount of sulfur maintained the monoclinic packing. The diffraction data are reported in Figure 5-25. No effects are foreseen in LIBs performance, since the crystal structure of sulfur has no impact on the cell performance. In addition, sulfur undergoes continuous melting and precipitations during the cell operations and little effect is

evidenced in the starting structure of the active material. In summary, the different syntheses lead to different materials, both structurally and microscopically. The differences are also well observable macroscopically: in Figure 5-26, 10 mg of each sample are inserted in the sockets of a Teflon sample-holder, and the differences in density are noticeable at a glance. On the left, clockwise in shown S - TEGO dT, in which the TEGO aspect is maintained, and the material appears as an expanded, fluffy carbon, and the socket cannot contain even that scarce quantity. Then, the S - TEGO BM sample can be seen; the material appears as a fine and impalpable powder, similar to powdered sugar, leaving a black trail whenever touching a minimally porous surface. Finally, S - LAArGO appears coarse and almost crystalline; the material is hard and almost shiny. Major differences are observable between the samples, and these differences will translate into different electrochemical behavior during the GCD testing.

Figure 5-26 Different appearance of sulfur-carbon composites. From left to right, clockwise: S - TEGO dT, S - TEGO BM and S - LAArGO.

5.2.2 ELECTROCHEMICAL CHARACTERIZATION OF LI/S CELLS

All the previously listed samples were tested electrochemically via GCD analysis, and the potential window was set between 3- and 1.5-volt vs Li/Li^+. The voltage window was chosen since it is a well-known standard procedure for Li/S batteries [200,201]. The same work-rest pattern was employed as in the case of TiO_2-containing LIBs, thus performing a 30-minute rest phase between each semi-cycle. Also in this case, an adjustment of the OCV of the batteries was observed after the resting phase, which was proportional to the C rate employed for the test, thus high C rates obtained more important OCV assessments. The first samples considered were blanks obtained by simple mortaring elemental sulfur and CB. It was observed that important amounts of CB were needed in order to obtain functioning devices, and just a high ratio of CB:S (50:50) produced a working device (rate/capacity diagram reported in Figure 5-27), which obtained a first discharge gravimetrical capacity of 880 mAh/g (calculated on the total sulfur mass), about 50 % of the theoretical capacity of the active material. After about 90 cycles, the reversible capacity settles at 134(3) mAh/g which is about 8 % the theoretical capacity. This result suggests that a relevant amount of active mass was irreversibly lost from the electrode, hence CB did not perform an effective filter to the polysulfide shuttle, which led to a progressive loss of reversibility of the cell, amounting at 0.7 % capacity loss per cycle, calculated in the last 10 discharges and 1.5 % per cycle when calculated from the first discharge. This sample was first compared with the TEGO-supported composite, in order to understand the eventual occurring differences between the two scaffolds. The direct comparison of mortared samples was not carried out because TEGO is impossible to mortar, given its density. According to literature, two weight ratios were tested, namely S : TEGO BM 50:50 and 70:30. The electrochemical performance of the devices are reported in Figure 5-27 and compared to the blank electrode. The electrode with 50:50

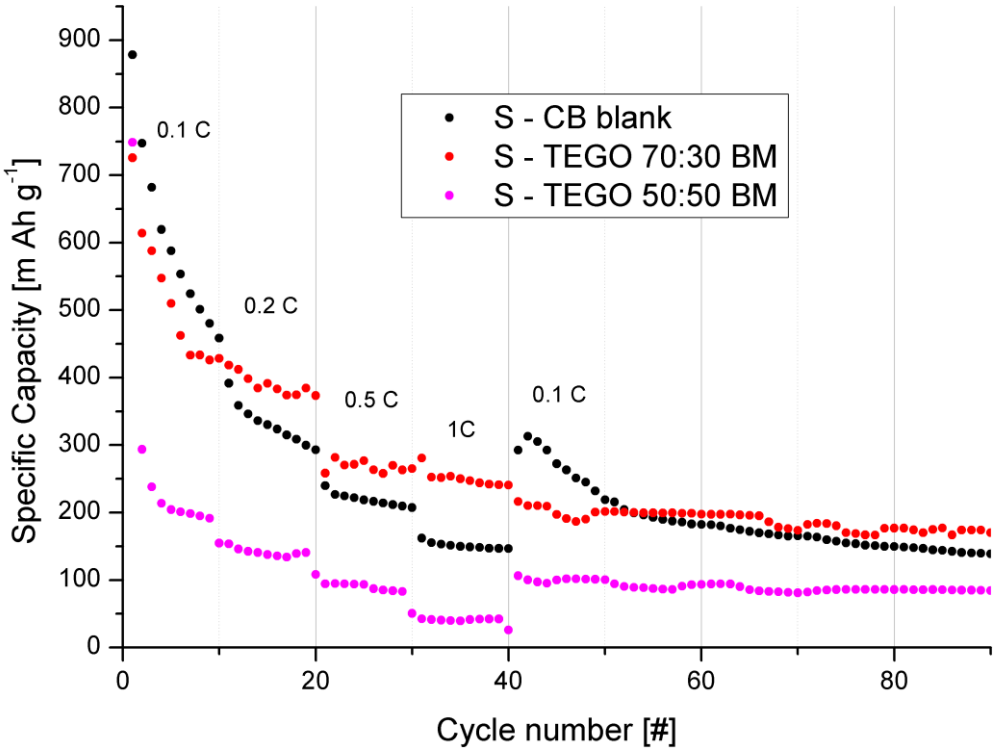

Figure 5-27 GCD analysis of different mechanically mixed S-C composites. In black, the blank sample is reported, obtained by hand mortaring S and CB. In red, S – TEGO BM 70:30, and in pink S – TEGO BM 50:50.

ratio achieved 748 mAh/g during the first discharge, but immediately sinks to about 300 mAh/g at the second cycle and the capacity loss continues for the subsequent cycles, and the trend is strengthened at higher C rates. After the different rate cycling, the reversible capacity stabilizes at C/10 with a mean value of 89(6.5) mAh/g, undergoing an attenuating capacity loss of about 0.44 %. The 70:30 sample, on the other hand, showed a first cycle capacity of 725 mAh/g, which is slightly lower than the other stoichiometry, but undergoes a less important loss of capacity, losing only 40 % of initial capacity in the first 10 cycles, while the 50:50 sample lost about 80 %. This reversibility is maintained also at higher C rates, where the sulfur-rich electrode shows an improvement of capacity, both compared to the sulfur-poor electrode and the blank. During the long-term cycling, the BM 70:30 sample showed the most interesting performance, having a mean 187(13) mAh/g capacity in the last 50 cycles, with a mean capacity loss of 0.46 %. Still the results

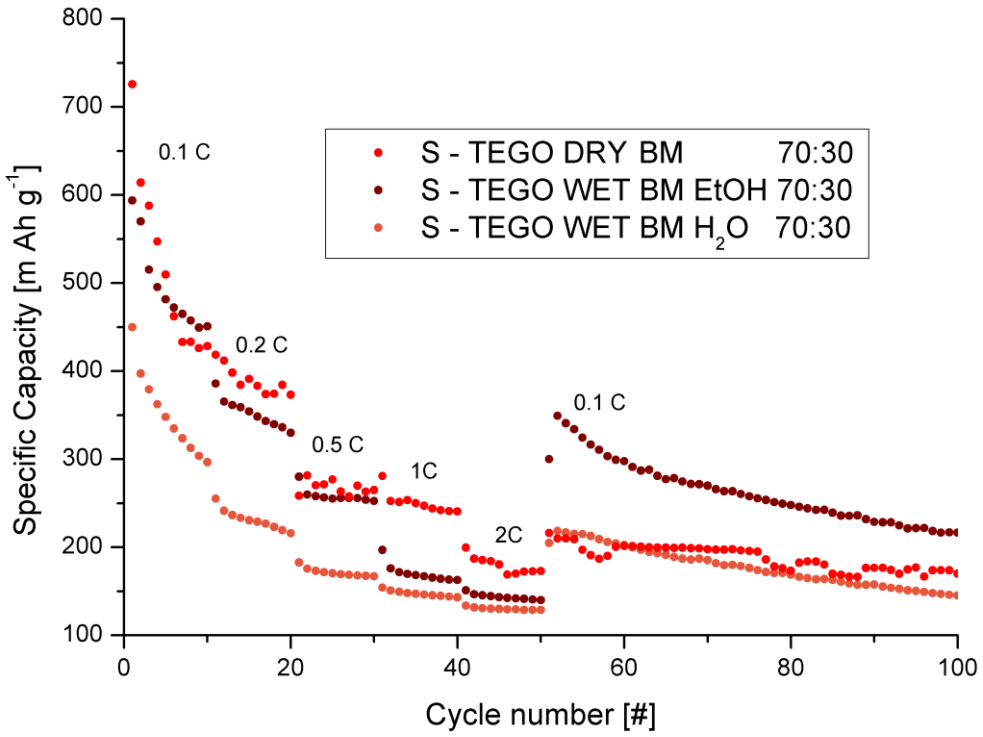

Figure 5-28 GCD analysis of S - TEGO composites with 70:30 weight ratio. In red is reported the dry milled sample. The sample milled in EtOH is indexed in wine red, while the water-milled sample is in light red.

are slightly underwhelming compared to the theoretical values of the active material, and no outstanding improvements from the blank sample were noticed. The wet ball milling route was tested, since literature reports significant differences between the milling in dry and wet environment. The S-C 70:30 weight ratio was kept constant since it showed the better results. Both the sample milled with water and with ethanol showed a similar trend in GCD despite having different absolute values. In fact, the first discharge of the sample milled in ethanol was measured as 593 mAh/g, while the sample milled in water was measured as 450 mAh/g, but both underwent a similar steady capacity fading trend unlike the dry milled sample, which showed noisier results. The sample milled in water showed the least interesting performance, while the one milled with ethanol achieved similar results to the dry milled sample. After the wearing high-rate cycles, the water processed, and the dry milled sample achieved similar results. The last 50 cycles performed at C/10

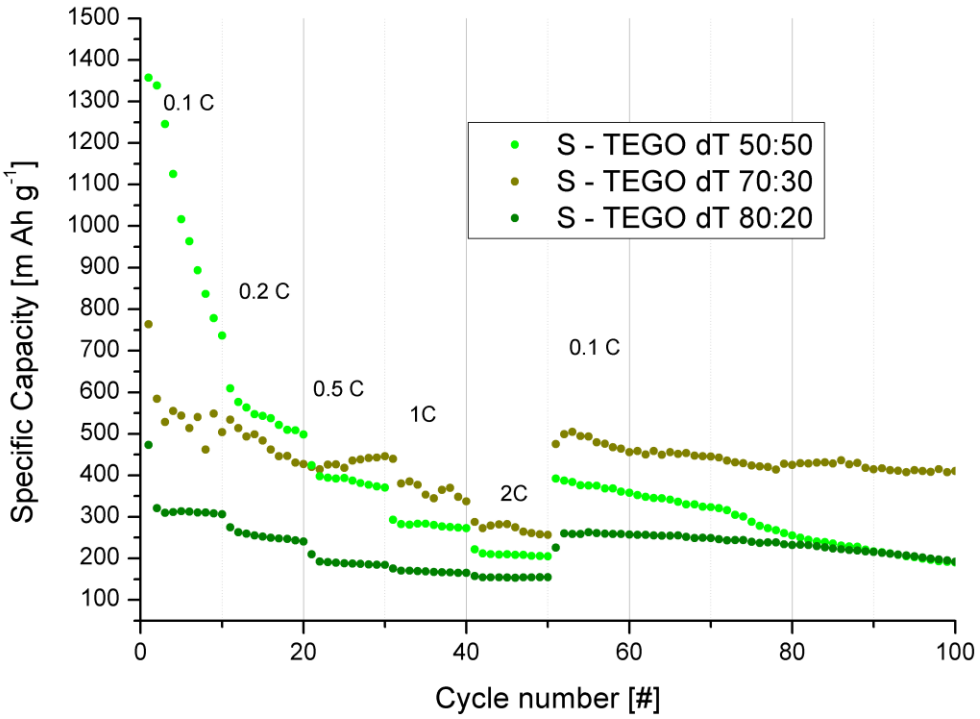

Figure 5-29 GCD analysis of S – TEGO dT composites. The samples are reported in scale of color, where the lightest green corresponds to the lowest sulfur loading, while the darkest to the higher loading.

resulted in a mean 177(22) mAh/g, with a mean capacity loss of 0.69 % per cycle. S:TEGO WET BM EtOH 70:30, on the other hand, achieved a 262(35) mAh/g capacity in the last 50 cycles, with a mean capacity fading of 0.63 % for each subsequent cycle. The sample milled in ethanol outperformed the other candidates, with the exception of the dry milled 70:30 sample for fast rates, but the overall performance of the cell did not comply the theoretical expectation, hence proving that the ball milling route is a non-efficient method to obtain S-C composites for Li/S batteries. After the ball milling method, the thermal infiltration route was investigated, and for this synthesis also the 80:20 w/w % ratio was explored. Nevertheless, this considerable sulfur loading did not result in satisfying results. In fact, as reported in Figure 5-29, the 80:20 sulfur loading achieves the least interesting performance, as it was expected, since the sulfur loading exceeds the values typically reported in literature. The first discharge specific capacity of

the 80:20 sample resulted in 473 mAh/g (28% of theoretical capacity), and immediately loses a further 30 % capacity at the second cycle. After this initial loss, the device obtains a mean 311(4) mAh/g mean specific capacity at C/10, which decreases of a 20% at C/5 rate, with a capacity of 253(10) mAh/g. After a further 20% capacity loss at C/2, the electrode does not show an important decrease between C/2 and C and between C and 2C rate, experiencing a 10 % mean capacity loss, and having a low inter-rate loss (0.39 and 0.18 % respectively). During the long-term C/10 cycling the capacity settles at a mean 192 mAh/g capacity, with a 0.62 % capacity fading per cycle. These scarce results can be due to the excessive sulfur/carbon ratio, which is known as non-optimal for Li/S batteries. Nevertheless, an interesting trend can be observed at high C rates, but the average capacities do not justify further efforts. When the ratio is pushed towards lower S loading, better performance are observed: in fact, the 70:30 ratio obtained the better results between the thermally infiltrated composites. In fact, it achieved the better high-rate capacities (mean values are 430 mAh/g at C/2, 370 mAh/g at C and 271 mAh/g at 2C) and the best capacity retention in the long-range cycling, maintaining a mean reversible capacity of 440 mAh/g in the last 50 cycles, experiencing a 0.28 % fading per cycle. This method proved to be better performing than the simple ball milling route, probably because, in this case, the porous structure of the TEGO scaffold remained pristine after the decoration by means of sulfur, while the BM samples shewed drastically different features, with an important pulverization and compression of the carbon matrix. For these reasons, this infiltration method, which employs milder conditions and no harsh mechanical synthetic steps, was found to be better performing than the mere mechanical mixing of the composite components. A further increase in the carbon content was found to be detrimental for the cell performance, probably due to the difficulty in achieving a satisfying electrode loading. The main problem was the TEGO volume that was hard to decrease sufficiently to get a high loading on an electrode. The elevated TEGO ratio hinders high mass loading per cm^2 on the electrode; in fact, the loading for the 80:20 sample was 0.43 mg/cm^2, in the 70:30 sample was 0.24 mg/cm^2 and for the 50:50 composite, a 0.11 mg/cm^2 loading was achieved. An important parameter to control in Li/S batteries is the sulfur/electrolyte ratio, since high ratios offer better performing

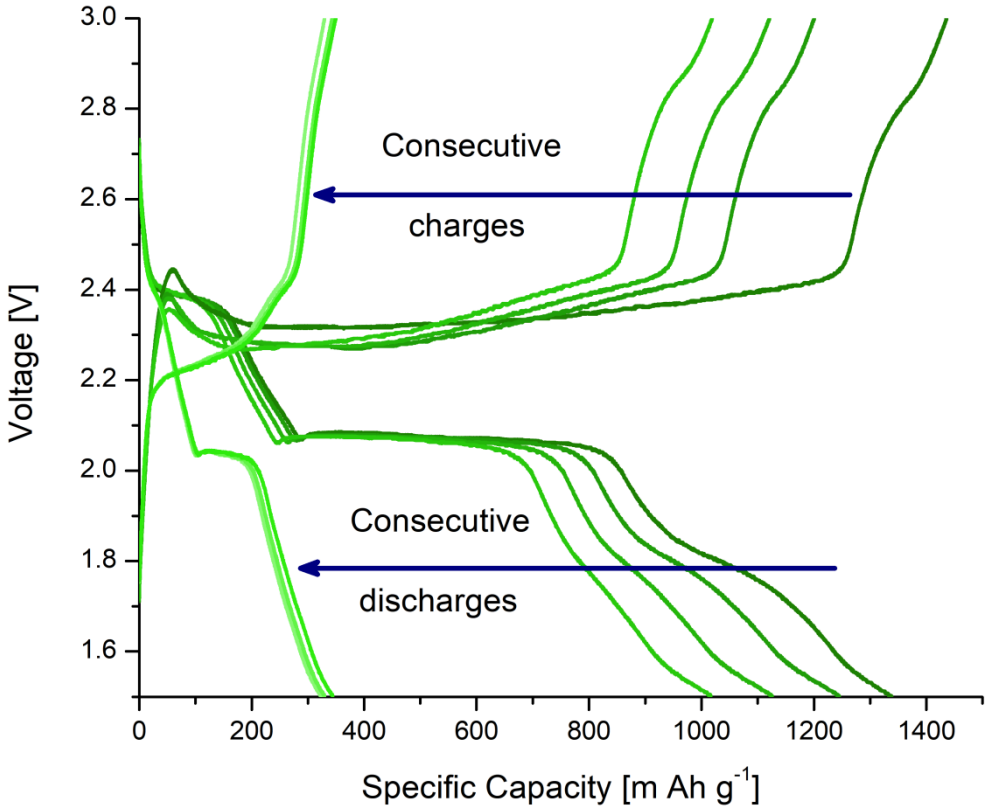

Figure 5-30 Voltage profiles during charge and discharge of S - TEGO dT 50:50 taken at C/10 at the beginning and the end of the GCD analysis. A considerable capacity loss is observed during the cycling of the device.

devices, because of the limited Kps of the polysulfides species in the electrolyte [80–82]. In this lab-scale research, about 1 ml of electrolyte was employed to properly soak the cell, leading to far from optimal sulfur to electrolyte ratio. A scarce sulfur loading results in a high polysulfide dissolution and a high-capacity fading. This was confirmed by the final S – TEGO dT 50:50 device, which showed an outstanding 1357 mAh/g first discharge specific capacity, which amounts 81 % of the theoretical capacity, but immediately experiences a capacity fade, losing 46 % of the reversible capacity within the first 10 cycles carried at 0.1C. After the first 20 cycles, the specific capacity of the 70:30 sample overtakes the 50:50, whilst the low sulfur sample steadily loses capacity during the charge/discharge cycling. After 50 cycles, when the rate was set at 0.1C, the reversible capacity is still close to 400 mAh/g, but rapidly decreases in the next cycles,

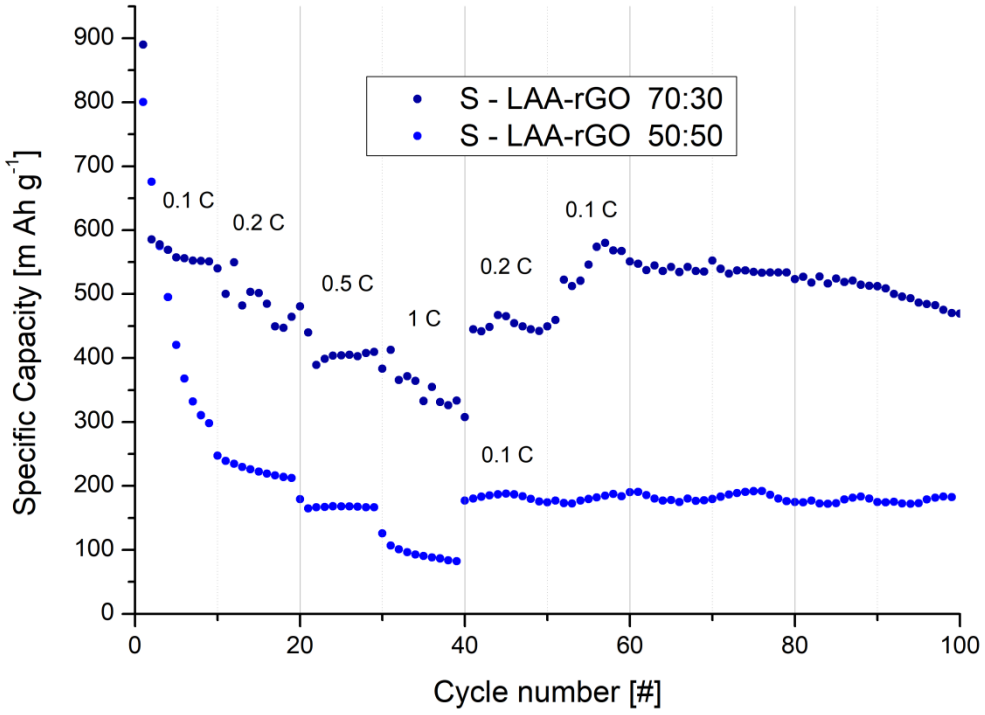

Figure 5-31 GCD of S – LAArGO composites. The 50:50 and 70:30 ratio are compared, and the different behavior at a variety of C-rates is shown.

reaching 190 mAh/g at the 100th cycle, with a mean 1.46 % capacity loss per cycle, which is an undesirable phenomenon for a secondary battery. The discharge curves are reported in Figure 5-30, where different voltage profiles at C/10 are reported, both at the beginning and at the end of the cycling analysis. A tailoring of the electrode loading and a more advanced research status, where volume and mass efficiency of the device are better employed, can limit the continuous capacity leakage. Finally, the chemical decoration route was studied. The electrochemical performance were investigated also in this case by means of GCD technique and the observed results were found to be interesting. Also in this case, the already observed optimum in S-C ratio was confirmed, since the 70 % loaded electrode obtained the better results. This can be due to the large surface area of the carbons employed in this work, since LAA-rGO was measured having a SSA of above 550 m^2/g by spectrophotometric analysis through the methylene blue adsorption method [202]. The high SSA and carbon fraction may hinder the usage of all the active material,

thus being outperformed by making the sulfur rich composites. In this case (as shown in Figure 5-31), S – LAArGO 50:50 obtained a 800 mAh/g first discharge capacity, that swiftly dropped to about 300 mAh/g after only 9 cycles. The high rates performance confirm the capacity fading trend and have mean values of 226(11) mAh/g at C/5, 172(4) mAh/g at C/2 and 102(13) mAh/g at C rate; when the rate is set at C/10 again, the capacity appears stable, with a mean 180(5) mAh/g reversible capacity, with an almost negligible mean capacity loss of 0.06 % per cycle. This unusual capacity retention is promptly confuted by the 70:30 sample, which showed the already observed capacity loss but measured the better overall performance between all the observed composites. After the initial capacity of 890 mAh/g, the observed capacities keep fading for the rest of the test, despite some ascending trends attributed to non-predictable fluctuation of the cell during the test. This descending trend is less severe than in the other observed devices and measured mean capacities of 560(14) for the first C/10 discharges (first cycle excluded), dropping at 486(30) mAh/g at C/5, 404(14) mAh/g at C/2 and 350(30) mAh/g at C rate; given the elevated irregularity during the first C/5 cycles, it was measured again as 450(9) mAh/g, thus showing less capacity but a more stable reversibility during measurement. Finally, during the last C/10 cycles, the capacity showed a steady, but not too steep fading trend (neglecting the initial rise), achieving a mean 525(25) mAh/g, with a descending trend of - 0.21 % capacity per cycle, which can be considered harsh for a state-of-the-art electrode, but is acceptable for a complex chemistry as Li/S in a research-scaled device. These interesting results identify the S – LAArGO 70:30 as the best overall candidate as electrode for Li/S batteries, being the better performing electrode and maintaining a good degree of reversibility, even after prolonged and wearing cycling. Finally, in the table below the mean performance of the tested composites are reported schematically.

Table 5-4 Recap of the mean performance at different C-rates of S-C composites

	C/5 specific cap.	C/2 specific cap.	C specific cap.	C/10 specific cap.	Cap.fading @ C/10
Blank CB	330(30)	219(10)	151(5)	178(47)	1.3
S - TEGO BM 50:50	142(7)	92(7)	42(3)	90(7)	0.4
S - TEGO BM 70:30	389(16)	268(8)	250(12)	188(14)	0.5
S - TEGO wet BM H_2O 70:30	231(12)	172(5)	147(3)	178(22)	0.7
S - TEGO wet BM EtOH 70:30	352(17)	258(8)	171(10)	263(35)	0.6
S - TEGO dT 50:50	541(35)	380(31)	275(19)	287(66)	1.5
S - TEGO dT 70:30	473(37)	431(12)	370(29)	408(26)	1.2
S - TEGO dT 80:20	253(10)	190(7)	168(3)	155(1)	0.6
S - LAArGO 50 :50	226(12)	172(4)	102(13)	180(6)	0.1
S - LAArGO 70 :30	451(9)	404(15)	350(30)	526(25)	0.2

5.3 SILICON-BASED CELLS

5.3.1 STRUCTURAL CHARACTERIZATION OF SILICON NANOPARTICLES

The disproportionation of SiO can produce a variety of silicon NPs, and in order to better understand the dependence between the treatment conditions and the size of the final product, several syntheses were carried out. In fact, it is known from literature that the reaction does not take place below 900 °C and that is almost quantitative at 1000 °C after a few hours treatment [161,203]. Four samples were produced and each of them underwent the same heating ramp of 20 °C/min treatment, but different final temperatures and dwelling times. The conditions employed were:

- 1100 °C, 2 h treatment
- 1000 °C, 2 h treatment
- 1000 °C, 1 h treatment
- 950 °C, 1 h treatment

All the products were let cool to RT and taken into an Ar-filled glove box, then PXRD was performed after sealing the powders in airtight glass capillaries. All the disproportionated samples yielded silicon NPs, with minor differences in the size of the latter. The diffractograms from which the Rietveld was performed are reported in Figure 5-32, where the SiO starting material is compared with the materials obtained after the different treatments. In the SiO diffractogram, only the amorphous contribution at $2\theta = 25°$ is noticeable. After the treatment, the amorphous contribution remains, but two different diffraction peaks attributed to silicon emerge at $2\theta = 28°$ and $2\theta = 47°$, respectively the 111 and 220 reflections. The sharpness of the diffraction reflections of silicon appears proportional to the treatment, having broader peaks for the less intense

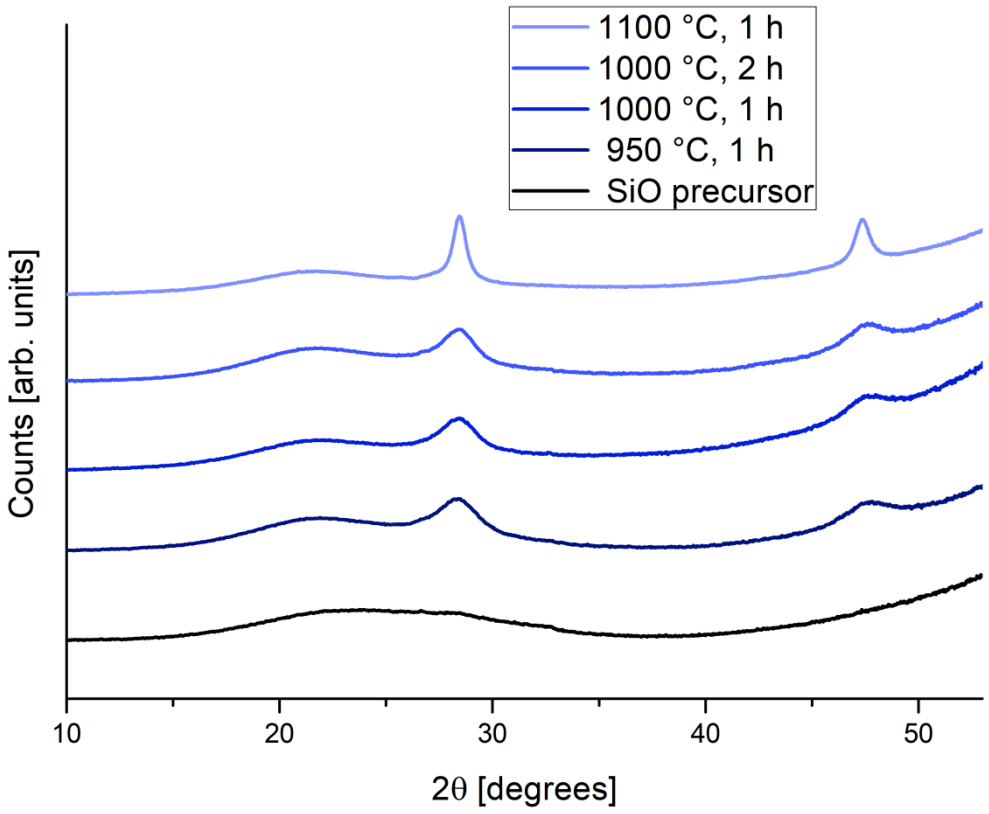

Figure 5-32 Comparison between pristine SiO (black) and the materials obtained by different disproportionation temperatures and times. The samples are ordered in a scale of blue.

treatment, while more severe conditions lead to sharper signals and bigger crystallites. After refinement, the sample treated at 950 °C showed a mean crystallite size of 4.2 nm, while the sample obtained at 1000 °C measured an average 4.7 nm when treated for 1 hour and 4.9 nm when treated for 2 hours. The mean crystallite size of the sample treated at 1100 °C for 2 hours was found to be much bigger, resulting in an average 12 nm, making them less interesting for LIBs applications, due to the known correlation between Si crystallite size and both discharge capacities and capacity retention [204]. In order to study the electrochemical behavior of Si NPs, an etching of the amorphous matrix, consisting in SiO_2 and residual SiO was attempted. The etching was performed on the sample treated at 1000 °C for 1 hour. The first try in etching the oxidized phase was performed following the experimental route reported in chapter 4.2.3.2, but at the first

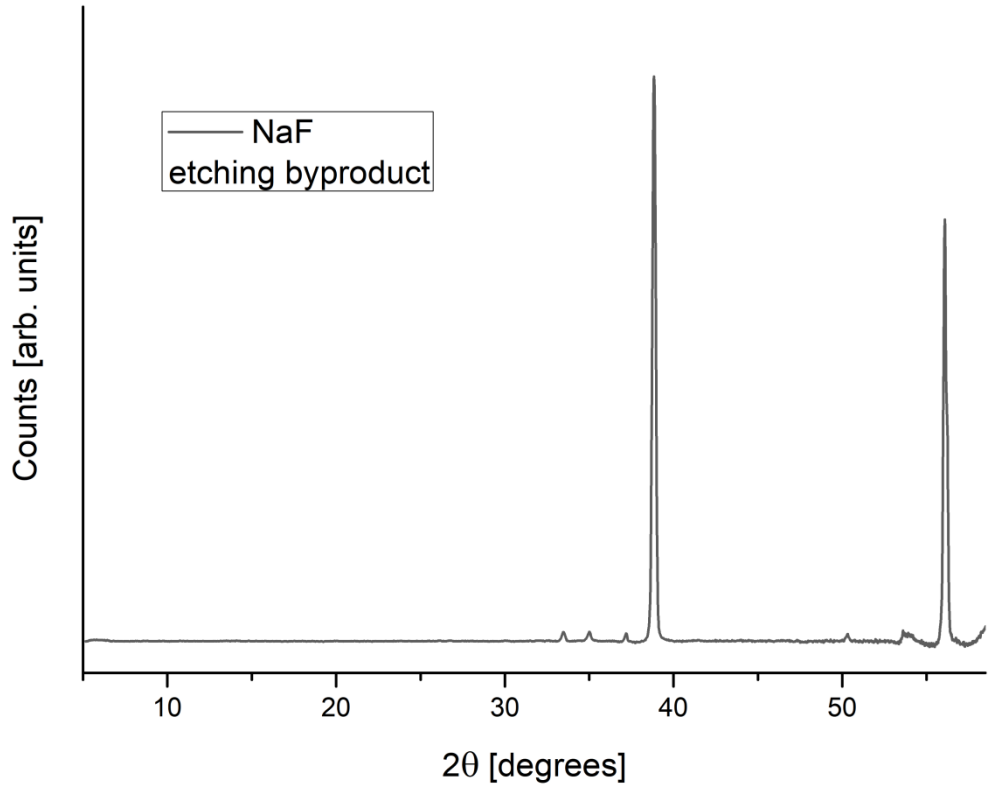

Figure 5-33 Diffraction pattern of the powder recovered from the etching process. The material was characterized as NaF, a product of the neutralization process

time an attempt in neutralizing the etching solution was tested, in order to neutralize the unreacted NH_4HF_2. To do so, a slight excess of NaOH solution was added to the reaction vessel after the separation of the organic (n-hexane) and water phase. Some bubbling was noticed while the solution heats a little during the exotermic process, and probably a little NH_3 release is observed, following reaction (24):

$$NH_4HF_2 + 2\ NaOH \rightarrow NH_3 + 2\ NaF + 2\ H_2O \qquad (24)$$

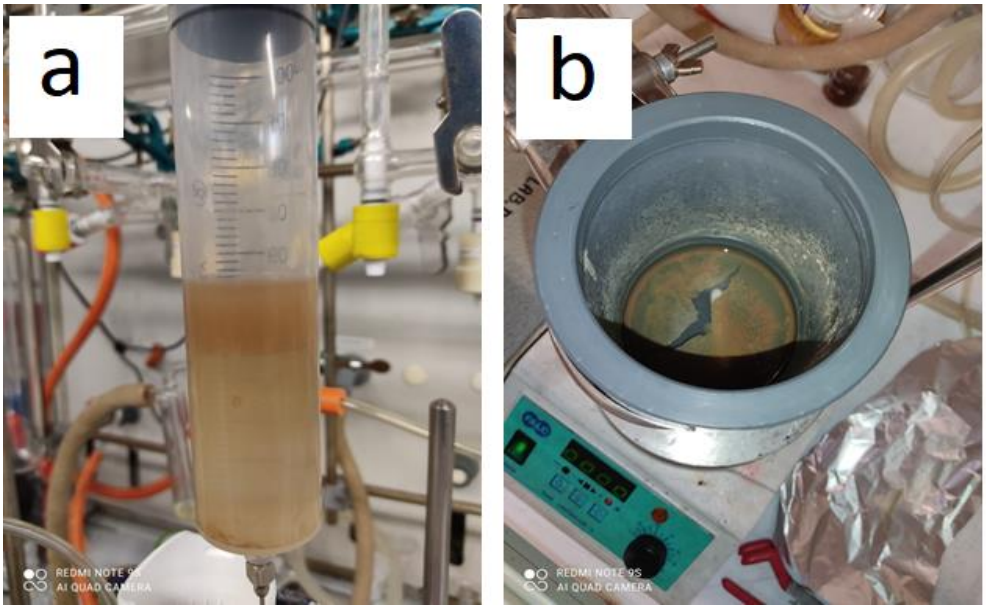

Figure 5-34 On the left, phase separation of hexane (top) and water (bottom). The solid suspension is mostly found in the organic phase. On the right, the remains of the reaction: the water phase and some leftover hexane. The red suspension is found at the upper water-organic interface, while the water is clear.

After some minutes of stirring, the organic phase was collected with the aim of a stainless-steel syringe and placed in an airtight Schlenk vial under Ar atmosphere. The n-hexane appeared crystal clear, meaning that almost no silicon was extracted from the reaction, while the water phase showed a gel-like appearance, probably because of a reaction between NaOH and SiO_2, that produce silica gel. This means that some unreacted SiO_2 remained in the reactor, probably because of some oxygen infiltration or some procedural mistakes. A small amount of the extracted solvent was dried in an oxygen-free environment and some a little powder was recovered. The powder was analyzed via PXRD (reported in Figure 5-33), and the two signals were indexed as the cubic crystal lattice of NaF, a byproduct of the neutralization of the hydrofluoric acid derivate and sodium hydroxide. Another etching process was attempted, but this time the organic solvent was removed from the vessel without prior neutralization. This time, a visible suspension was found and, as shown in Figure 5-34a, the reddish solid was mostly located in the organic (upper) phase, as seen in the syringe photo. After a little time, no solid is

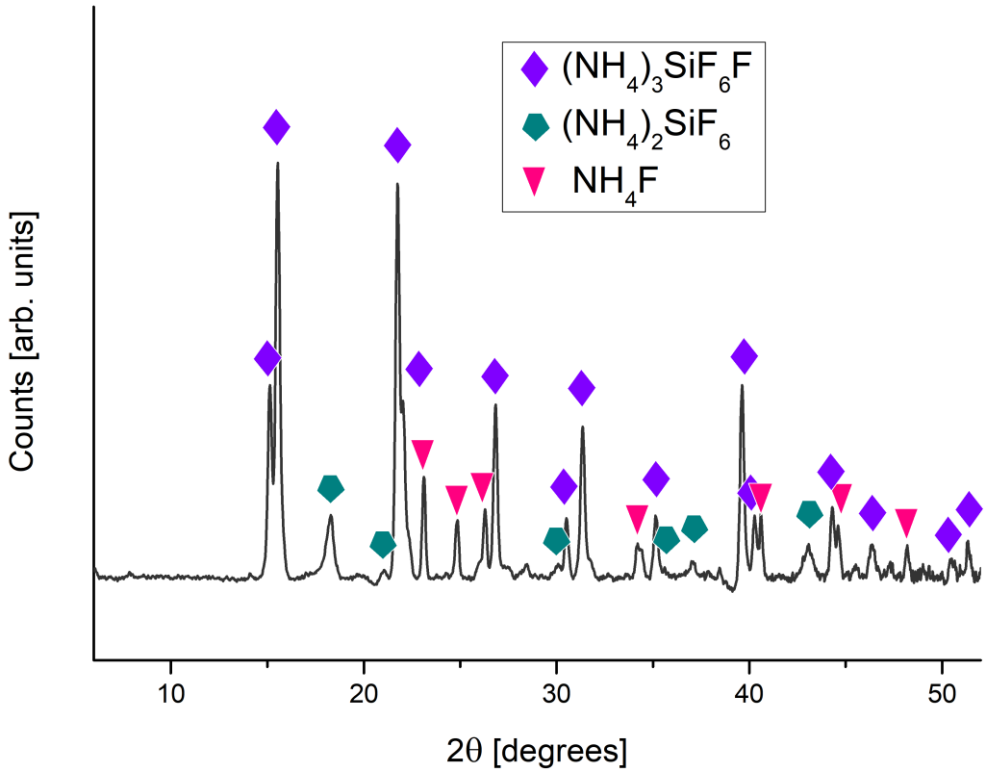

Figure 5-35 PXRD analysis of the powder mixture recovered after the etching of disproportioned SiO. Three different crystal crystalline materials were recognized, but no evidence of Si was detected.

found in the water phase, as evidenced in figure 5-34b, where it can be noted that below the water-hexane interface water appear crystal clear. Also in this case, the organic phase was transferred in a Schlenk vial under Ar atmosphere, and a small amount of material was dried in an oxygen-free environment. PXRD was performed on the powder and the diffraction pattern is reported in Figure 5-35. Three phases were identified in the powder mixture, namely triammonium silicon fluoride $(NH_4)_3SiF_6F$, $(NH_4)_2SiF_6$ and NH_4F. The peaks attributed to $(NH_4)_2SiF_6$ cubic phase have a Gaussian profile, while the peaks attributed to both $(NH_4)_3SiF_6F$ tetragonal and NH_4F hexagonal phases have a more distinct Lorentzian shape, attributed to coarser crystallites. No traces of silicon were found, unlike the reference papers, in which the silicon was successfully detected after the etching and extraction process. It was decided nonetheless to test the materials, so a comparative analysis between the synthesized Si-SiO_2 mixture with the SiO starting

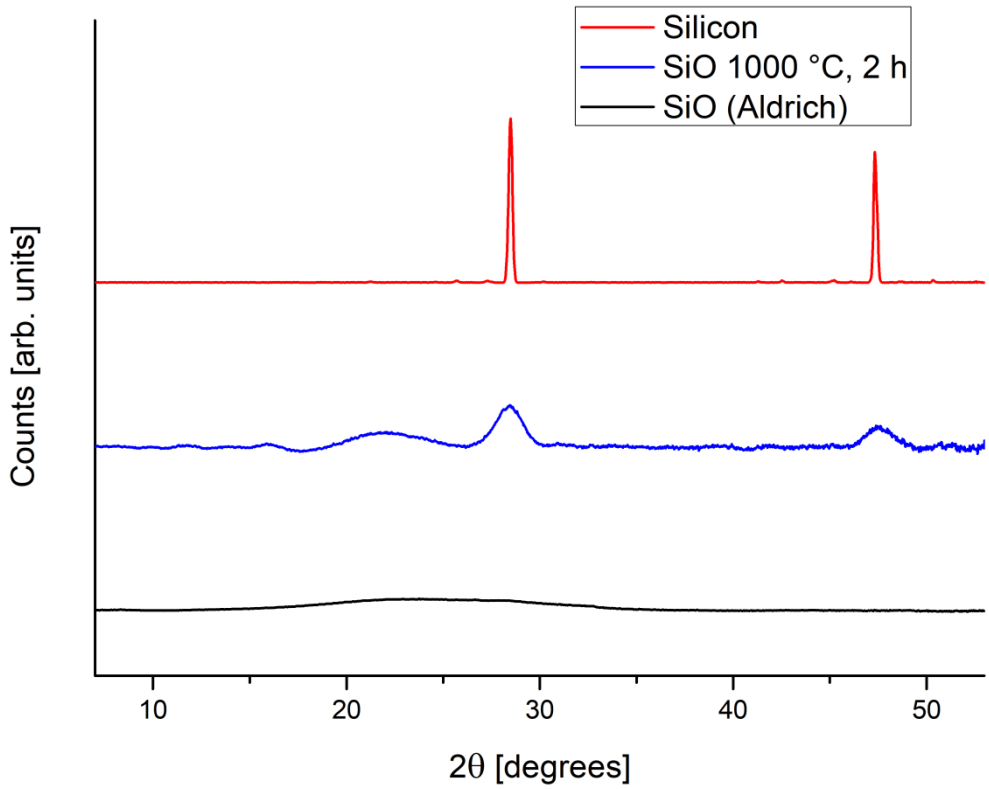

Figure 5-36 PXRD of the precursor SiO (black), the disproportionate sample (1000 °C for 2 hours, in blue) and pristine silicon microcrystals (red). These powders were tested in LIBs and compared with both CB and TEGO as a conductive additive.

material. In fact, both Si and SiO are known having electrochemical properties in LIBs, and SiO is characterized by a theoretical specific capacity of 2400 mAh/g [205]. In order to compare the performance with pure silicon, batteries were produced using Si microparticles, directly bought from Sigma- Aldrich with a ~ 325 mesh. The structural analysis of the different materials is reported in Figure 5-36, while the electrochemical comparison will be discussed in the following chapter.

5.3.2 ELECTROCHEMICAL CHARACTERIZATION OF SILICON-BASED LIBS

In order to produce working silicon-based electrodes, a generous amount of conductive carbon has to be employed, and ratios up to 1:1 silicon : CB w/w % can be found in literature [87,206]. In order to understand the minimum CB amount needed to allow a proper cyclability of the insulating silicon NPs, both 811 and 622 active material/carbon/binder ratio were tested. The preparation of the electrode materials was carried out by mortar grinding the dry powders, from which the slurry was produced. The GCD testing was carried out without employing stressful conditions, since the objective was to test the capacity retention over a high number of cycles of the silicon-based anodes. In fact, the greatest hindrance to the employment of silicon anodes are the degrading effects listed in chapter 2.3.2, hence several C/20 cycles were conducted in order to observe the fading capacity caused by intrinsic process, not caused by severe conditions. The cycles were performed between 2 and 0.05 V (vs. Li/Li^+), since almost no capacity is expressed above 2 V and most of the discharge plateau of silicon is located below 0.4 V, but below 0.05 V lithium plating starts developing. For this reason, this value is used as the lower limit. The first tested samples were based on SiO, which was the starting material to obtain Si NPs. It is the least performing material, since it has the lowest theoretical capacity between the analyzed silicon-based anodes and it is known as a troublesome material, characterized by an immediate capacity loss in the first cycles. It is also known as having relatively low reversible capacity after stabilization, making it the ideal first candidate to be considered, in order to have a blank comparison for the other samples. A SiO-CB-PAA 811 electrode was produced and characterized, and the electrochemical performance are reported in Figure 5-37. The first discharges achieves less than half the theoretical specific capacity of the active material (933 mAh/g), and within the first 10 cycles fades rapidly below 500 mAh/g, despite the stressless cycling conditions. At the end of the cycling, the specific capacity reaches 100 mAh/g, 11 % of

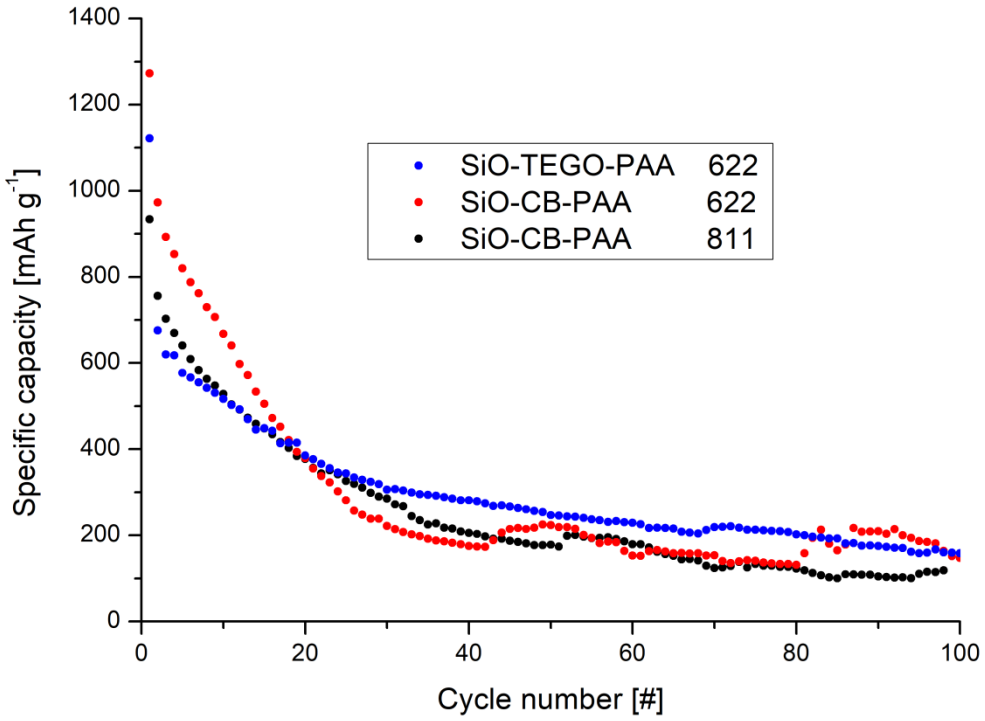

Figure 5-37 Comparison between GCD performance of SiO electrodes prepared with different active material to carbon ratios

the initial capacity, this fact being a known problem related to this family of electroactive materials. In the last 20 cycles, a mean 110(7.4) mAh/g is achieved, which is not an impressive result. To improve the performance, a higher CB and binder ratio was tested, setting the proportion to SiO-CB-PAA to 622. The addition of both CB and binder was proven as being beneficial, increasing the first discharge to 1272 mAh/g, which is anyway halved after 10 cycles at C/20 (640 mAh/g) and almost halved again at the 20th cycle (379 mAh/g). It has to be highlighted that in the middle of the testing (from cycle 20 to cycle 80), the performance of 622 SiO electrode are comparable to the 811, probably because the harnessing of electroactive material at the beginning of the cycling, but when the anode starts being pulverized, the performance appear similar. During the last discharges, probably due to fresh material being exposed because of the fragmentation of SiO, the capacities slightly improve passing from a mean specific capacity of 154(14)

mAhg (cycle 60th to 80th) to a capacity of 185(28) mAh/g. These unforeseeable mechanisms make the behavior of the device unpredictable and are not desirable. The SiO powder was at this point mixed with TEGO instead of CB to test the differences. The carbon content was kept at 20 % (622 ratio) since it was proven as most beneficial for the electrochemical performance. The specific capacity discharge trend is included in Figure 5-37, and it can be noted that during the first cycles, the TEGO addition did not lead to an improvement, since the capacities of the electrode with 20 % CB outperform the TEGO electrode for the first 20 cycles. After this initial stage, TEGO was proven beneficial because the capacities underwent a less drastic decay, experiencing a lower fade per cycle respect to the CB electrodes. The improved capacities can also be attributed to the TEGO contribution, which is known to be approximatively 200 mAh/g after the very first discharges (which can measure up to 2000 mAh/g [207]). The other beneficial effect of the TEGO addition is the more stable electrode potential upon cycling, meaning that the electrode had no severe fluctuations during the long (several weeks) measure. In fact, the reversible capacity in the last cycles is almost comparable to the one of SiO-CB-PAA 622 electrode, but the standard deviation is almost halved, being 181(14) mAh/g. For this reason, TEGO was proven a good candidate to support SiO particles in LIBs, given the stability it provides to the anode and the improved performance. The same test was then carried out with Si microparticles (Sigma-Aldrich, 325 mesh). The active material was used as received, without further treatment. The same experimental conditions as SiO electrodes were maintained for this material, meaning that the three different electrode composition (CB 811 and 622 and TEGO 622) were prepared and tested. Similar results as for SiO are observed, since the carbon and binder content are related to an improvement of mean capacities, meaning that just 10 % w/w of both carbon and PAA is not ideal for designing a silicon-based anode. In this case, both CB-based anodes (811 and 622) achieve a first discharge capacity of more than 2000 mAh/g (2389 and 2264 respectively), but the capacity rapidly fades. In the 811 sample, capacity drops to 168 mAh/g within the 10th cycle, and the last reaches a stabilization after about 15 cycles; the reversible capacity of the last 50 cycles is of 90(4) mAh/g, which is about 4 % of the initial capacity. Same goes for the 622 electrodes, but these detrimental processes occur in a less severe kinetic.

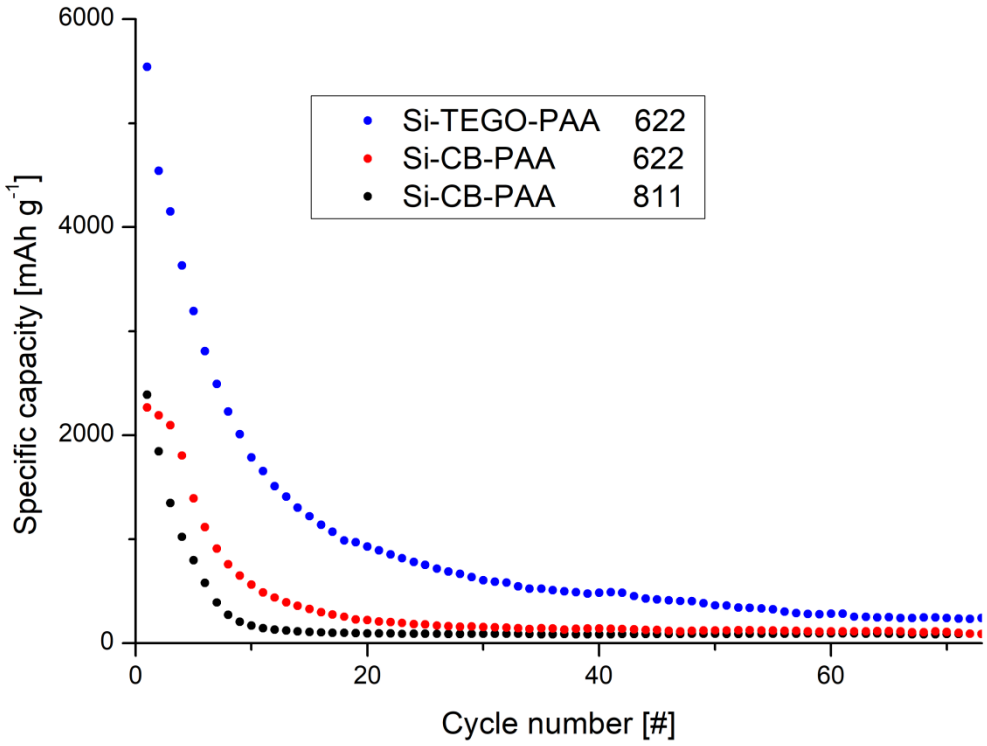

Figure 5-38 Comparison between GCD performance of Si microparticles-based electrodes prepared with different active material to carbon ratios

In fact, after 10 cycles the electrode retains ¼ of its starting capacity after 10 cycles and reaches stabilization after 30 cycles. In the last 50 discharges, the 622 electrode maintains a mean 106(8.7) mAh/g capacity, which is close to 5 % of the initial capacity. These huge losses can be attributed to the degradation mechanisms explained in section 2.3.2 and to the size of the silicon particles which are not ideal to be employed in LIBs. The test with TEGO as a conductive agent achieved clearly better results, starting from the first discharge capacity of 5540 mAh/g, which is even higher than silicon theoretical capacity: in fact, since the operating voltage window reaches 0.05 V vs Li/Li^+, also the lithiation of TEGO takes place, and the specific capacity is normalized to the silicon weight, thus exceeding the theoretical values. TEGO capacity swiftly fades to values of 200 mAh/g after the initial cycles in which a huge SEI is formed [207], hence most of the capacity expressed by the electrode after the first cycles can be mainly attributed to silicon. Despite

the huge first discharge capacity, the performance quickly decrease reaching 1/3 of the initial capacity at the 10th cycle and 1/6 at the 20th which is still above 900 mAh/g. After the first exponential decrease observed during the first 20 cycles, the capacity fade becomes almost linear, and in the last 20 cycles the device undergoes a capacity loss of about 1.6 % per cycle, and the capacity does not reach an equilibrium even after 70 cycles, but the values are more than double than CB-based anodes. This can be explained thanks to the beneficial effect of TEGO in these systems, thanks to its high SSA that can prevent the Si fragments dispersion in the cell and also contributes to the overall capacity of the system, even if marginally. Lastly, the disproportionated SiO electrodes were prepared and characterized via GCD as the previously investigated electroactive materials, in order to investigate the behavior of the synthesized NPs. Only the silicon fraction of the material was considered as active material, consisting of about 32 % of the silicon and silicon-oxides mixture, considering a quantitative disproportionation of the starting silicon monoxide and excluding any oxygen contamination. In this case, the Si crystallite size is more appropriate for the employment in LIBs, and the effect is observable in Figure 5-39, where the comparison between the electrodes produced with different formulations of active material:carbon is reported. As in the previous samples, the first data presented is the disproportionated SiO combined in a slurry along with 10 % PAA and 10 % CB. In this case the 811 ratio outperforms the electrodes prepared with both SiO and Si as active material, gaining an impressive 3500 mAh/g as a first discharge specific capacity. The capacity fading trend is maintained, and the capacity halved within the first 4 cycles and drops below 1000 mAh/g after 13. After this initial plummet, the capacities stabilized and underwent a stable fading of the performance, with a mean capacity loss of 3.7 % loss per cycle, until the capacities are in the 100 mAh/g range. Also in this case it was proven that the 811 ratio was not sufficient to ensure a proper and stable cycling of the device, whilst some positive contribution of the disproportionated SiO was observed. In fact, the 811 ratio achieved a 2390 mAh first discharge specific capacity with the Si and 930 mAh/g with SiO. After prolonged cycling, all the samples capacity faded around 100 mAh/g, meaning 10 % CB and PAA were not sufficient to prevent the problems that affect silicon-related chemistries, listed in chapter 2.3.2. The performance significantly improve when

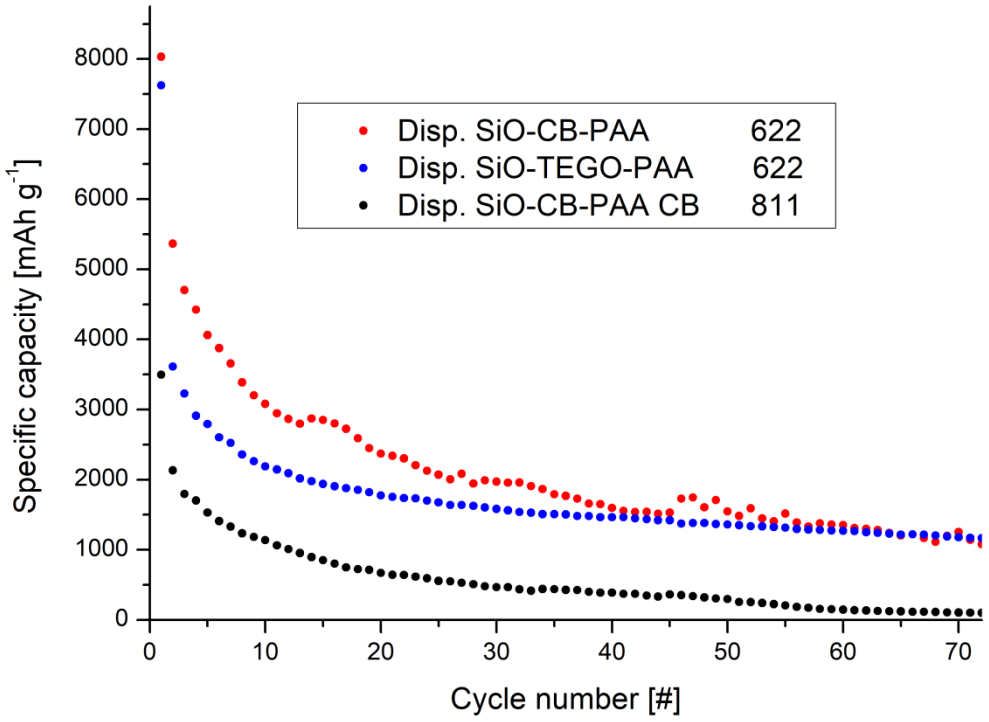

5-39 Comparison between GCD performance of disproportionated SiO NPs based electrodes prepared with different active material to carbon ratios

a more suitable CB and PAA (622) content were employed in the electrode formulation. The first discharge capacity of the 622-ratio resulted above 8000 mAh/g, which is more than 2 times the capacity registered with the 811 ratio, but also in this case the capacities quickly fade, reaching 4000 mAh/g at the 5th cycle and 2000 mAh/g at the 25th. Also in this case, the capacity is above the theoretical values because of the important SEI formed by TEGO during the very first cycles, which then can be found responsible for no more than 40 mAh/g of the overall capacity, given the amount of TEGO employed for the electrode fabrication. The following capacity fade was observed as being of a mean 1.2 % per cycle, resulting in a further halving of the capacities after about 50 cycles, reaching 1000 mAh/g at the 72nd cycle. It can be noticed that the capacity/cycle number plot appears noisy and with several spikes. This means that not all the active material is available during the first cycles, probably due to the SiO_2 still present in the sample (about 70 % in mass if the disproportionation reaction is considered quantitative) that can cause

a hurdle to the harnessing of the Si NPs, which become more and more available after some cycling, probably due to continuous cracking of the particles. Finally, the electrode prepared with 20 wt % of TEGO is reported (blue in Figure 5-39). This sample show similarities with the 622 sample produced with CB, starting from the initial capacity, which also scored an impressive 7625 mAh/g, which is above the silicon theoretical capacity. For this sample the fading was faster than in the 622 CB sample, and at the 2nd cycle the electrode already almost halved its specific capacity, dropping at 3900 mAh/g. The capacity underwent a fading of about 3.9 % per cycle, reaching 2000 mAh/g at the 18th cycle. Afterwards, the loss mitigates and reaches a mean 0.8 % loss per cycle, reaching 1007 mAh/g at the 100th cycles, which is not reported because the sample with 20 % CB stopped working after 72 cycles. The sample produced with TEGO as a scaffold achieved lower capacities at the beginning, but the descending trend was less steep and the capacities did not show significant noise, meaning that no unpredictable events took place in the electrode except the expected capacity decrease. This comparison suggests that the disproportionation of silicon monoxide can achieve NPs that are very promising for the employment in LIBs, but the etching step has to be improved because SiO_2 has a negative impact on the energy density of the device, since it adds weight to the cell. But despite being weight inefficient, silicon dioxide plays a minor role inside a battery, especially at the very first cycles, and this is what causes the high first cycle capacities, which widely exceed the Si theoretical capacities. In fact, silicon oxides can undergo the following electrochemically driven reactions:

$$SiO_x + xLi \rightarrow (1 - 0.25x)Si + 0.25xLi_4SiO_4 \quad (25)$$

$$SiO_x + 0.4xLi \rightarrow (1 - 0.4x)Si + 0.2xLi_2Si_2O_5 \quad (26)$$

$$SiO_x + 2xLi \rightarrow Si + x\,Li_2O \quad (27)$$

From these reactions it can be understood that silicon oxides can generate different secondary reactions that consume Li and do not generate reversible byproducts, except

for Equation 26 that generates elemental silicon by single replacement at the cost of lithium. This effect can be good when considering experimental half cells which operate with pure lithium as a counter electrode, but become detrimental if applied in a full cell, where the electrode balance has to be pushed towards the cathode material to buffer these losses of lithium, making the use of a high-capacity vs weight electrode vain, because of the notoriously low specific capacities of cathode materials.

6 CONCLUSIONS

In this thesis, the role of carbon nanostructured materials in novel LIB chemistries was explored. Specifically, graphene-based materials were employed as technological additives in order to overcome the typical hurdles that oppose the good functioning and thus the wide commercialization of the examined chemistries. A graphene-based material obtained by the thermal exfoliation of graphite oxide was widely investigated for this purpose, since its physical and chemical properties and scalable synthesis indicated it as a promising candidate. The systems studied included LIBs based on titanium dioxide, sulfur and silicon. In each of these chemistries carbon nanostructured materials introduced improvements in the performance of the devices. Herein is summarized a brief compendium of the work carried out along with the conclusions and a comment on the future perspectives of the work. The themes will be presented maintaining the order observed during the whole discussion of the thesis, starting from the TiO_2-containing LIBs.

Regarding TiO_2-based electrodes, the performance of graphene-supported TiO_2 electrodes in lithium-ion batteries was investigated. Two different synthetic approaches for the decoration of thermally exfoliated graphene flakes with TiO_2 nanoparticles were proposed. We compared a novel chemical route operating in hydrothermal mild conditions with a physical solid-state approach via high energy ball-milling of the precursors. The synthesized materials were analysed via X-ray diffraction and HR-TEM, and the electrodes were tested electrochemically. operando synchrotron diffraction was conducted on modified coin cell to investigate phase transitions in the electrode materials. From this investigation it was observed:

- The presence of graphene in the reaction vessel improved the selectivity of the synthesis, obtaining a higher ratio of the anatase instead of the brookite polymorph byproduct, passing from 87 % to 91.5 % anatase content.

- The presence of graphene catalysed the formation of smaller crystallites, passing from an average 15 nm crystallite size when the reaction is conducted without carbon to a mean 9 nm crystallite size.
- The electrochemical performance highlighted a significant beneficial effect even for small amounts of graphene both at low and high C rates.
- Improvements in capacity, reversibility, and high-rate stability were observed. In particular, the sample containing 1 wt % of graphene is characterized by a reversible capacity of more than 180 mAh/g rate after prolonged and wearing cycling. This result outperforms by 327% the reversible capacity of bare TiO_2 electrode.
- The sample synthesized with high (20 wt %) graphene content granted good performance at high C rates, obtaining about 30 mAh/g capacity at 30C rate, while pure TiO_2 showed close to 0 capacity.
- TiO_2 and graphene mechanically mixed showed intermediate performance.
- The structural analysis of TiO_2 was monitored by operando synchrotron light diffraction, and a high degree of reversibility of the system was observed.

This work showed a significative improvement of the performance of bare TiO_2 by impregnation of the graphene scaffold during the synthetic step. Future steps may improve the fine tuning of the graphene content in the electrode formulation, and the optimization of the synthetic procedure of TiO_2 nanoparticles, in order to obtain smaller crystallites with a positive effect on the overall cell performance. These progresses offer a novel point of view in the production of TiO_2 nanoparticles, which can be also employed for other systems and close the gap for a successful widening of the commercialization of TiO_2-based LIBs. In addition, this study can be employed for lithium titanate batteries with minor optimizations.

Regarding Li/S batteries, three different synthetic routes were tested to achieve the combination of sulfur and graphene. First, simple ball milling between sulfur and graphene was tested, then thermal infiltration of the active material was carried out and

finally a single-step graphene oxide reduction and sulfur precipitation was explored. The effectiveness of the synthesis was confirmed by powder X-ray diffraction and the morphology of the samples was investigated by SEM. For each synthetic route, different weight ratios between sulfur and carbon were explored. From the results observed, it can be concluded that:

- The ball milling of sulphur along with graphene produced a fine powder, almost impalpable. The devices prepared with this material produced batteries that after several cycling achieved a reversible capacity that is about 1/10 of the theoretical capacity of sulphur.
- The best result obtained by ball milling was reached with the sample obtained by wet milling of sulphur and graphene using ethanol as a wetting agent. The capacities were 70 % above the other best milled samples, thus a beneficial effect of wet environment is noticed.
- An important improvement is observed with the samples produced by thermal infiltration of sulphur in the graphene porous structure, which achieved a material with high apparent volume and difficult to handle.
- The thermally infiltrated sample with a 50:50 S:C ratio obtained a first discharge capacity in the sample of 1357 mAh/g, but it quickly faded, obtaining a mean 286 mAh/g at C/10. With higher loading of sulphur (70 %), the capacity stabilized at more than 400 mAh/g at C/10.
- The best overall results were observed with the chemical decoration route, from which hard agglomerates were obtained. The sample with 70 % sulphur loading achieved a mean 525 mAh/g after prolonged cycling, with a capacity loss per cycle of about 0.2 %.

During this systematic study, it was observed that 70 wt % loading of sulfur proved as the optimum for all the synthetic strategies tested. This can be attributed to the sulfur to electrolyte ratio, that is an important parameter to take in consideration that was not tightly controlled in these experiments. Strict control of the electrolyte used in these

devices can grant a less severe capacity loss of the electrodes and allow the optimization of electrode formulation with lower sulfur loading. It was noted that the chemical decoration of GO was the best performing strategy, and it can be applied to several types of GOs, in order to compare other potential interesting scaffolds. Finally, chemically modified scaffolds can improve the anchoring of polysulfides thus improving the overall performance of the cell and is a route that can lead to interesting results.

Finally, the conclusions about silicon-based batteries are reported. In this part of the work, a cheap and scalable method to obtain silicon nanoparticles was explored and optimized to reach a mean crystallite size of 4.2 nm, measured by powder X-ray diffraction. This factor is crucial to overcome the problems related to the expansion and shrinkage of silicon upon intercalation/deintercalation of lithium ions. The synthesis led to the formation of silicon nanodomains in a silicon dioxide matrix that had to be etched to obtain pure silicon. Problems during the etching phase were experienced, probably due to oxygen leakage in the system. It was decided to test the reaction intermediate along with the SiO precursor and Si from Aldrich as comparisons. It was noted that:

- The 811 active material to binder to conductive carbon ratio was not sufficient for the proper cyclability of the silicon-based batteries. This causes a loss in energy density of the system, but it appears daunting to produce working batteries with less additives.
- The addition of 20 % of conductive carbon and binder showed substantial improvements in both first discharge capacities and long-term reliability.
- Generally, graphene allowed to obtain better results in terms of robustness of the device (less noise during prolonged cycling) and the capacities of the device in the long term, retaining a higher percentage of the initial capacity.
- Disproportionated SiO produces nanocrystals in the range of 4 to 5 nm and was proven as an optimal candidate for the formulation of silicon-based electrodes.

A still unresolved issue of this chapter is the selective etching of silicon dioxide matrix surrounding the silicon nanoparticles. It could be feasible to design a more robust airtight

reactor or directly employing hydrofluoric acid as some literature suggests. Once the oxide part is removed, the performance should arise and the bare silicon nanoparticles could be easily functionalized (chemically or physically) in order to be employed for a finer and tailored embedding or wrapping with the scaffold, or even chemically bound to the conductive carbon by covalent grafting.

The overall conclusion is that graphene based materials can be successfully employed as conductive scaffolds for electroactive materials in lithium-ion batteries; in particular:

- The graphene-based materials studied in this work, which are produced via scalable top-down syntheses, can effectively improve the performance of LIBs based on novel chemistries
- Many different approaches can be followed to create graphene-active material composites. Each chemistry needs a tailored optimization of both the electrode formulation and the synthetic process to obtain the better results.
- Graphene was proven a good candidate for improving the electrical properties of electrodes and, in the case of TiO_2-containing LIBs, for the direct synthesis of nanoparticles on its surface, granting smaller crystallites with an enhanced selectivity towards the desired polymorph.

BIBLIOGRAPHY

[1] Energy Agency I. Review 2021 Assessing the effects of economic recoveries on global energy demand and CO 2 emissions in 2021 Global Energy 2021.

[2] BP Statistical Review of World Energy & Ember. Electricity production by source, World. Our World Data 2021.

[3] for Climate Change IGP. Summary for Policymakers — Global Warming of 1.5 °C. Aromar Revi 2018:32.

[4] Fraunhofer Institute for Solar Energy Systems. The Energy Charts: Online Data Platform n.d.

[5] GL S. Battery technologies for large-scale stationary energy storage. Annu Rev Chem Biomol Eng 2011;2:503–27. https://doi.org/10.1146/ANNUREV-CHEMBIOENG-061010-114116.

[6] Dunn B, Kamath H, Tarascon JM. Electrical energy storage for the grid: A battery of choices. Science (80-) 2011;334:928–35. https://doi.org/10.1126/SCIENCE.1212741.

[7] Gür TM. Review of electrical energy storage technologies, materials and systems: Challenges and prospects for large-scale grid storage. Energy Environ Sci 2018;11:2696–767. https://doi.org/10.1039/c8ee01419a.

[8] BloombergNEF. Battery Pack Prices Cited Below $100/kWh for the First Time in 2020, While Market Average Sits at $137/kWh. Bloomberg 2020.

[9] Hsieh IYL, Pan MS, Chiang YM, Green WH. Learning only buys you so much: Practical limits on battery price reduction. Appl Energy 2019;239:218–24. https://doi.org/10.1016/J.APENERGY.2019.01.138.

[10] McKerracher C. Electric Vehicle Outlook Report 2021 | BloombergNEF | Bloomberg Finance LP n.d.

[11] European Commission. Transport emissions | Climate Action. Eur Comm 2014.

[12] The Royal Swedish Academy of Sciences. The Nobel Prize in Chemistry 2019. Nobel Media AB 2019.

[13] Bocconi S. Starace, frenata sul nucleare: «Siamo nel decennio delle rinnovabili»- Corriere.it. Corr Della Sera Econimia 2021.

[14] Winter M, Barnett B, Xu K. Before Li Ion Batteries 2018. https://doi.org/10.1021/acs.chemrev.8b00422.

[15] Wang L, Menakath A, Han F, Wang Y, Zavalij PY, Gaskell KJ, et al. Identifying the components of the solid–electrolyte interphase in Li-ion batteries. Nat Chem 2019 119 2019;11:789–96. https://doi.org/10.1038/s41557-019-0304-z.

[16] Huang G, Guo X, Cao X, Tian Q, Sun H. 3D network single-phase Ni0.9Zn0.1O as anode materials for lithium-ion batteries. Nano Energy 2016;28:338–45. https://doi.org/10.1016/J.NANOEN.2016.08.050.

[17] Palacín MR. Recent advances in rechargeable battery materials: a chemist's perspective. Chem Soc Rev 2009;38:2565–75. https://doi.org/10.1039/B820555H.

[18] Lee BS. A Review of Recent Advancements in Electrospun Anode Materials to Improve Rechargeable Lithium Battery Performance. Polym 2020, Vol 12, Page 2035 2020;12:2035. https://doi.org/10.3390/POLYM12092035.

[19] Subramanian V, Karki A, Gnanasekar KI, Eddy FP, Rambabu B. Nanocrystalline TiO2 (anatase) for Li-ion batteries. J Power Sources 2006;159:186–92. https://doi.org/10.1016/J.JPOWSOUR.2006.04.027.

[20] Chen Z, Belharouak I, Sun Y-K, Amine K. Titanium-Based Anode Materials for Safe Lithium-Ion Batteries. Adv Funct Mater 2013;23:959–69.

https://doi.org/10.1002/ADFM.201200698.

[21] Zhu G-N, Wang Y-G, Xia Y-Y. Ti-based compounds as anode materials for Li-ion batteries. Energy Environ Sci 2012;5:6652–67. https://doi.org/10.1039/C2EE03410G.

[22] Raccichini R, Varzi A, Passerini S, Scrosati B. The role of graphene for electrochemical energy storage. Nat Mater 2014 143 2014;14:271–9. https://doi.org/10.1038/nmat4170.

[23] J C, L M, D L, MR P. Beyond intercalation-based Li-ion batteries: the state of the art and challenges of electrode materials reacting through conversion reactions. Adv Mater 2010;22. https://doi.org/10.1002/ADMA.201000717.

[24] Yu S-H, Feng X, Zhang N, Seok J, Abruña HD. Understanding Conversion-Type Electrodes for Lithium Rechargeable Batteries. Acc Chem Res 2018;51:273–81. https://doi.org/10.1021/ACS.ACCOUNTS.7B00487.

[25] Zheng F, Kotobuki M, Song S, Lai MO, Lu L. Review on solid electrolytes for all-solid-state lithium-ion batteries. J Power Sources 2018;389:198–213. https://doi.org/10.1016/J.JPOWSOUR.2018.04.022.

[26] Blomgren GE. Liquid electrolytes for lithium and lithium-ion batteries. J Power Sources 2003;119–121:326–9. https://doi.org/10.1016/S0378-7753(03)00147-2.

[27] Younesi R, Veith GM, Johansson P, Edström K, Vegge T. Lithium salts for advanced lithium batteries: Li–metal, Li–O2, and Li–S. Energy Environ Sci 2015;8:1905–22. https://doi.org/10.1039/C5EE01215E.

[28] Seo DM, Reininger S, Kutcher M, Redmond K, Euler WB, Lucht BL. Role of Mixed Solvation and Ion Pairing in the Solution Structure of Lithium Ion Battery Electrolytes. J Phys Chem C 2015;119:14038–46. https://doi.org/10.1021/ACS.JPCC.5B03694.

[29] Ashassi-Sorkhabi H, Kazempour A, Salehi-Abar P. On the first coordination shell of lithium ion in linear carbonate solvents as electrolyte model for lithium-ion batteries: a computational study. Ionics 2019 258 2019;25:3705–13. https://doi.org/10.1007/S11581-019-02918-5.

[30] Foreman E, Zakri W, Hossein Sanatimoghaddam M, Modjtahedi A, Pathak S, Kashkooli AG, et al. A Review of Inactive Materials and Components of Flexible Lithium-Ion Batteries. Adv Sustain Syst 2017;1. https://doi.org/10.1002/ADSU.201700061.

[31] Wang A, Kadam S, Li H, Shi S, Qi Y. Review on modeling of the anode solid electrolyte interphase (SEI) for lithium-ion batteries. Npj Comput Mater 2018 41 2018;4:1–26. https://doi.org/10.1038/s41524-018-0064-0.

[32] Peled E, Menkin S. Review—SEI: Past, Present and Future. J Electrochem Soc 2017;164:A1703. https://doi.org/10.1149/2.1441707JES.

[33] Shi S, Lu P, Liu Z, Qi Y, Louis G. Hector J, Li H, et al. Direct Calculation of Li-Ion Transport in the Solid Electrolyte Interphase. J Am Chem Soc 2012;134:15476–87. https://doi.org/10.1021/JA305366R.

[34] Peled E, Golodnitsky D, Ardel G. Advanced Model for Solid Electrolyte Interphase Electrodes in Liquid and Polymer Electrolytes. J Electrochem Soc 1997;144:L208. https://doi.org/10.1149/1.1837858.

[35] Li T, Balbuena PB. Theoretical studies of the reduction of ethylene carbonate. Chem Phys Lett 2000;317:421–9. https://doi.org/10.1016/S0009-2614(99)01374-3.

[36] Xing L, Borodin O, Smith GD, Li W. Density Functional Theory Study of the Role of Anions on the Oxidative Decomposition Reaction of Propylene Carbonate. J Phys Chem A 2011;115:13896–905. https://doi.org/10.1021/JP206153N.

[37] Zhang X, Pugh JK, Ross PN. Computation of Thermodynamic Oxidation

Potentials of Organic Solvents Using Density Functional Theory. J Electrochem Soc 2001;148:E183. https://doi.org/10.1149/1.1362546.

[38] Nguyen CC, Yoon T, Seo DM, Guduru P, Lucht BL. Systematic Investigation of Binders for Silicon Anodes: Interactions of Binder with Silicon Particles and Electrolytes and Effects of Binders on Solid Electrolyte Interphase Formation. ACS Appl Mater Interfaces 2016;8:12211–20. https://doi.org/10.1021/ACSAMI.6B03357.

[39] Bresser D, Buchholz D, Moretti A, Varzi A, Passerini S. Alternative binders for sustainable electrochemical energy storage – the transition to aqueous electrode processing and bio-derived polymers. Energy Environ Sci 2018;11:3096–127. https://doi.org/10.1039/C8EE00640G.

[40] Jana KK, Lue SJ, Huang A, Soesanto JF, Tung K-L. Separator Membranes for High Energy-Density Batteries. ChemBioEng Rev 2018;5:346–71. https://doi.org/10.1002/CBEN.201800014.

[41] Andersson AM, Edström K. Chemical Composition and Morphology of the Elevated Temperature SEI on Graphite. J Electrochem Soc 2001;148:A1100. https://doi.org/10.1149/1.1397771.

[42] Malmgren S, Ciosek K, Lindblad R, Plogmaker S, Kühn J, Rensmo H, et al. Consequences of air exposure on the lithiated graphite SEI. Electrochim Acta 2013;105:83–91. https://doi.org/10.1016/J.ELECTACTA.2013.04.118.

[43] Raccichini R, Varzi A, Passerini S, Scrosati B. The role of graphene for electrochemical energy storage. Nat Mater 2014 143 2014;14:271–9. https://doi.org/10.1038/nmat4170.

[44] Saqib Shams S, Zhang R, Zhu J. Graphene synthesis: a Review. Mater Sci 2015;33:566–78. https://doi.org/10.1515/msp-2015-0079.

[45] Neto AHC, Guinea F, Peres NMR, Novoselov KS, Geim AK. The electronic

properties of graphene. Rev Mod Phys 2009;81:109. https://doi.org/10.1103/RevModPhys.81.109.

[46] Weir A, Westerhoff P, Fabricius L, Hristovski K, Goetz N von. Titanium Dioxide Nanoparticles in Food and Personal Care Products. Environ Sci Technol 2012;46:2242–50. https://doi.org/10.1021/ES204168D.

[47] Bai Y, Mora-Seró I, Angelis F De, Bisquert J, Wang P. Titanium Dioxide Nanomaterials for Photovoltaic Applications. Chem Rev 2014;114:10095–130. https://doi.org/10.1021/CR400606N.

[48] Yang H, Zhu S, Pan N. Studying the mechanisms of titanium dioxide as ultraviolet-blocking additive for films and fabrics by an improved scheme. J Appl Polym Sci 2004;92:3201–10. https://doi.org/10.1002/APP.20327.

[49] Wang D, Choi D, Li J, Yang Z, Nie Z, Kou R, et al. Self-Assembled TiO2–Graphene Hybrid Nanostructures for Enhanced Li-Ion Insertion. ACS Nano 2009;3:907–14. https://doi.org/10.1021/NN900150Y.

[50] Filice S, D'Angelo D, Libertino S, Nicotera I, Kosma V, Privitera V, et al. Graphene oxide and titania hybrid Nafion membranes for efficient removal of methyl orange dye from water. Carbon N Y 2015;C:489–99. https://doi.org/10.1016/J.CARBON.2014.10.093.

[51] Bergamonti L, Predieri G, Paz Y, Fornasini L, Lottici PP, Bondioli F. Enhanced self-cleaning properties of N-doped TiO2 coating for Cultural Heritage. Microchem J 2017;C:1–12. https://doi.org/10.1016/J.MICROC.2017.03.003.

[52] Frazer L. Titanium dioxide: Environmental white knight? Environ Health Perspect 2001;109. https://doi.org/10.2307/3454883.

[53] Hearne GR, Zhao J, Dawe AM, Pischedda V, Maaza M, Nieuwoudt MK, et al. Effect of grain size on structural transitions in anatase TiO2: A Raman spectroscopy study at high pressure. Phys Rev B - Condens Matter Mater Phys

2004;70:134102. https://doi.org/10.1103/PhysRevB.70.134102.

[54] Zhang H, Banfield JF. Structural Characteristics and Mechanical and Thermodynamic Properties of Nanocrystalline TiO2. Chem Rev 2014;114:9613–44. https://doi.org/10.1021/CR500072J.

[55] MT N, MA A, A A. Synthesis and applications of nano-TiO 2: a review. Environ Sci Pollut Res Int 2019;26:3262–91. https://doi.org/10.1007/S11356-018-3884-Z.

[56] and C-CW, Ying* JY. Sol−Gel Synthesis and Hydrothermal Processing of Anatase and Rutile Titania Nanocrystals. Chem Mater 1999;11:3113–20. https://doi.org/10.1021/CM990180F.

[57] Sandhya CP, John B, Gouri C. Lithium titanate as anode material for lithium-ion cells: a review n.d. https://doi.org/10.1007/s11581-014-1113-4.

[58] Guler MO, Cevher O, Cetinkaya T, Tocoglu U, Akbulut H. High capacity TiO2 anode materials for Li-ion batteries. Energy Convers Manag 2013;72:111–6. https://doi.org/10.1016/J.ENCONMAN.2012.11.026.

[59] Liu S, Wang Z, Yu C, Wu H Bin, Wang G, Dong Q, et al. A Flexible TiO2(B)-Based Battery Electrode with Superior Power Rate and Ultralong Cycle Life. Adv Mater 2013;25:3462–7. https://doi.org/10.1002/ADMA.201300953.

[60] Zhang H, Banfield JF. Structural Characteristics and Mechanical and Thermodynamic Properties of Nanocrystalline TiO2. Chem Rev 2014;114:9613–44. https://doi.org/10.1021/CR500072J.

[61] Koudriachova M V., Harrison NM, De Leeuw SW. Diffusion of Li-ions in rutile. An ab initio study. Solid State Ionics 2003;157:35–8. https://doi.org/10.1016/S0167-2738(02)00186-8.

[62] Marnix Wagemaker †, Gordon J. Kearley †, Ad A. van Well †, Hannu Mutka ‡ and, Fokko M. Mulder* †. Multiple Li Positions inside Oxygen Octahedra in

Lithiated TiO2 Anatase. J Am Chem Soc 2002;125:840–8. https://doi.org/10.1021/JA028165Q.

[63] Kubiak P, Fröschl T, Hüsing N, Hörmann U, Kaiser U, Schiller R, et al. TiO2 Anatase Nanoparticle Networks: Synthesis, Structure, and Electrochemical Performance. Small 2011;7:1690–6. https://doi.org/10.1002/SMLL.201001943.

[64] Madian M, Eychmüller A, Giebeler L. Current Advances in TiO2-Based Nanostructure Electrodes for High Performance Lithium Ion Batteries. Batter 2018, Vol 4, Page 7 2018;4:7. https://doi.org/10.3390/BATTERIES4010007.

[65] Shin J-Y, Samuelis D, Maier J. Sustained Lithium-Storage Performance of Hierarchical, Nanoporous Anatase TiO2 at High Rates: Emphasis on Interfacial Storage Phenomena. Adv Funct Mater 2011;21:3464–72. https://doi.org/10.1002/adfm.201002527.

[66] Park SJ, Kim H, Kim YJ, Lee H. Preparation of carbon-coated TiO2 nanostructures for lithium-ion batteries. Electrochim Acta 2011;56:5355–62. https://doi.org/10.1016/j.electacta.2011.03.119.

[67] Xin X, Zhou X, Wu J, Yao X, Liu Z. Scalable Synthesis of TiO 2 /Graphene Nanostructured Composite with High-Rate Performance for Lithium Ion Batteries 2012. https://doi.org/10.1021/nn304725m.

[68] Wang D, Choi D, Li J, Yang Z, Nie Z, Kou R, et al. Self-Assembled TiO 2-Graphene Hybrid Nanostructures for Enhanced Li-Ion Insertion 2009. https://doi.org/10.1021/nn900150y.

[69] SCiB™ Rechargeable battery | Toshiba n.d.

[70] Ma Z, Jing F, Fan Y, Li J, Zhao Y, Shao G. High electrical conductivity of 3D mesporous carbon nanocage as an efficient polysulfide buffer layer for high sulfur utilization in lithium-sulfur batteries. J Alloys Compd 2019;789:71–9. https://doi.org/10.1016/J.JALLCOM.2019.03.035.

[71] Laboratories CI, Clark RJH, Cobbold DG. Characterization of Sulfur Radical Anions Contribution from the Characterization of Sulfur Radical Anions in Solutions of Alkali Polysulfides in Dimethylformamide and Hexamethylphosphoramide and in the Solid State in Ultramarine Blue, Green, and Red. Inorg Chem 1978;17:3169.

[72] Tobishima SI, Yamamoto H, Matsuda M. Study on the reduction species of sulfur by alkali metals in nonaqueous solvents. Electrochim Acta 1997;42:1019–29. https://doi.org/10.1016/S0013-4686(96)00281-2.

[73] Zhang SS, Tran DT. A proof-of-concept lithium/sulfur liquid battery with exceptionally high capacity density. J Power Sources 2012;211:169–72. https://doi.org/10.1016/J.JPOWSOUR.2012.04.006.

[74] Lee S-Y, Choi K-H, Choi W-S, Kwon YH, Jung H-R, Shin H-C, et al. Progress in flexible energy storage and conversion systems, with a focus on cable-type lithium-ion batteries. Energy Environ Sci 2013;6:2414–23. https://doi.org/10.1039/C3EE24260A.

[75] Gao X-P, Yang H-X. Multi-electron reaction materials for high energy density batteries. Energy Environ Sci 2010;3:174–89. https://doi.org/10.1039/B916098A.

[76] Zhou G, Li F, Cheng H-M. Progress in flexible lithium batteries and future prospects. Energy Environ Sci 2014;7:1307–38. https://doi.org/10.1039/C3EE43182G.

[77] Hagen M, Dörfler S, Fanz P, Berger T, Speck R, Tübke J, et al. Development and costs calculation of lithium–sulfur cells with high sulfur load and binder free electrodes. J Power Sources 2013;224:260–8. https://doi.org/10.1016/J.JPOWSOUR.2012.10.004.

[78] Fongy C, Gaillot A-C, Jouanneau S, Guyomard D, Lestriez B. Ionic vs Electronic Power Limitations and Analysis of the Fraction of Wired Grains in LiFePO 4

Composite Electrodes. J Electrochem Soc 2010;157:885–91. https://doi.org/10.1149/1.3432559.

[79] Hu L, Mantia F La, Wu H, Xie X, McDonough J, Pasta M, et al. Lithium-Ion Textile Batteries with Large Areal Mass Loading. Adv Energy Mater 2011;1:1012–7. https://doi.org/10.1002/AENM.201100261.

[80] Chung S-H, Manthiram A. Rational Design of Statically and Dynamically Stable Lithium–Sulfur Batteries with High Sulfur Loading and Low Electrolyte/Sulfur Ratio. Adv Mater 2018;30:1705951. https://doi.org/10.1002/ADMA.201705951.

[81] Zhang SS. Improved Cyclability of Liquid Electrolyte Lithium/Sulfur Batteries by Optimizing Electrolyte/Sulfur Ratio. Energies 2012, Vol 5, Pages 5190-5197 2012;5:5190–7. https://doi.org/10.3390/EN5125190.

[82] Chen S, Gao Y, Yu Z, Gordin ML, Song J, Wang D. High capacity of lithium-sulfur batteries at low electrolyte/sulfur ratio enabled by an organosulfide containing electrolyte. Nano Energy 2017;31:418–23. https://doi.org/10.1016/J.NANOEN.2016.11.057.

[83] Zhang SS. Liquid electrolyte lithium/sulfur battery: Fundamental chemistry, problems, and solutions. J Power Sources 2013;231:153–62. https://doi.org/10.1016/J.JPOWSOUR.2012.12.102.

[84] Xue W, Miao L, Qie L, Wang C, Li S, Wang J, et al. Gravimetric and volumetric energy densities of lithium-sulfur batteries. Curr Opin Electrochem 2017;6:92–9. https://doi.org/10.1016/J.COELEC.2017.10.007.

[85] Green MA. Intrinsic concentration, effective densities of states, and effective mass in silicon. J Appl Phys 1998;67:2944. https://doi.org/10.1063/1.345414.

[86] Chan CK, Peng H, Liu G, McIlwrath K, Zhang XF, Huggins RA, et al. High-performance lithium battery anodes using silicon nanowires. Nat Nanotechnol 2008 31 2007;3:31–5. https://doi.org/10.1038/nnano.2007.411.

[87] R T, MK D, R K, TC P, TM L, PN K, et al. Nanostructured silicon anodes for lithium ion rechargeable batteries. Small 2009;5:2236–42. https://doi.org/10.1002/SMLL.200900382.

[88] Goriparti S, Miele E, De Angelis F, Di Fabrizio E, Proietti Zaccaria R, Capiglia C. Review on recent progress of nanostructured anode materials for Li-ion batteries. J Power Sources 2014;257:421–43. https://doi.org/10.1016/J.JPOWSOUR.2013.11.103.

[89] Wu H, Cui Y. Designing nanostructured Si anodes for high energy lithium ion batteries. Nano Today 2012. https://doi.org/10.1016/j.nantod.2012.08.004.

[90] Chandrasiri KWDK, Nguyen CC, Parimalam BS, Jurng S, Lucht BL. Citric Acid Based Pre-SEI for Improvement of Silicon Electrodes in Lithium Ion Batteries. J Electrochem Soc 2018;165:A1991. https://doi.org/10.1149/2.0161810JES.

[91] Parikh P, Sina M, Banerjee A, Wang X, Savio M, Souza D', et al. Role of Polyacrylic Acid (PAA) Binder on the Solid Electrolyte Interphase in Silicon Anodes 2019. https://doi.org/10.1021/acs.chemmater.8b05020.

[92] Mazouzi D, Karkar Z, Hernandez CR, Manero PJ, Guyomard D, Roué L, et al. Critical roles of binders and formulation at multiscales of silicon-based composite electrodes. J Power Sources 2015;280:533–49. https://doi.org/10.1016/J.JPOWSOUR.2015.01.140.

[93] Dou F, Shi L, Chen G, Zhang D. Silicon/Carbon Composite Anode Materials for Lithium-Ion Batteries. Electrochem Energy Rev 2019 21 2019;2:149–98. https://doi.org/10.1007/S41918-018-00028-W.

[94] Sila Nanotechnologies' battery technology will launch in Whoop wearables | TechCrunch n.d.

[95] Battery2030+ - Battery 2030+.

[96] Novoselov KS, Geim AK, Morozov S V., Jiang D, Katsnelson MI, Grigorieva I V., et al. Two-dimensional gas of massless Dirac fermions in graphene. Nat 2005 4387065 2005;438:197–200. https://doi.org/10.1038/nature04233.

[97] Stoller MD, Park S, Zhu Y, An J, Ruoff RS. Graphene-Based Ultracapacitors. Nano Lett 2008;8:3498–502. https://doi.org/10.1021/NL802558Y.

[98] Wang Y, Shi Z, Huang Y, Ma Y, Wang C, Chen M, et al. Supercapacitor Devices Based on Graphene Materials. J Phys Chem C 2009;113:13103–7. https://doi.org/10.1021/JP902214F.

[99] Liu C, Yu Z, Neff D, Zhamu A, Jang BZ. Graphene-Based Supercapacitor with an Ultrahigh Energy Density. Nano Lett 2010;10:4863–8. https://doi.org/10.1021/NL102661Q.

[100] Al-Dhahebi AM, Gopinath SCB, Saheed MSM. Graphene impregnated electrospun nanofiber sensing materials: a comprehensive overview on bridging laboratory set-up to industry. Nano Converg 2020 71 2020;7:1–23. https://doi.org/10.1186/S40580-020-00237-4.

[101] Muñoz R, Gómez-Aleixandre C. Review of CVD Synthesis of Graphene. Chem Vap Depos 2013;19:297–322. https://doi.org/10.1002/CVDE.201300051.

[102] Yazdi GR, Iakimov T, Yakimova R. Epitaxial Graphene on SiC: A Review of Growth and Characterization. Cryst 2016, Vol 6, Page 53 2016;6:53. https://doi.org/10.3390/CRYST6050053.

[103] J K, S K, DH C, B K, H K, Y K, et al. Direct exfoliation and dispersion of two-dimensional materials in pure water via temperature control. Nat Commun 2015;6. https://doi.org/10.1038/NCOMMS9294.

[104] Arao Y, Kubouchi M. High-rate production of few-layer graphene by high-power probe sonication. Carbon N Y 2015;95:802–8. https://doi.org/10.1016/J.CARBON.2015.08.108.

[105] Luo B, Pu Y-C, Yang Y, Lindley SA, Abdelmageed G, Ashry H, et al. Synthesis, Optical Properties, and Exciton Dynamics of Organolead Bromide Perovskite Nanocrystals. J Phys Chem C 2015;119:26672–82. https://doi.org/10.1021/ACS.JPCC.5B08537.

[106] Halbig CE, Nacken TJ, Walter J, Damm C, Eigler S, Peukert W. Quantitative investigation of the fragmentation process and defect density evolution of oxo-functionalized graphene due to ultrasonication and milling. Carbon N Y 2016;96:897–903. https://doi.org/10.1016/J.CARBON.2015.10.021.

[107] Jeon I-Y, Bae S-Y, Seo J-M, Baek J-B. Scalable Production of Edge-Functionalized Graphene Nanoplatelets via Mechanochemical Ball-Milling. Adv Funct Mater 2015;25:6961–75. https://doi.org/10.1002/ADFM.201502214.

[108] Najafabadi AT, Gyenge E. Synergistic production of graphene microsheets by simultaneous anodic and cathodic electro-exfoliation of graphitic electrodes in aprotic ionic liquids. Carbon N Y 2015;84:449–59. https://doi.org/10.1016/J.CARBON.2014.12.041.

[109] Hamra AAB, Lim HN, Chee WK, Huang NM. Electro-exfoliating graphene from graphite for direct fabrication of supercapacitor. Appl Surf Sci 2016;360:213–23. https://doi.org/10.1016/J.APSUSC.2015.11.006.

[110] Najafabadi AT, Gyenge E. High-yield graphene production by electrochemical exfoliation of graphite: Novel ionic liquid (IL)–acetonitrile electrolyte with low IL content. Carbon N Y 2014;71:58–69. https://doi.org/10.1016/J.CARBON.2014.01.012.

[111] Valentina Tozzini, Vittorio Pellegrini. Prospects for hydrogen storage in graphene. Phys Chem Chem Phys 2012;15:80–9. https://doi.org/10.1039/C2CP42538F.

[112] Hur SH, Park J-N. Graphene and its application in fuel cell catalysis: a review. Asia-Pacific J Chem Eng 2013;8:218–33. https://doi.org/10.1002/APJ.1676.

[113] Dahn JR, Zheng T, Liu Y, Xue JS. Mechanisms for lithium insertion in carbonaceous materials. Science (80-) 1995;270:590–3. https://doi.org/10.1126/SCIENCE.270.5236.590.

[114] Lian P, Zhu X, Liang S, Li Z, Yang W, Wang H. Large reversible capacity of high quality graphene sheets as an anode material for lithium-ion batteries. Electrochim Acta 2010;55:3909–14. https://doi.org/10.1016/J.ELECTACTA.2010.02.025.

[115] Jiao L, Liu Z, Sun Z, Wu T, Gao Y, Li H, et al. An advanced lithium ion battery based on a high quality graphitic graphene anode and a Li[Ni0.6Co0.2Mn0.2]O2 cathode. Electrochim Acta 2018;259:48–55. https://doi.org/10.1016/j.electacta.2017.10.155.

[116] Wang G, Shen X, Yao J, Park J. Graphene nanosheets for enhanced lithium storage in lithium ion batteries. Carbon N Y 2009;47:2049–53. https://doi.org/10.1016/J.CARBON.2009.03.053.

[117] Pramudita JC, Pontiroli D, Magnani G, Gaboardi M, Riccò M, Milanese C, et al. Graphene and Selected Derivatives as Negative Electrodes in Sodium- and Lithium-Ion Batteries. ChemElectroChem 2015;2:600–10. https://doi.org/10.1002/celc.201402352.

[118] C. OAV, Caballero Á, Morales J. Can the performance of graphene nanosheets for lithium storage in Li-ion batteries be predicted? Nanoscale 2012;4:2083–92. https://doi.org/10.1039/C2NR11936F.

[119] F. Xiang H, D. Li Z, K. Xie, Z. Jiang J, J. Chen J, C. Lian P, et al. Graphene sheets as anode materials for Li-ion batteries: preparation, structure, electrochemical properties and mechanism for lithium storage. RSC Adv 2012;2:6792–9. https://doi.org/10.1039/C2RA20549A.

[120] Wu ZS, Zhou G, Yin LC, Ren W, Li F, Cheng HM. Graphene/metal oxide composite electrode materials for energy storage. Nano Energy 2012;1:107–31.

https://doi.org/10.1016/J.NANOEN.2011.11.001.

[121] Huang X, Zeng Z, Fan Z, Liu J, Zhang H. Graphene-Based Electrodes. Adv Mater 2012;24:5979–6004. https://doi.org/10.1002/ADMA.201201587.

[122] Zhai PY, Peng HJ, Cheng XB, Zhu L, Huang JQ, Zhu W, et al. Scaled-up fabrication of porous-graphene-modified separators for high-capacity lithium–sulfur batteries. Energy Storage Mater 2017;7:56–63. https://doi.org/10.1016/J.ENSM.2016.12.004.

[123] Lei T, Chen W, Lv W, Huang J, Zhu J, Chu J, et al. Inhibiting Polysulfide Shuttling with a Graphene Composite Separator for Highly Robust Lithium-Sulfur Batteries. Joule 2018;2:2091–104. https://doi.org/10.1016/J.JOULE.2018.07.022.

[124] Zhou G, Li L, Wang D-W, Shan X, Pei S, Li F, et al. A Flexible Sulfur-Graphene-Polypropylene Separator Integrated Electrode for Advanced Li–S Batteries. Adv Mater 2015;27:641–7. https://doi.org/10.1002/ADMA.201404210.

[125] Richard Prabakar SJ, Hwang YH, Bae EG, Lee DK, Pyo M. Graphene oxide as a corrosion inhibitor for the aluminum current collector in lithium ion batteries. Carbon N Y 2013;52:128–36. https://doi.org/10.1016/J.CARBON.2012.09.013.

[126] Kim HR, Choi WM. Graphene modified copper current collector for enhanced electrochemical performance of Li-ion battery. Scr Mater 2018;146:100–4. https://doi.org/10.1016/J.SCRIPTAMAT.2017.11.030.

[127] Chen Y, Fu K, Zhu S, Luo W, Wang Y, Li Y, et al. Reduced Graphene Oxide Films with Ultrahigh Conductivity as Li-Ion Battery Current Collectors. Nano Lett 2016;16:3616–23. https://doi.org/10.1021/ACS.NANOLETT.6B00743.

[128] Mo R, Lei Z, Sun K, Rooney D. Facile Synthesis of Anatase TiO2 Quantum-Dot/Graphene-Nanosheet Composites with Enhanced Electrochemical Performance for Lithium-Ion Batteries. Adv Mater 2014;26:2084–8. https://doi.org/10.1002/ADMA.201304338.

[129] Menéndez R, Alvarez P, Botas C, Nacimiento F, Alcántara R, Tirado JL, et al. Self-organized amorphous titania nanotubes with deposited graphene film like a new heterostructured electrode for lithium ion batteries. J Power Sources 2014;248:886–93. https://doi.org/10.1016/J.JPOWSOUR.2013.10.019.

[130] Guifang Gu, Jianli Cheng, Xiaodong Li, Wei Ni, Qun Guan, Guoxing Qu, et al. Facile synthesis of graphene supported ultralong TiO 2 nanofibers from the commercial titania for high performance lithium-ion batteries. J Mater Chem A 2015;3:6642–8. https://doi.org/10.1039/C5TA00523J.

[131] Hoshide T, Zheng Y, Hou J, Wang Z, Li Q, Zhao Z, et al. Flexible Lithium-Ion Fiber Battery by the Regular Stacking of Two-Dimensional Titanium Oxide Nanosheets Hybridized with Reduced Graphene Oxide. Nano Lett 2017;17:3543–9. https://doi.org/10.1021/ACS.NANOLETT.7B00623.

[132] Li N, Liu G, Zhen C, Li F, Zhang L, Cheng HM. Battery performance and photocatalytic activity of mesoporous anatase TiO2 nanospheres/graphene composites by template-free self-assembly. Adv Funct Mater 2011;21:1717–22. https://doi.org/10.1002/ADFM.201002295.

[133] Gaboardi M, Bliersbach A, Bertoni G, Aramini M, Vlahopoulou G, Pontiroli D, et al. Decoration of graphene with nickel nanoparticles: Study of the interaction with hydrogen. J Mater Chem A 2014;2:1039–46. https://doi.org/10.1039/c3ta14127f.

[134] Ji X, Lee KT, Nazar LF. A highly ordered nanostructured carbon--sulphur cathode for lithium--sulphur batteries. Nat Mater 2009;8. https://doi.org/10.1038/NMAT2460.

[135] Arie AA, Kristianto H, Cengiz EC, Demir-Cakan R. Waste tea-based porous carbon–sulfur composite cathodes for lithium–sulfur battery. Ionics 2019 261 2019;26:201–12. https://doi.org/10.1007/S11581-019-03196-X.

[136] K. B, R. S, N. K. Exploration of microporous bio-carbon scaffold for efficient

utilization of sulfur in lithium-sulfur system. Electrochim Acta 2016;209:171–82. https://doi.org/10.1016/J.ELECTACTA.2016.05.069.

[137] Gu X, Wang Y, Lai C, Qiu J, Li S, Hou Y, et al. Microporous bamboo biochar for lithium-sulfur batteries. Nano Res 2015 81 2014;8:129–39. https://doi.org/10.1007/S12274-014-0601-1.

[138] Noh H, Choi S, Kim HG, Choi M, Kim H-T. Size Tunable Zeolite-Templated Carbon as Microporous Sulfur Host for Lithium-Sulfur Batteries. ChemElectroChem 2019;6:558–65. https://doi.org/10.1002/CELC.201801148.

[139] Tang C, Li B-Q, Zhang Q, Zhu L, Wang H-F, Shi J-L, et al. CaO-Templated Growth of Hierarchical Porous Graphene for High-Power Lithium–Sulfur Battery Applications. Adv Funct Mater 2016;26:577–85. https://doi.org/10.1002/ADFM.201503726.

[140] Wu S, Ge R, Lu M, Xu R, Zhang Z. Graphene-based nano-materials for lithium–sulfur battery and sodium-ion battery. Nano Energy 2015;15:379–405. https://doi.org/10.1016/J.NANOEN.2015.04.032.

[141] Li L, Shan Y. The use of graphene and its composites to suppress the shuttle effect in lithium-sulfur batteries. New Carbon Mater 2021;36:336–49. https://doi.org/10.1016/S1872-5805(21)60023-9.

[142] Yu M, Li R, Wu M, Shi G. Graphene materials for lithium–sulfur batteries. Energy Storage Mater 2015;1:51–73. https://doi.org/10.1016/J.ENSM.2015.08.004.

[143] Wang B, Li X, Zhang X, Luo B, Jin M, Liang M, et al. Adaptable Silicon–Carbon Nanocables Sandwiched between Reduced Graphene Oxide Sheets as Lithium Ion Battery Anodes. ACS Nano 2013;7:1437–45. https://doi.org/10.1021/NN3052023.

[144] Wang W, Epur R, Kumta PN. Vertically aligned silicon/carbon nanotube (VASCNT) arrays: Hierarchical anodes for lithium-ion battery. Electrochem Commun 2011;13:429–32. https://doi.org/10.1016/J.ELECOM.2011.02.012.

[145] Shen X, Tian Z, Fan R, Shao L, Zhang D, Cao G, et al. Research progress on silicon/carbon composite anode materials for lithium-ion battery. J Energy Chem 2018;27:1067–90. https://doi.org/10.1016/J.JECHEM.2017.12.012.

[146] Cavallari C, Rols S, Fischer HE, Brunelli M, Gaboardi M, Magnani G, et al. Neutron scattering study of nickel decorated thermally exfoliated graphite oxide. Int J Hydrogen Energy 2019;44:30999–1007. https://doi.org/10.1016/J.IJHYDENE.2019.09.226.

[147] Botas C, Álvarez P, Blanco P, Granda M, Blanco C, Santamaría R, et al. Graphene materials with different structures prepared from the same graphite by the Hummers and Brodie methods. Carbon N Y 2013;65:156–64. https://doi.org/10.1016/j.carbon.2013.08.009.

[148] Marcano DC, Kosynkin D V., Berlin JM, Sinitskii A, Sun Z, Slesarev A, et al. Improved Synthesis of Graphene Oxide. ACS Nano 2010;4:4806–14. https://doi.org/10.1021/NN1006368.

[149] Shao G, Lu Y, Wu F, Yang C, Zeng F, Wu Q. Graphene oxide: the mechanisms of oxidation and exfoliation. J Mater Sci 2012 4710 2012;47:4400–9. https://doi.org/10.1007/S10853-012-6294-5.

[150] Zhao X, Jin W, Cai J, Ye J, Li Z, Ma Y, et al. Shape- and Size-Controlled Synthesis of Uniform Anatase TiO2 Nanocuboids Enclosed by Active {100} and {001} Facets. Adv Funct Mater 2011;21:3554–63. https://doi.org/10.1002/adfm.201100629.

[151] Jeon BH, Yeon JH, Kim KM, Chung IJ. Preparation and electrochemical properties of lithium–sulfur polymer batteries. J Power Sources 2002;109:89–97. https://doi.org/10.1016/S0378-7753(02)00050-2.

[152] Choi JW, Kim JK, Cheruvally G, Ahn JH, Ahn HJ, Kim KW. Rechargeable lithium/sulfur battery with suitable mixed liquid electrolytes. Electrochim Acta

2007;52:2075–82. https://doi.org/10.1016/J.ELECTACTA.2006.08.016.

[153] Zhang Y, Zhao Y, Bakenov Z. A novel lithium/sulfur battery based on sulfur/graphene nanosheet composite cathode and gel polymer electrolyte. Nanoscale Res Lett 2014;9:1–7. https://doi.org/10.1186/1556-276X-9-137/FIGURES/4.

[154] Liu G, Su Z, He D, Lai C. Wet ball-milling synthesis of high performance sulfur-based composite cathodes: The influences of solvents and ball-milling speed. Electrochim Acta 2014;149:136–43. https://doi.org/10.1016/J.ELECTACTA.2014.10.033.

[155] Xu G, Yuan J, Geng X, Dou H, Chen L, Yan X, et al. Caterpillar-like graphene confining sulfur by restacking effect for high performance lithium sulfur batteries. Chem Eng J 2017;322:454–62. https://doi.org/10.1016/J.CEJ.2017.04.052.

[156] Yu Z, Zhang N, Zhang X, Li Y, Xie G, Ge W, et al. Synthesis and research of layered CoS/graphene nanoflakes as sulfur cathode for high-energy lithium sulfur batteries. J Electroanal Chem 2019;854:113524. https://doi.org/10.1016/J.JELECHEM.2019.113524.

[157] Vos R, Lux M, Xu K, Fyen W, Kenens C, Conard T, et al. Removal of Submicrometer Particles from Silicon Wafer Surfaces Using HF-Based Cleaning Mixtures. J Electrochem Soc 2001;148:G683. https://doi.org/10.1149/1.1413483/XML.

[158] Verhaverbeke S, Teerlinck I, Vinckier C, Stevens G, Cartuyvels R, Heyns MM. The Etching Mechanisms of SiO2 in Hydrofluoric Acid. J Electrochem Soc 1994;141:2852–7. https://doi.org/10.1149/1.2059243/XML.

[159] Mastronardi ML, Maier-Flaig F, Faulkner D, Henderson EJ, Kü C, Lemmer U, et al. Size-Dependent Absolute Quantum Yields for Size-Separated Colloidally-Stable Silicon Nanocrystals. Nano Lett 2012;12:27.

https://doi.org/10.1021/nl2036194.

[160] Sun W, Qian C, Cui XS, Wang L, Wei M, Casillas G, et al. Silicon monoxide – a convenient precursor for large scale synthesis of near infrared emitting monodisperse silicon nanocrystals. Nanoscale 2016;8:3678–84. https://doi.org/10.1039/C5NR09128D.

[161] Mohapatra P, Mendivelso-Perez D, Bobbitt JM, Shaw S, Yuan B, Tian X, et al. Large-Scale Synthesis of Colloidal Si Nanocrystals and Their Helium Plasma Processing into Spin-On, Carbon-Free Nanocrystalline Si Films. ACS Appl Mater Interfaces 2018;10:20740–7. https://doi.org/10.1021/ACSAMI.8B03771.

[162] Rondeau RE, Afb W-P. A Technique for Degassing Liquid Samples. J Chem Educ 1967;14:27.

[163] Yu X, Terakawa S, Hayashi S, Asaka T, Itoigawa F, Ono S, et al. Carbonization of Silicon Nanoparticles via Ablation Induced by Femtosecond Laser Pulses in Hexane. Arab J Sci Eng 2017 4210 2017;42:4221–6. https://doi.org/10.1007/S13369-017-2619-7.

[164] Valøen LO, Reimers JN. Transport Properties of LiPF[sub 6]-Based Li-Ion Battery Electrolytes. J Electrochem Soc 2005;152:A882. https://doi.org/10.1149/1.1872737/XML.

[165] Zhang S, Ueno K, Dokko K, Watanabe M, Zhang S, Ueno K, et al. Recent Advances in Electrolytes for Lithium–Sulfur Batteries. Adv Energy Mater 2015;5:1500117. https://doi.org/10.1002/AENM.201500117.

[166] Zhang SS. Role of LiNO3 in rechargeable lithium/sulfur battery. Electrochim Acta 2012;70:344–8. https://doi.org/10.1016/J.ELECTACTA.2012.03.081.

[167] Zhang L, Ling M, Feng J, Mai L, Liu G, Guo J. The synergetic interaction between LiNO3 and lithium polysulfides for suppressing shuttle effect of lithium-sulfur batteries. Energy Storage Mater 2018;11:24–9.

https://doi.org/10.1016/J.ENSM.2017.09.001.

[168] Zhang SS. A new finding on the role of LiNO3 in lithium-sulfur battery. J Power Sources 2016;322:99–105. https://doi.org/10.1016/J.JPOWSOUR.2016.05.009.

[169] Liang X, Wen Z, Liu Y, Wu M, Jin J, Zhang H, et al. Improved cycling performances of lithium sulfur batteries with LiNO3-modified electrolyte. J Power Sources 2011;196:9839–43. https://doi.org/10.1016/J.JPOWSOUR.2011.08.027.

[170] Xiong S, Xie K, Diao Y, Hong X. Properties of surface film on lithium anode with LiNO3 as lithium salt in electrolyte solution for lithium–sulfur batteries. Electrochim Acta 2012;83:78–86. https://doi.org/10.1016/J.ELECTACTA.2012.07.118.

[171] Zhang SS. Effect of Discharge Cutoff Voltage on Reversibility of Lithium/Sulfur Batteries with LiNO 3 -Contained Electrolyte . J Electrochem Soc 2012;159:A920–3. https://doi.org/10.1149/2.002207JES/XML.

[172] Zeng P, Han Y, Duan X, Jia G, Huang L, Chen Y. A stable graphite electrode in superconcentrated LiTFSI-DME/DOL electrolyte and its application in lithium-sulfur full battery. Mater Res Bull 2017;95:61–70. https://doi.org/10.1016/J.MATERRESBULL.2017.07.018.

[173] Krause A, Dörfler S, Piwko M, Wisser FM, Jaumann T, Ahrens E, et al. High Area Capacity Lithium-Sulfur Full-cell Battery with Prelitiathed Silicon Nanowire-Carbon Anodes for Long Cycling Stability. Sci Reports 2016 61 2016;6:1–12. https://doi.org/10.1038/srep27982.

[174] FullProf Suite Homepage.

[175] THE FIT2D HOME PAGE.

[176] Match! - Phase Analysis using Powder Diffraction.

[177] Toby BH, Von Dreele RB. GSAS-II: The genesis of a modern open-source all

purpose crystallography software package. J Appl Crystallogr 2013;46:544–9. https://doi.org/10.1107/S0021889813003531.

[178] LabSpec 6 Spectroscopy Suite Software - HORIBA.

[179] SEM vs TEM | Technology Networks.

[180] Besenhard JO. Handbook of battery materials 1999:618.

[181] How do Synchrotrons Work?.

[182] Rebuffi L, Plaisier JR, Abdellatief M, Lausi A, Scardi AP. Mcx: A synchrotron radiation beamline for X-ray diffraction line profile analysis. Zeitschrift Fur Anorg Und Allg Chemie 2014;640:3100–6. https://doi.org/10.1002/zaac.201400163.

[183] Freiman SW. Standard Reference Material ® 660a Lanthanum Hexaboride Powder Line Position and Line Shape Standard for Powder Diffraction Standard Reference Materials Program 2000.

[184] Material SR. Silicon Powder (Line Position and Line Shape Standard for Powder Diffraction) 2015:1–5.

[185] Latychevskaia T, Son SK, Yang Y, Chancellor D, Brown M, Ozdemir S, et al. Stacking transition in rhombohedral graphite. Front Phys 2019 141 2018;14:1–7. https://doi.org/10.1007/S11467-018-0867-Y.

[186] Mattia Gaboardi, Andreas Bliersbach, Giovanni Bertoni, Matteo Aramini, Gina Vlahopoulou, Daniele Pontiroli, et al. Decoration of graphene with nickel nanoparticles: study of the interaction with hydrogen. J Mater Chem A 2013;2:1039–46. https://doi.org/10.1039/C3TA14127F.

[187] Zhang H, Banfield JF. Understanding polymorphic phase transformation behavior during growth of nanocrystalline aggregates: Insights from TiO2. J Phys Chem B 2000;104:3481–7. https://doi.org/10.1021/jp000499j.

[188] Bersani D, Lottici PP, Ding X-Z. Phonon confinement effects in the Raman scattering by TiO2 nanocrystals. Appl Phys Lett 1998;72:73. https://doi.org/10.1063/1.120648.

[189] Tompsett GA, Bowmaker GA, Cooney RP, Metson JB, Rodgers KA, Seakins JM. The Raman spectrum of brookite, TiO2 (Pbca, Z = 8). J Raman Spectrosc 1995;26:57–62. https://doi.org/10.1002/JRS.1250260110.

[190] Bersani D, Lottici PP, Ding XZ. Phonon confinement effects in the Raman scattering by TiO2 nanocrystals. Appl Phys Lett 1998;72:73–5. https://doi.org/10.1063/1.120648.

[191] Gajovi A, Stubičar M, Ivanda M, Furi K. Raman spectroscopy of ball-milled TiO2. J Mol Struct 2001;563–564:315–20. https://doi.org/10.1016/S0022-2860(00)00790-0.

[192] Gajović A, Stubičar M, Ivanda M, Furić K. Raman Spectroscopy of ball-milled TiO2. J Mol Struct 2001;563:315–20. https://doi.org/10.1016/S0022-2860(00)00790-0.

[193] Ferrari AC. Raman spectroscopy of graphene and graphite: Disorder, electron–phonon coupling, doping and nonadiabatic effects. Solid State Commun 2007;143:47–57. https://doi.org/10.1016/J.SSC.2007.03.052.

[194] Pan F, Yang J, Huang Q, Wang X, Huang H, Wang Q, et al. Redox Targeting of Anatase TiO2 for Redox Flow Lithium-Ion Batteries. Adv Energy Mater 2014;4:1400567. https://doi.org/10.1002/AENM.201400567.

[195] Wang J, Zhou Y, Shao Z. Porous TiO2(B)/anatase microspheres with hierarchical nano and microstructures for high-performance lithium-ion batteries. Electrochim Acta 2013;97:386–92. https://doi.org/10.1016/J.ELECTACTA.2013.03.015.

[196] Pramudita JC, Pontiroli D, Magnani G, Gaboardi M, Riccò M, Milanese C, et al. Graphene and Selected Derivatives as Negative Electrodes in Sodium- and

Lithium-Ion Batteries. ChemElectroChem 2015;2:600–10. https://doi.org/10.1002/celc.201402352.

[197] Liu H, Grey CP. Influence of particle size, cycling rate and temperature on the lithiation process of anatase TiO2. J Mater Chem A 2016;4:6433–46. https://doi.org/10.1039/C6TA00673F.

[198] Jung SC, Han YK. Monoclinic sulfur cathode utilizing carbon for high-performance lithium–sulfur batteries. J Power Sources 2016;325:495–500. https://doi.org/10.1016/J.JPOWSOUR.2016.06.057.

[199] Moon S, Hwa Jung Y, Ki Jung W, Soo Jung D, Wook Choi J, Kyung Kim D, et al. Encapsulated Monoclinic Sulfur for Stable Cycling of Li–S Rechargeable Batteries. Adv Mater 2013;25:6547–53. https://doi.org/10.1002/ADMA.201303166.

[200] Peled E, Sternberg Y, Gorenshtein A, Lavi Y. Lithium-Sulfur Battery: Evaluation of Dioxolane-Based Electrolytes. J Electrochem Soc 1989;136:1621–5. https://doi.org/10.1149/1.2096981/XML.

[201] Manthiram A, Fu Y, Su YS. Challenges and Prospects of Lithium–Sulfur Batteries. Acc Chem Res 2012;46:1125–34. https://doi.org/10.1021/AR300179V.

[202] El-Kady MF, Strong V, Dubin S, Kaner RB. Laser scribing of high-performance and flexible graphene-based electrochemical capacitors. Science (80-) 2012;335:1326–30. https://doi.org/10.1126/SCIENCE.1216744/SUPPL_FILE/EL-KADY-SOM.PDF.

[203] Park CM, Choi W, Hwa Y, Kim JH, Jeong G, Sohn HJ. Characterizations and electrochemical behaviors of disproportionated SiO and its composite for rechargeable Li-ion batteries. J Mater Chem 2010;20:4854–60. https://doi.org/10.1039/B923926J.

[204] Keller C, Desrues A, Karuppiah S, Martin E, Alper J, Boismain F, et al. Effect of size and shape on electrochemical performance of nano-silicon-based lithium battery 2021;11:307. https://doi.org/10.3390/nano11020307ï.

[205] Hu L, Xia W, Tang R, Hu R, Ouyang L, Sun T, et al. Excellent Cyclic and Rate Performances of SiO/C/Graphite Composites as Li-Ion Battery Anode. Front Chem 2020;8:388. https://doi.org/10.3389/FCHEM.2020.00388/BIBTEX.

[206] Dimov N, Kugino S, Yoshio M. Carbon-coated silicon as anode material for lithium ion batteries: advantages and limitations. Electrochim Acta 2003;48:1579–87. https://doi.org/10.1016/S0013-4686(03)00030-6.

[207] Scaravonati S, Sidoli M, Magnani G, Morenghi A, Canova M, Kim J-H, et al. Combined capacitive and electrochemical charge storage mechanism in high performance graphene-based lithium-ion batteries. Mater Today Energy 2021:100928. https://doi.org/10.1016/J.MTENER.2021.100928.